

UC Berkeley

UC Berkeley Electronic Theses and Dissertations

Title

Integrated Polymer Microfluidic-Electronic Sensors and Actuators

Permalink

<https://escholarship.org/uc/item/0hm5h794>

Author

Chooljian, Marc Steven

Publication Date

2020

Peer reviewed|Thesis/dissertation

Integrated Polymer Microfluidic-Electronic Sensors and Actuators

By

Marc S. Chooljian

A dissertation submitted in partial satisfaction of the

requirements for the degree of

Joint Doctor of Philosophy
with University of California, San Francisco

in

Bioengineering

in the

Graduate Division

of the

University of California, Berkeley

Committee in charge:

Professor Dorian Liepmann, chair

Professor Jeffrey Bokor

Professor Amy Herr

Professor Tejal Desai

Summer 2020

Abstract

Integrated Polymer Microfluidic-Electronic Sensors and Actuators

by

Marc S. Chooljian

Joint Doctor of Philosophy in Bioengineering
with the University of California, San Francisco

University of California, Berkeley

Professor Dorian Liepmann, chair

Though microfluidic and BioMEMS devices have been active areas of research since the late 1990s, commercial success of diagnostic tools making use of these technologies has been limited, especially with regard to complex “micro-total analysis systems” with integrated fluid control and sample preparation. The incompatibility of current prototyping technology (PDMS soft lithography) used during the discovery phase with large-scale industrial production and the difficulty of integrating electronic sensing and fluid control with PDMS devices contribute to this problem by requiring substantial redesign of microfluidic devices from prototype to manufacturable product. Therefore, there is a need for a lab-scale prototyping method that is compatible with manufacturing-friendly materials and which allows for simple integration of electronic components.

I will describe such a method based on hot embossing of thermoplastics and propose modifications to this method which allow for simultaneous patterning of microfluidic channels and integration of electrodes with a variety of geometries. This method involves minimal specialized equipment and is similar in complexity to the fabrication of PDMS devices. Furthermore, I will describe applications of this manufacturing technology to impedance cytometry and electrolysis-driven pumping.

Efforts to increase the complexity and decrease the footprint of microfluidic devices also require novel strategies for on-chip sensing and actuation. To that end, I will also describe two strategies for such compact active devices. The first is a pump powered by chemical propellant and fabricated using high-resolution 3D printing, which has been applied to oral vaccine delivery. The second is an electrically-actuated magnetic particle sorter which makes use of the inverse magnetostrictive effect in a multiferroic heterostructure to achieve local control of particle motion without an external magnetic field.

Taken together, the work described in this dissertation is intended to advance the potential of integrated microfluidic systems to function without the requirement of an extensive external infrastructure including off-chip pumps and microscopes, and to ease the

transition of microfluidic devices out of the lab by incorporating some design-for-manufacturing ideas into the early stages of the development of such devices.

Table of Contents

<u>CHAPTER 1: INTEGRATION OF MICROFLUIDIC-ELECTRONIC SYSTEMS.....</u>	<u>1</u>
CHAPTER 1A: MATERIAL CONSIDERATIONS FOR SCALE-UP	1
CHAPTER 1B: INTEGRATION AND THE “CHIP-IN-A-LAB” PROBLEM	2
CHAPTER 1C: EXISTING STRATEGIES FOR ELECTRONIC-MICROFLUIDIC INTEGRATION	2
CHAPTER 1D: DIRECT PATTERNING OF CONDUCTIVE SURFACE FEATURES IN POLYMERS.....	3
CHAPTER 1E: LIQUID & CHANNEL-CAST ELECTRODES	4
CHAPTER 1F: EMBEDDED CONDUCTIVE ELEMENTS IN POLYMERS	5
CHAPTER 1G: ADDRESSING UNMET NEEDS IN PROTOTYPING OF ACTIVE MICROFLUIDIC SENSORS & ACTUATORS.....	5
<u>CHAPTER 2: MICRO-HOT EMBOSsing OF MULTILAYER MICROFLUIDIC-ELECTRONIC DEVICES IN THERMOPLASTICS.....</u>	<u>7</u>
CHAPTER 2A: INTRODUCTION	7
CHAPTER 2B: THEORY OF THE HOT EMBOSsing PROCESS.....	7
CHAPTER 2C: CHANNEL MOLD PROCESS OPTIMIZATION	9
CHAPTER 2D: HOT EMBOSsing PROCESS	13
CHAPTER 2E: EMBEDDED ELECTRODE PROCESS OPTIMIZATION.....	15
CHAPTER 2F: ELECTRODE DEFORMATION	16
CHAPTER 2G: BONDING AND ASSEMBLY	20
CHAPTER 2H: POTENTIAL OF PARALLEL-PLATE DEVICES FOR IMPEDANCE CYTOMETRY.....	21
CHAPTER 2I: FIELD HOMOGENEITY AND ELECTRODE GEOMETRY	23
CHAPTER 2J: PARALLEL PLATE ELECTRODE FABRICATION	25
CHAPTER 2K: DISCUSSION	26
<u>CHAPTER 3: ACTIVE ELECTROLYSIS PUMP USING EMBEDDED ELECTRODES.....</u>	<u>28</u>
CHAPTER 3A: INTRODUCTION	28
CHAPTER 3B: THEORY & DESIGN OF ELECTROLYSIS PUMP	28
CHAPTER 3C: FABRICATION OF ELECTROLYSIS PUMP.....	30
CHAPTER 3D: CHARACTERIZATION OF FLOW RATES.....	30
CHAPTER 3E: DISCUSSION	34
<u>CHAPTER 4: CHEMICALLY-ACTUATED MICROJET INJECTOR.....</u>	<u>35</u>
CHAPTER 4A: INTRODUCTION	35
CHAPTER 4B: FUNCTIONAL PRINCIPLE OF PUMP	35
CHAPTER 4C: MICROJET SIMULATIONS	37
CHAPTER 4D: IN VITRO INVESTIGATION USING PORCINE BUCCAL MUCOSA	39
CHAPTER 4E: DISCUSSION	40

<u>CHAPTER 5: COMPACT, ELECTRICALLY CONTROLLED MICROMAGNETIC ACTUATORS FOR MICROFLUIDICS APPLICATIONS</u>	<u>42</u>
CHAPTER 5A: INTRODUCTION	42
CHAPTER 5B: THEORY OF MULTIFERROIC ACTUATOR.....	42
CHAPTER 5C: DESIGN OF MULTIFERROIC-MICROFLUIDIC GATE.....	43
CHAPTER 5D: CHARACTERIZATION OF PARTICLE TRAP AND RELEASE MECHANISM.....	47
CHAPTER 5D: PATTERNED MICROELECTRODES FOR LOCAL STRAIN CONTROL.....	49
CHAPTER 5E: FABRICATION	51
CHAPTER 5F: STRAIN MEASUREMENTS.....	52
CHAPTER 5G: MICROFLUIDIC DEVICE ASSEMBLY.....	68
CHAPTER 5H: DISCUSSION.....	70
<u>CONCLUSION.....</u>	<u>71</u>
<u>WORKS CITED.....</u>	<u>72</u>
<u>APPENDIX A: MATLAB SCRIPT FOR STRAIN IMAGE GENERATION</u>	<u>78</u>
<u>APPENDIX B: NICKEL EMBOSSING MOLD SOP</u>	<u>80</u>

Acknowledgements

I would like to thank my advisor and dissertation chair, Prof. Dorian Liepmann, who has been a mentor to me since early in my undergraduate career. He is a caring and insightful advisor who truly believes that the purpose of a PhD is to educate, and to that end has allowed me to pursue whatever strange impulses I had regarding my project as well as my numerous forays into academic service. It is rare to find an advisor who values the well-being of his students to the degree that Dorian does. I would be remiss if I did not acknowledge his sense of humor, without which my spirits would have been considerably lower at times throughout the last several years. I would also like to thank Bodie for his top-notch technical advice.

I would also like to thank my co-advisor, Prof. Jeffrey Bokor, for his support, mentorship, and considerable patience as we attempted a deeply ambitious cross-field collaboration. Though my time in Jeff's lab was relatively short, I am very grateful for the opportunity to immerse myself in a fascinating field about which I knew very little prior to beginning this project.

To the remaining members of my dissertation committee, Prof. Tejal Desai and Prof. Amy Herr, I am grateful for your time, advice, and scientific inspiration. I would like to extend additional thanks to Prof. Herr for going above and beyond as a mentor on a variety of occasions: welcoming me into your group meetings, providing advice on the trials of GRS fundraising, and supporting the creation of the Science Policy Group.

I acknowledge the financial support of the Siebel Scholars Foundation and Kang Family Graduate Fellowship for Biotechnology, which helped support my meandering path through graduate school. Special thanks to Tom Siebel for organizing the Siebel Scholars conferences, which among other things gave me the opportunity to ask Karl Rove a question he didn't like.

I would like to thank the director of the BNC, Paul Lum, for being incredibly generous with his time, expertise, and ability to generate useful equipment seemingly out of thin air. He and his facility have been an invaluable resource for virtually every part of the work described here.

I am incredibly grateful to my mentors in the Liepmann group: Dr. Jacobo Paredes, Dr. Kathryn Fink, and Dr. Kiana Aran. I only wish our time in lab together could have overlapped more. Jacobo, thank you for teaching me your creativity in lab and your ability to maintain high spirits even in the BNC cleanroom. Katie, thank you for being a good listener and a source of consistently good advice about grad school. Kiana, thank you for helping kick my productivity into gear when I was lacking in motivation.

I would like to thank graduate and undergraduate students who I had the privilege of mentoring: Nick Engel, Alice Vergani, Samir Hossainy, Jackelin Amorin-Cotrina, and Shahad Jawad, not only for their technical help but for the experience of being able to watch them grow as scientists. In particular, Alice Vergani provided invaluable help with microfabrication

process development and Jackelin Amorin-Cotrino and Shahad Jawad made considerable contributions to the work described in Chapter 3 of this dissertation.

To the members of the Bokor group and to our collaborators in TANMS, I am grateful for our brief time together. In particular, I would like to thank Roberto Lo Conte, Maite Goiriena-Goikoetxea, Hanuman Singh, Maggie Xiao, Reem Khojah, Mohanchandra Kotekar Panduranga, Akshay Pattabi, and Hyejin Jang for scientific collaboration, good times, or both.

Thanks to Dr. Nobumichi Tamura, beamline scientist at LBNL, for invaluable assistance with microdiffraction experiments and data processing.

My sincerest thanks to the friends who have helped me get through this with my sanity intact. Special mention to Mark Hettick for tolerating my eccentricities from middle school through graduate school at the same institutions, to Kevin Yamauchi and Colin Zamecnik for sitting through many a Fieldwork-fueled monologue, to Ryan Orendorff for helping force me out of my shell, to Chris Eiben for encouraging me to think of things from interesting angles, to Emerson Knapp for sharing the stranger parts of my sense of humor, and to Tom Zajdel, Todd Duncombe, and Julea Vlassakis for being at various times sources of scientific insight, mentors, and friends.

To my undergraduate research mentors, Dr. Wendy Cousin and Dr. Christian Elabd, who taught me my first lessons in how to be a scientist – thank you for taking a risk on me and for having patience with an undergrad who didn't always have his priorities straight.

It is absolutely impossible to capture in words how much I owe to my parents, Steven and Karen Chooljian, who have taught me the value of education and who have supported me in every way they conceivably could have, and my sister Catherine Chooljian, who has always been there for me.

Finally, my partner, Mane Chakarian: thank you for being at my side while I have gone through the difficult patches of graduate school, for supporting me through the frustrating parts and the late nights, and for helping me celebrate the good parts. I could not have done this without you.

Chapter 1: Integration of Microfluidic-Electronic Systems

Chapter 1a: Material Considerations for Scale-Up

Microfluidic technologies have long served as a source of considerable excitement in the academic community regarding their potential as platforms for biology, in particular for high-resolution biological measurements (e.g. single cell measurements) and for point-of-care diagnostic platforms. However, particularly in the latter area, the considerable body of academic research in this area has had limited translational success. Among the many reasons for this are two related problems in the manufacturing space: a mismatch between the materials used for prototyping and scale-up, and a reliance on bulky, off-chip sensing and actuation methods instead of on-chip integration.

The academic microfluidics community has largely relied on poly(dimethylsiloxane) (PDMS) soft lithography since its popularization by the Whitesides group (Ng *et al.* 2002). Microfluidic channels with a high aspect ratio and small feature size can be reliably molded in PDMS from a photoresist master, and the process requires minimal equipment and little specialized microfabrication expertise. However, this process limits material selection to PDMS and related elastomers, and some properties of these elastomers are undesirable for certain applications; for example, some low molecular weight amphiphilic compounds can partition into PDMS (Toepke and Beebe 2006), and most surface treatments for cell culture are designed to be compatible with polystyrene, which is a thermoplastic and is not compatible with soft lithography (Berthier, Young, and Beebe 2012). Additionally, PDMS is a poor material for manufacturing at scale due to its comparatively high cost and slow cure and degas steps. Thermoplastics, which are versatile, inexpensive and can be manufactured with high precision at scale using hot embossing or injection molding processes (Becker and Locascio 2002), are a desirable alternative; however, these processes have suffered from a high startup cost due to the comparatively difficult mold fabrication and are therefore much less popular for prototyping in academic labs.

Recently, interest in plastics as prototyping materials for microfluidic systems has been growing and several groups have developed methods for inexpensive lab-scale microfabrication in thermoplastics. In particular, several methods for low-cost prototyping of hot embossing molds have been developed, including vinyl-masked electroplating of nickel (Novak, Ranu, and Mathies 2013), micro-CNC (Wei *et al.* 2012), and even the use of PDMS as an embossing mold (Goral *et al.* 2010). Apart from the mold making, hot embossing requires minimal equipment and per-run material costs are very low, and these methods compete very favorably with soft lithography in terms of cost and expertise requirements. Furthermore, they are compatible with a much wider range of materials than soft lithography, including polycarbonate, acrylic, and polystyrene. The majority of materials that can be hot embossed are compatible with injection molding, meaning that devices prototyped using these methods can be minimally modified for mass production using injection molding tools.

Chapter 1b: Integration and the “Chip-in-a-Lab” Problem

Of particular concern for point-of-care diagnostic devices is miniaturization and ease of use. In the analogous area of microelectronics, the development of the integrated circuit has allowed for the miniaturization of a variety of electronic components on a single chip, including power electronics, logic, memory, gas- and photosensors, MEMS oscillators, and antennas. This capability to integrate nearly every component of a fully functional device has been critical to the development of distributed sensing and the “internet of things.” Microfluidic chips, by contrast, are typically largely passive in nature, consisting entirely of microchannel networks and pneumatically actuated membrane valves (Unger *et al.* 2000), which require off-chip pneumatic control via a solenoid manifold. Sensing typically relies on off-chip optics, with the size, weight, cost, and power requirements of the microfluidic system itself being dwarfed by those of the microscope required to read out a fluorescent display. In an academic laboratory, this equipment is all readily available, but pneumatic and optical systems are notoriously difficult to miniaturize.

Electronic sensors and actuators, by contrast, have excellent scaling properties as they are miniaturized. Numerous applications for integrated microfluidic-electronic systems exist, including impedance cytometry, dielectrophoretic cell trapping, electroosmotic pumping, etc. However, these devices are often limited in PDMS microfluidic devices by the difficulty of including more than one electronic layer. Methods for fabricating more complex structures in glass and silicon microfluidic chips exist, but require expensive, multi-step cleanroom processing and a comparatively expensive substrate.

Chapter 1c: Existing Strategies for Electronic-Microfluidic Integration

The dominant consideration for electronic-microfluidic integration in most academic settings is ease of fabrication. As a result, most microfluidic devices used in an academic setting use one or more layers of thin film electrodes deposited on a glass microscope slide or a diced glass wafer, which is then bonded to a PDMS microfluidic layer using oxygen plasma. This method necessitates the separation of the electronic and microfluidic components into distinct layers. Additionally, it requires that a substantial area of the electronic layer be dedicated to fluidic interfacing (inlets and outlets). This consideration is incompatible with typical CMOS fabrication strategies which attempt to maximize the number of useful features per wafer, in particular when the substrate material is precious.

Strategies for electronic-microfluidic integration can be separated into two broad categories based on approach: packaging of a full chip fabricated using a separate microfabrication process, or direct integration of microfluidic features with other microstructures such as electrodes or magnets. The first approach requires the least modification of existing fabrication strategies for either microelectronics or microfluidics; the

aforementioned glass slide-PDMS system is an example of such an approach. More sophisticated efforts in this vein may seek to eliminate wasted microelectronic real estate by embedding a small chip in a gasket material. For example, Murali *et al.* successfully encapsulated a CMOS magnetic cytometer in a microfluidic channel using a plastic gasket and a PDMS cap which incorporated cavities for wire bonding (Murali, Niknejad, and Boser 2017), and El Fissi *et al.* encapsulated a quartz crystal microbalance array in a replica-molded polymer cartridge containing microfluidic channels (El Fissi *et al.* 2019). Flip-chip bonding with a polymer intermediate layer has also been used to mate CMOS chips with single-layer PDMS microfluidic chips (Welch and Christen 2013).

Chapter 1d: Direct Patterning of Conductive Surface Features in Polymers

Due to the preponderance of PDMS and other soft elastomers in microfluidic fabrication and the fact that these materials are unsuitable as substrates for lithography or micromachining, the second strategy, direct integration of microfluidic and microelectronic features, has been less common. However, prior to the widespread adoption of soft lithography by the microfluidics community, silicon microfabrication techniques were commonly employed in microfluidics fabrication and complex integrated microfluidic-electronic structures such as valves (Messner *et al.* 2007), MEMS cantilevers (Zhang *et al.* 1997), pumps (Böhm, Olthuis, and Bergveld 1999), etc. were fabricated in silicon and glass. These strategies are still employed by the microfluidics community when necessary, such as when making sensitive measurements on small quantities of fluid (Khan *et al.* 2016), but require complex fabrication and expensive materials and are therefore unsuitable for the needs of medical device manufacturers, which require inexpensive disposable chips. To this end, researchers have pursued a variety of methods to integrate electrodes into polymer devices.

Thermoplastics are generally (with some notable exceptions) incompatible with traditional microfabrication techniques, mostly due to their sensitivity to heat and solvents, but methods to deposit metal directly onto plastics using electro- or electroless (X. Tang *et al.* 2009) plating have been developed. This typically requires the deposition of a seed layer and/or the chemical or physical activation of the plastic surface. After the deposition of a seed layer, electroplating can be used to deposit additional layers of metal for passivation or in order to introduce 3D structure (Wu, Benson, and Almasri 2012).

Thin metal layers have also been deposited on polymer layers using printed and annealed metal colloids (Park *et al.* 2007), though this requires a substrate with high thermal resistance for optimal resistivity, limiting compatibility with most hot embossing and injection molding processes, and even then suffers from conductivity losses due to oxidation of the metal nanoparticles during the solvent evaporation and annealing process. Additionally, electrodes can be patterned on polymer surfaces via xurography and lamination of metal foils. Mohammadzadeh *et al.* achieved feature sizes of 66 μm and spacing of 25 μm using this method (Mohammadzadeh, Robichaud, and Selvaganapathy 2019) at low cost and without the use of

photolithography; however, this is likely at the lower limit of feature size possible using a mechanical cutter, and this method is limited to single-layer patterning.

Of particular importance to flexible and transparent electronics (e.g. OLED fabrication) is the patterning of organic conductors and semiconductors on transparent plastics; this can be achieved by a variety of methods including low-temperature stamp transfer, inkjet printing (Lau *et al.* 2013; Ha *et al.* 2013) and thermal ablation via laser (Forrest 2004). These methods have considerable promise for microfluidic devices in the future, in particular for optoelectronic interfacing and in wearable diagnostics, and unlike the methods described above can deposit semiconducting materials as well as conductive materials for applications including electrochemistry and biomolecule-sensitive transistors (Kim, Rusling, and Papadimitrakopoulos 2007).

Of course, certain chemically inert thermoplastic polymers with very high glass transition temperatures, such as polyimides (e.g. Kapton®), are compatible with traditional vapor deposition and liftoff methods (Munief *et al.* 2018). While commonly used in the fields of flexible electronics and optoelectronics, this same quality makes these polymers difficult to work with as substrates for microfluidic devices due to the difficulty inherent in patterning and bonding said materials. The use of these materials as microfluidic substrates is therefore beyond the scope of this work.

Chapter 1e: Liquid & Channel-Cast Electrodes

Another approach to patterning conductive materials in a polymer substrate is to use a network of fluidic channels as a template, either by filling them with a conductive fluid or by casting a conductive polymer or metal within the channels. Due to flow limitations the feature sizes achievable using these methods are limited, but they can be easily integrated with soft lithography or 3D-printing based process flows and are capable of forming electrodes with 3-dimensional geometry.

As most biological buffers are highly conductive, it is convenient and common to use the carrier fluid as a conductive material; in the fields of impedance cytometry (Balakrishnan *et al.* 2015), electrophoresis (Duncombe and Herr 2013), and electroporation/lysis (Wang and Lu 2006), field geometry is frequently modulated by channel dimensions. Side-channels filled with electrolyte can be used as electrode pairs to apply electric fields locally (W. Tang *et al.* 2017). Two-phase flow, in the case where one fluid is conductive and the other insulating, can be used to modulate electric field strength, for instance, to concentrate field lines in order to amplify an impedance signal in a particular region (Rodriguez-Trujillo *et al.* 2008). Separate channels can also be used as ad-hoc electrodes, though screening effects due to the Debye double layer must be accounted for. Other conductive fluids, such as liquid metals (typically gallium or gallium alloys) have lately been gaining popularity as electrode materials in microfluidic systems (Khoshmanesh *et al.* 2017). Of particular interest in these systems is the immiscibility of gallium alloys with water, enabling parallel flow control of electrodes and aqueous solutions in connected channels, as demonstrated by So and Dickey (So and Dickey 2011).

It is also possible to pattern electrodes with low-temperature casting or plating, by selecting electrode materials that undergo a phase change, such as a conductive polymer precursor or a colloidal suspension of metal, or by flowing electroless plating solution into channels (Heuck, Van Der Ploeg, and Stauffer 2011). These approaches obviate the need to fill and control additional flow channels during operation of the device. Furthermore, they allow for electrode shape to be partially controlled by fluid dynamics; for example, Chatzimichail *et al.* demonstrate the ability to fill dead-end channels using vacuum-driven flow with a gas-permeable PDMS membrane on a plastic substrate and to create small electrode gaps with controlled two-phase flow (Chatzimichail *et al.* 2018).

Chapter 1f: Embedded Conductive Elements in Polymers

As metal cannot be directly patterned on PDMS, approaches to embedded PDMS electrodes typically require encapsulation of wires or other self-contained conductive elements, imposing restrictions in feature size. For certain applications that require few electrodes and/or large feature sizes, such as electrochemical sensing, this method can yield good results. (Molina *et al.* 2019)

Encapsulation of electrodes in plastics is possible if the electrodes have a high aspect ratio and the plastic is able to undergo a phase change from a fluid state to a solid one. One method to achieve this is to use an uncrosslinked plastic precursor, such as the photocurable resin (Acrifix 192) used by Schrott *et al.* to interface electroplated gold or copper electrodes with a PMMA chip (Schrott *et al.* 2009). It is also possible to transfer metal features into plastics using hot embossing. Jung *et al.*, who refer to their process as “micropatterned metal embedding” (MME), embedded an aluminum-PMMA double layer structure in a PMMA substrate by embossing, creating a buried conductive layer (Jung *et al.* 2008). More recently, Paredes *et al.* developed a process for direct transfer of electroplated nickel patterns from a stainless steel wafer into PMMA and polycarbonate by hot embossing (Paredes *et al.* 2015). This work forms the basis for the hot embossing-based method used in this thesis, which will be described in detail in the following chapter.

Chapter 1g: Addressing Unmet Needs in Prototyping of Active Microfluidic Sensors & Actuators

The many methods for electronic-microfluidic interfacing described above allow for a wide variety of materials and geometries when taken together, but individually all have limitations in terms of feature size, geometry, materials selection, scalability, or expense. New methods for inexpensive prototyping of active microfluidic elements are still needed, as are designs for low-cost on-chip active systems.

In the following chapters, I will describe a process for the fabrication of three-dimensional metal electrode patterns in contact with fluidic channels using electrodeposition and hot

embossing and two applications of this method: a proposed implementation of a parallel-plate impedance cytometer and a prototype of an electrolysis-driven pump. Furthermore, I will describe active microfluidic components that perform two functions which are typically relegated to off-chip hardware: a chemically driven pump and a magnetic particle sorter.

Chapter 2: Micro-Hot Embossing of Multilayer Microfluidic-Electronic Devices in Thermoplastics

Chapter 2a: Introduction

A variety of manufacturing techniques exist for forming plastic pieces with high feature fidelity at low cost. Particularly, injection molding, thermoforming, and roll-to-roll hot embossing are commonly used for large-scale production of plastics, including microfluidic chips. All three methods require precise mold fabrication and specialized equipment, and in the case of injection molding, require modeling of molten plastic flow in order to ensure adequate mold filling and air bubble exclusion. Plate-to-plate hot embossing has recently arisen as a laboratory-friendly alternative, requiring only a heated press (easily converted from a standard pneumatic shop press) and a mold, and with far simpler dynamics and more easily predictable plastic flow. Simple computational models based on convolution exist to predict the mechanical behavior of planar embossing molds (Taylor, Lam, and Boning 2009) and a variety of methods exist for low-cost prototyping of hot embossing molds, some of which are described in the previous chapter.

A handful of research groups have recently proposed that hot embossing can also be used as a packaging method for conductive elements and/or microelectronics. In particular, the work described here expands on the method described by Paredes *et al.* (Paredes *et al.* 2015) for transferring self-anchoring nickel microelectrodes into plastic using hot embossing. I have made modifications to the mold fabrication and hot embossing processes to improve the consistency of the method for both channel mold and electrode fabrication, and have added an additional deformation step which allows for three-dimensional electrode patterning. Furthermore, I propose a design for a parallel-plate impedance cytometer fabricated using this method.

Chapter 2b: Theory of the Hot Embossing Process

Thermoplastics are polymers that exhibit a characteristic change in their mechanical properties - called the glass transition - as they are heated and cooled. Unlike thermosets or elastomers (such as silicone rubbers), in which the polymer chains are covalently crosslinked, polymer chains in thermoplastic materials are bonded only by van der Waals forces and therefore can reorient and slide at elevated temperatures or stresses, giving rise to this behavior. Below the glass transition temperature T_g , the material is in the “glassy” state and behaves as a rigid linearly elastic material; as with other linearly elastic materials, the mechanism of deformation in this case is bond lengthening. Above T_g , there is sufficient energy to transiently break the van der Waals forces between polymer chains and local motion of chains relative to each other is possible, giving rise to a “rubbery” state that exhibits viscoelastic deformation (Peng *et al.* 2014).

This phenomenon is not a first order phase transition, as the process occurs gradually and does not involve a latent heat. T_g is therefore not an exact temperature but a characteristic

temperature that approximates the center of the distribution of temperatures over which the glass transition occurs. Nevertheless, sufficiently far from T_g the approximation can be made that the plastic behaves as if it is purely in the “glassy” elastic or the “rubbery” viscoelastic state. As amorphous materials, most thermoplastics do not, strictly speaking, have a first-order melting point associated with a latent heat, but a similar transition occurs at elevated temperatures where the van der Waals bonds completely dissociate and chains move freely, causing the polymer to behave like a purely viscous liquid. Hot embossing processes are generally carried out in the temperature regime above T_g but below this viscous flow temperature T_f .

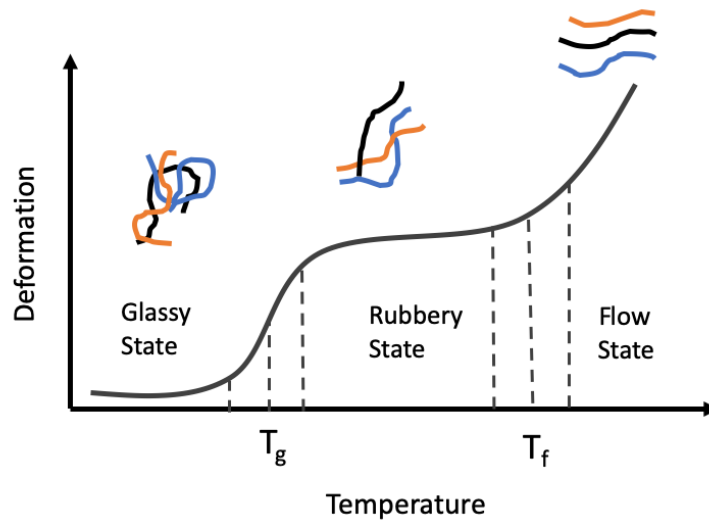


Figure 2-1: Illustration of temperature vs deformation in a thermoplastic material as it moves through the glass transition. Red, blue and black lines above the graph illustrate the behavior of the polymer chains in each state.

As a viscoelastic material, the thermoplastic in its rubbery state exhibits a temperature-dependent deformation in two steps. The short-time deformation behavior is purely elastic and results in a characteristic curved surface with a gap between the surface of the plastic and the mold, referred to a “swallowtail” shape by Liu *et al.* (C. Liu *et al.* 2010). Viscous relaxation and reflow then fill this gap, reproducing the desired feature. The process time for the embossing step is thus bounded below by the characteristic reflow time, which according to Heyderman and coauthors is given by:

$$t_f = \frac{\eta S^2}{2p} \left(\frac{1}{h_f^2} - \frac{1}{h_0^2} \right)$$

$$h_f = h_0 - WD/S$$

for a 2-dimensional periodic structure of cavities with cavity width W , cavity depth D , and cavity to cavity pitch S , where η is the viscosity (dependent on temperature), p is the embossing pressure, and h_0 and h_f are the initial and final thicknesses of the bulk plastic layer (Heyderman *et al.* 2000). Substituting in h_f gives a second-order polynomial expression in terms of the dimensions of the cavity. This equation assumes identical, rectangular trenches and neglects effects from trapped air and surface slip. It follows that the characteristic fill time can be approximated as linear with the viscosity and inversely proportional to the embossing pressure; increasing the pressure and/or the temperature will therefore reduce the embossing time, as will reducing the cross-sectional area and depth of the features to be filled. In reality, high aspect ratio structures will result in trapped air during embossing, which will result in a more complex relationship between dimensions and fill time.

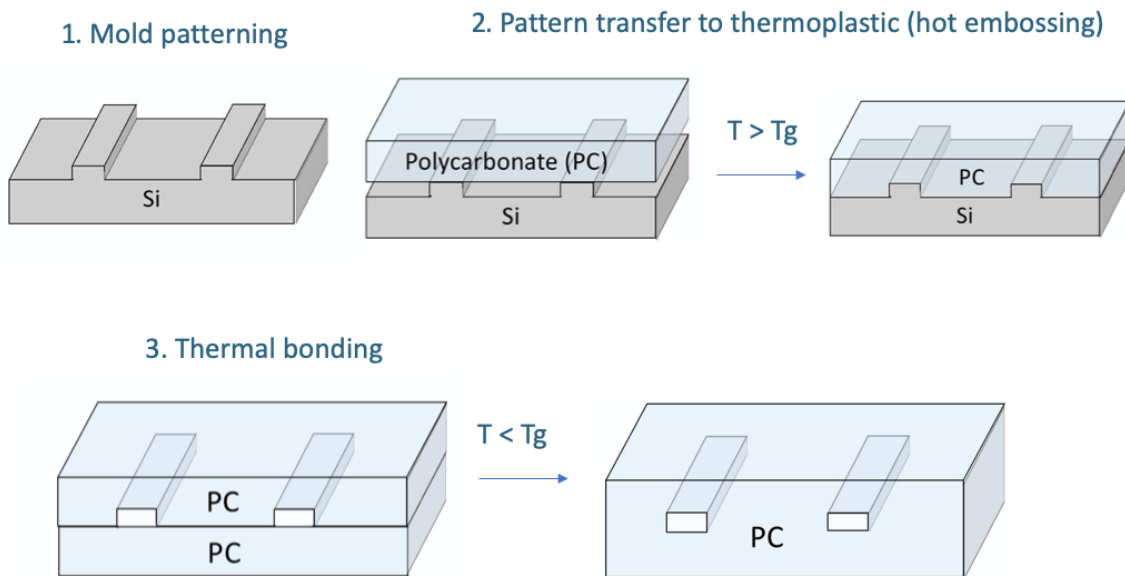


Figure 2-2: Schematic of a process for embossing and sealing channels in polycarbonate using a silicon mold.

Chapter 2c: Channel Mold Process Optimization

Like most replication processes, mold preparation constitutes the bulk of the cost of micro hot embossing. Due to the high thermal expansion coefficients of thermoplastics relative to most materials, thermal mismatch forces are very high during cooldown and demolding, and demolding temperature must be carefully controlled to prevent damage to the mold or the plastic. Even at optimal demolding temperature, the demolding force is still quite high, and thus

the mold material must be mechanically strong in order to survive the process and not leave residue in the molded channels. Lithographically defined SU-8 molds, as used in PDMS soft lithography, are not compatible with this process due to the relatively poor adhesion between the photoresist and the substrate causing the features to peel off in the plastic. Typically, due to these requirements, micromolds for hot embossing are metal and are patterned either through micromilling or electrodeposition. In some cases, when demolding stress and pressure distribution on the platens can be tightly controlled, less mechanically robust materials such as silicon, 3D printed plastic, or even PDMS are used.

The work described here used one of two methods for channel mold fabrication. For feature sizes greater than 50 μm , the mold material was nickel electrodeposited on a stainless steel substrate. This was based on the process described by Novak *et al.* (Novak, Ranu, and Mathies 2013) but used an inexpensive dry film photoresist (Riston GM130) and mylar photomasks instead of cut vinyl as the masking material. Though this process did involve one photolithography step, the choices of substrate, photoresist, and electroplated material make this a very low-cost microfabrication method which compares very favorably in terms of cost, equipment, and training requirements to PDMS soft lithography.

Mirror polished 100mm stainless steel wafers were cleaned with acetone and isopropanol and dried before applying Riston GM130 by laminating at 115 degrees C. The photoresist-coated wafer was cooled to room temperature while covered on an aluminum cooling rack and then exposed at approximately 70 mJ/cm^2 in an OAI UV mask aligner. Immediately after the exposure, the photoresist was developed in 1% w/v potassium carbonate solution under moderate agitation. The development time for this process was by far the most variable component in the process and was extremely sensitive to photoresist loading; it was very easy to over- or underdevelop the photoresist, leading in both cases to poor plating adhesion due to residual photoresist on the bottom of the channel. In the case of underdevelopment, undeveloped photoresist remained in the channel; in the case of overdevelopment, the sidewalls of the pattern would collapse, fouling the surface. The development time ranged from 8-20 minutes; in the latter case, which applied to patterns with a large proportion of open area (and thus a large amount of photoresist dissolved in the developer) but small features, a double bath exposure would be used (10 minutes in each bath). The wafers were then sprayed briefly with developer and then rinsed in a bath of deionized water for 5 minutes.

In order to promote adhesion between the electroplated nickel and stainless steel substrate, the wafer was immersed in a Wood's nickel strike solution (240 g/L nickel chloride and 20% w/v HCl) and a current of 1A was applied between the wafer (cathode) and a nickel plate (anode) at 50 degrees C for 1 minute under vigorous agitation. The wafer and nickel anode were kept a constant distance from each other using a custom 3D printed frame. The anode and wafer were then transferred to a nickel plating bath made from nickel plating crystals (Caswell Inc., 80% nickel sulfate, 15% nickel chloride, 5% boric acid) and brightener (Caswell nickel/copy chrome brightener, 10% saccharin) and plated at 65 mA. The plating rate depends on the current density (and therefore on the area of the exposed features) according to the following relationship:

$$d = C \frac{iM_w\rho}{nF}$$

Where d is the plating rate in m/s, i is the current density in A/m², ρ is the density of the deposited metal in kg/m³, M_w is the molar mass of the metal, n is the charge number of the metal ion, F is Faraday's constant, and C is the cathode efficiency, or the proportion of charge that is consumed by the reduction reaction at the cathode rather than by the electrolysis of water to hydrogen gas, which is typically 92-97% for nickel plating baths (DiBari 2008). M_w/nF is the electrochemical equivalent of the metal, or the mass per charge; this equation is a simple expression of conservation of charge. For the Ni²⁺ ions present in nickel plating solutions (valence 2, molar mass 58.69 g/mol) this is equal to 3.04×10^{-4} g/C. It is important to note that this equation relates the *local* plating rate to the *local* current density – in other words, features that cause electric field concentration such as small features, channel edges, or protrusions in the plating surface will cause local variations in plating rate. Left unchecked, this can cause a feedback process as areas of increased plating thickness can cause further concentration of field lines and higher current density, leading to a rough surface. To mediate this effect, electroplating solutions include brighteners, organic compounds which nucleate around protrusions in the metal deposit and reduce the deposition rate in these areas. This current concentration effect also caused a characteristic “saddle” shape to channel molds (see Figure 2-3) resulting from the concentration of field lines at the edges, which is reduced in larger features and with slower plating rates.

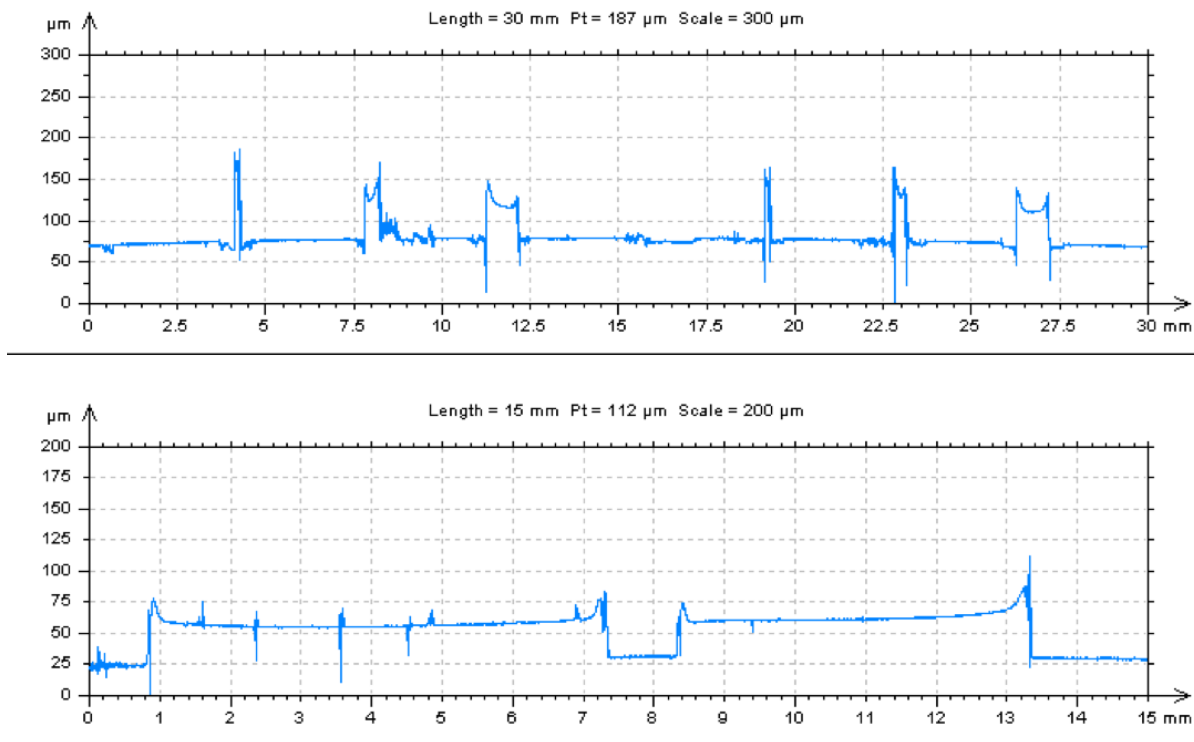


Figure 2-3: Profiles of plated channel molds. Channel molds plated for 2h at 250mA in Caswell nickel plating solution. Saddle shape is more exaggerated in small channels.

Care must be taken not to plate thicker than the photoresist layer (70 μm for Riston GM-130) or the features will separate from the wafer either during the photoresist strip (due to swelling) or during the subsequent embossing step. After plating, the wafer is rinsed in deionized water and then the photoresist is removed from the surface using a solution of 3% w/v KOH under moderate agitation. The primary failure mode of a mold fabricated using this method is separation of the features from the stainless steel substrate during embossing – in order to prevent this, an additional annealing step at 400 degrees C for 10 minutes may be incorporated here to reduce the residual stress in the nickel plate and to promote interdiffusion of nickel and stainless steel and therefore higher adhesion.

For feature sizes from 4-50 μm, the mold material was silicon patterned with deep reactive ion etching. A standard i-line contact photolithography process using 12 μm thick AZ-4620 photoresist to mask a Bosch etch was performed using a Surface Technology Systems Advanced Silicon Etch inductively coupled plasma system. The Bosch etch alternates a dry silicon etch using SF₆ with a sidewall passivation using C₄F₈ in order to achieve a deep etch with nearly straight (~100nm scalloping) sidewalls, thus allowing for high aspect ratio silicon features. This process is much costlier and requires much more specialized equipment than the plating process above, and was therefore used exclusively for the project described in Chapter 4 which required high aspect ratio channels with single micron feature sizes.

Chapter 2d: Hot Embossing Process

After mold fabrication, the pattern is transferred into a plastic (in this work, polycarbonate or poly-(methyl methacrylate)) sheet via hot embossing. The plastic was placed between the mold and a clean, unpatterned backing wafer, which were sandwiched between two layers of unpatterned PDMS to dissipate any concentrations of pressure caused by an uneven surface. This assembly was then placed onto the hot embosser and the embossing cycle is performed. See Figure 2-4 for an image of the hot embosser; ours is a hand cranked pneumatic shop press with custom-built platens that contain resistive heating coils, thermocouples and an air cooling system. The heating of the upper and lower platens is set by a pair of independent PIV controllers and the flow of air is also independently controllable to each platen by manual valves so that the temperature can be kept roughly equal during the cooling step despite the difference in thermal mass between the platens.

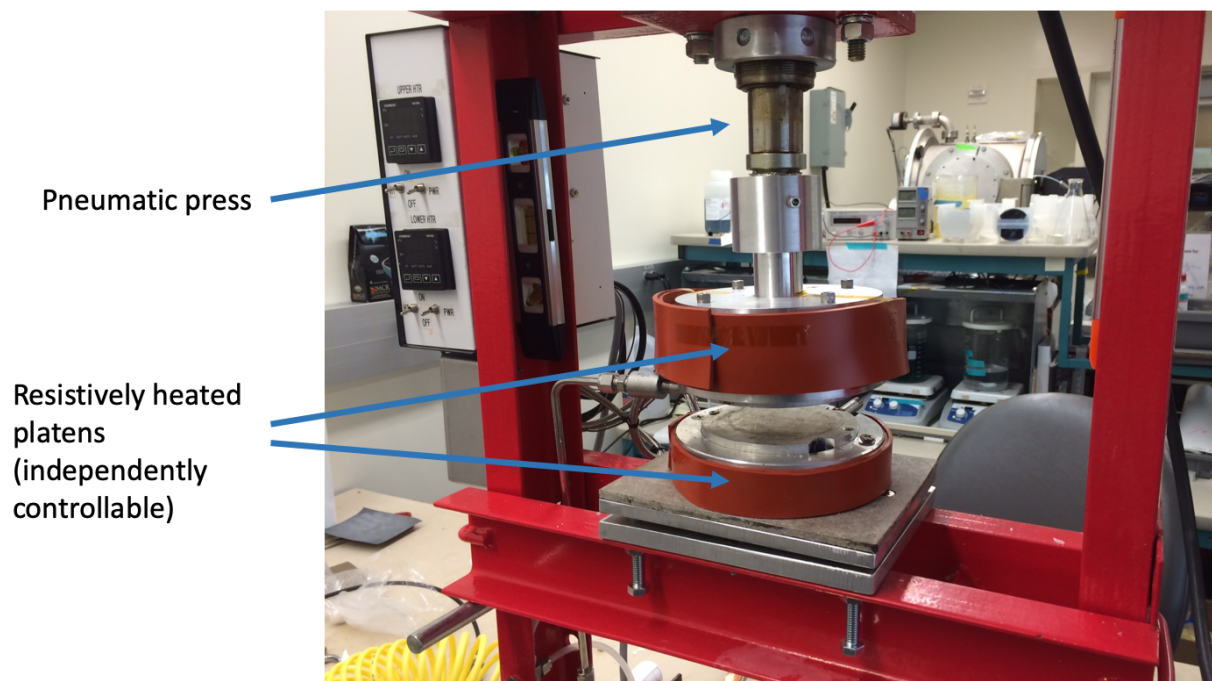


Figure 2-4: Hot embossing setup in the UC Berkeley Biomolecular Nanotechnology Center (BNC). Consists of two platens with independently PID-controlled resistive heaters, one of which is mounted on a pneumatic column. Platens also contain air channels for active cooling.

As described above, the hot embossing process consists of 4 steps: heating, embossing, cooling, and demolding. During the heating step, the platens and mold assembly were brought into contact but no extra pressure was applied, in order to ensure that the mold assembly is heated evenly from both sides but avoid applying any pressure while the plastic is in the elastic deformation regime which could damage the plastic or the mold. Due to thermal expansion, some pressure may be applied to the mold assembly as it approaches the glass transition temperature. This is acceptable and even desirable as it will assist in removing any air bubbles

from the mold-plastic interface, as long as the pressure is not in excess of 100 PSI. When the temperature reaches the target temperature of 10-15 degrees above the glass transition temperature (or 160 degrees C for polycarbonate), we allowed the temperature to equilibrate for 2 minutes before the second step, in which the embossing pressure of 500 PSI was applied for a period of time which is dependent on the size of the desired features and the viscosity of the plastic used. After the embossing time has elapsed, the cooling step begins and the heaters are turned off and the air cooling system is turned on, allowing the platens to cool below the glass transition temperature.

The final step, demolding, introduced the most variability into our hot embossing process, as it is very sensitive to timing and temperature. A particularly challenging aspect of hot embossing is the large mismatch in linear thermal expansion coefficients between thermoplastics (40-120 ppm/K) and mold materials such as metals (10-20 ppm/K), glass (5-10 ppm/K), or silicon (3-5 ppm/K). This causes the plastic features to clamp down on the mold during the cooling phase, causing deformation of the feature in the best case or structural failure of the mold in the worst. For this reason, it is important to demold at the highest temperature possible, when the plastic has cooled down sufficiently far below T_g that it is fully in the rigid state but before the thermal mismatch stress is too large. If the plastic was allowed to cool too much before demolding, structural failure of the mold generally occurred, which took the form of mold features remaining embedded in the plastic in the case of nickel-steel molds or the mold shattering in the case of silicon mold. Either of these failure modes render both the mold and the replica unusable. A less severe failure mode of delayed demolding occurred in a minority of cases where the plastic warped during demolding due to thermal mismatch stress. For our purposes, a temperature of 10-15 degrees below the glass transition temperature was found to be sufficient (135 degrees C for polycarbonate) – any higher and the plastic remained pliable, any lower and the mold was damaged or the plastic would warp.

The addition of an annealing step (400 degrees C for 10 minutes) substantially increased the yield of the channel embossing process by preventing demolding. A thorough investigation into the mechanism by which this occurs is beyond the scope of this dissertation, but I hypothesize that it is due to a combination of the following factors: relaxation of thermal mismatch stress in the nickel deposit leading to less stress discontinuity at the nickel-steel interface, interdiffusion of nickel and stainless steel at the interface, and the formation of a nickel oxide on the surface which reduced surface roughness.

A successful embossing process yields a 3-sided trench in thermoplastic which must then be bonded to another plastic piece in order to seal the channel. This bonding process will be described in Chapter 2g.

Chapter 2e: Embedded Electrode Process Optimization

The sacrificial electrode transfer process used in this work is similar to the process characterized in Paredes *et al.* (Paredes *et al.* 2015). This process takes advantage of the demolding stress to transfer conductive patterns electrodeposited on a stainless steel wafer (in a manner similar to that described above) into a sheet of plastic. A nickel electrode template was patterned by photolithography using 5 μm -thick photoresist (AZ-4620 or S-1818) and electrodeposition on a stainless steel substrate. Following electrodeposition of a sufficiently thick nickel layer (4-8 μm thick, depending on the factors described below), the photoresist was stripped with acetone and the electrode templates were embossed into the target plastic 15 degrees above the glass transition temperature (T_g) of the plastic. After cooling below the T_g , the plastic was separated from the stainless steel substrate and under successful process conditions the adhesion of the nickel to the stainless steel was substantially weaker than the demolding force, causing the electrodes to remain embedded in the plastic. Paredes *et al.* describe a technique involving intentionally overplating the nickel in order to create a mushroom-like anchor structure (see Fig 2-5) – in the course of this work, that has proven either necessary or detrimental to the process depending on the size of the electrodes.

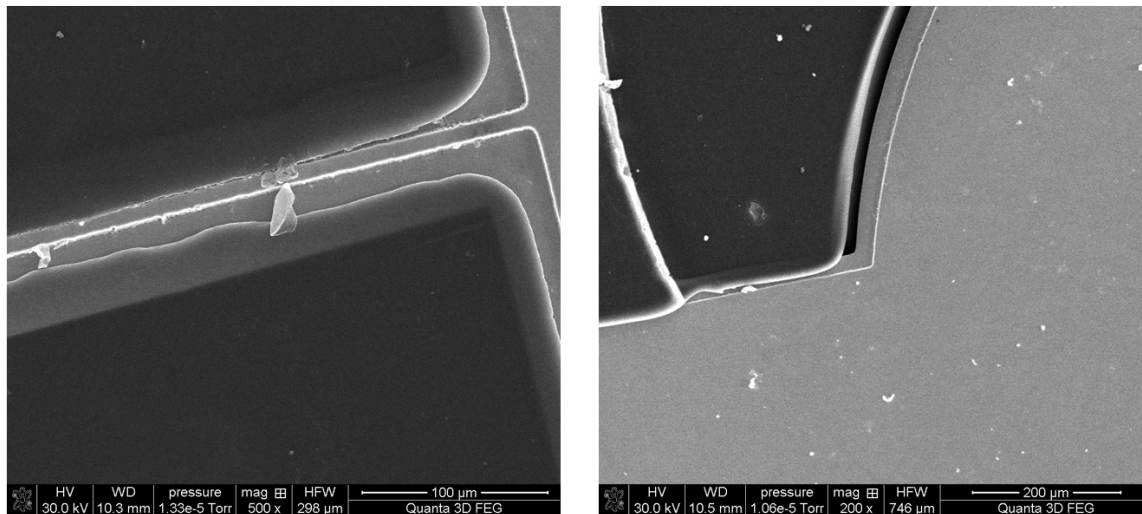


Figure 2-5: SEM images of embedded electrodes. “Mushroom cap” overplate is visible at the edges of the electrodes due to incomplete reflow of plastic. Left: one element of an interdigitated microelectrode array. Right: edge of a 2mm contact pad.

While the process described in this paper is sufficient for large electrodes, some process refinements were necessary to achieve feature sizes smaller than 50 μm . The failure modes involved are the premature liftoff of the electrodes from the substrate due to photoresist stripping and the failure of the electrodes to demold in the plastic. At small feature sizes, the process window between these two extremes is fairly small due to the high aspect ratio of the electrodes and the consequently large ratio of the sidewall surface area to the adhesion area.

The premature demolding process is exacerbated by the “mushroom” overplating technique – this failure mode is in part mediated by swelling of photoresist during stripping, and the existence of the anchor structure above the photoresist causes upward force on the electrode during swelling. Swelling of photoresist during demolding also causes a force on the sidewalls of the electrode, a component of which is upward and therefore contributes to premature demolding. However, for optimal behavior during the embossing and optimal electrical performance the aspect ratio of the electrode should be maximized. The optimal plating thickness is therefore slightly thinner than the photoresist layer without overplating. The process is also highly sensitive to material effects on the adhesion between the nickel and stainless steel, and is thus highly sensitive to both surface cleanliness and plating bath condition. Contamination of the bath with organics or iron or brightener depletion can cause rough, grainy plating, which decreases the adhesion force and also reduces the mechanical and electrical performance of the electrodes during subsequent steps. Careful monitoring and regular replacement of the nickel bath is therefore necessary.

At the other extreme, too much adhesion between the substrate and the nickel deposits can prevent transfer of the electrodes into the plastic. The thermal mismatch stress can be leveraged to provide maximum demolding force. Unlike the channel molding process, in this case the embossed electrodes were allowed to cool to room temperature before demolding. This is to ensure that the electrodes are encapsulated by the plastic and that the demolding force is maximized prior to liftoff. It also has the benefit of minimizing warping, as force is applied to the plastic sheet until it has cooled to room temperature and both sides of the sheet are cooled at the same rate.

Chapter 2f: Electrode Deformation

Unique to this “thick film” transfer strategy is the ability to deform the nickel electrode templates during the channel embossing step. This has the potential to allow for a variety of electrode geometries that are difficult or impossible to fabricate using conventional soft lithography, including “wraparound” electrodes and parallel-plate sensors. After the sacrificial transfer process and mold fabrication process described above, the channel mold was aligned with the embedded electrode templates by eye and the channel embossing process was performed on top of the embedded electrodes (see Figure 2-6). If the electrode is sufficiently thick compared to the depth of the channel, the electrode will deform during the embossing process into a curved shape which allows electrical contact between the bottom of the channel and the surface of the plastic (see Figure 2-7).

The shape of the deformed electrode is determined by the applied load and the drag force of the plastic. The load on the surface of the electrode pushes one end down into the plastic, which above its glass transition temperature acts as a viscoelastic fluid. The drag force from this fluid acts on the other end of the electrode, providing resistance to motion and anchoring the electrode in place. This results in a bent electrode with a radius of curvature dependent on the stiffness of the electrode material and the viscosity of the plastic. The deformation of the electrode creates a plastic-free cavity between the electrode and the stainless steel substrate,

which is then filled by reflow of the plastic. The time constant for this filling process can be estimated using the same equation used during the channel embossing process, but in this case the size of the cavity is the space left by the elastic portion of the embossing plus the space underneath the electrode (which is simply the area of the electrode times the depth of the channel). Should insufficient reflow time be allowed before cooling, the reflow process can be paused and observed (see Figure 2-8).

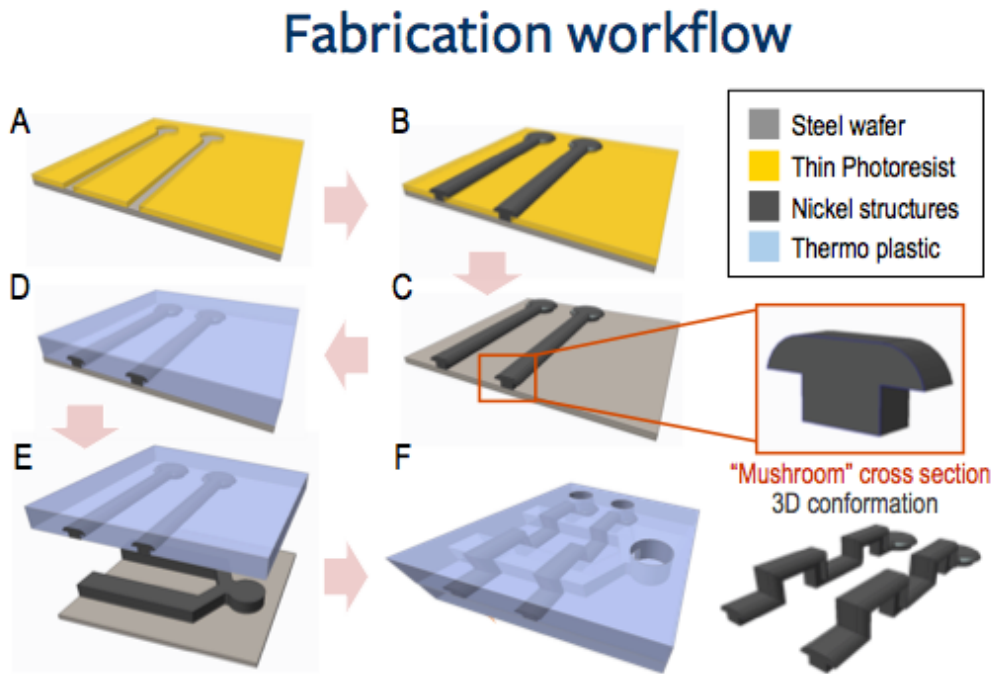


Figure 2-6: Deformed electrode process. A: electrode shapes are patterned in photoresist (3-5 μm thick) using photolithography. B: Nickel electrode templates are deposited by electroplating to a thickness of 1-2 μm more than the thickness of the photoresist. C: Photoresist is stripped. D: Electrodes are transferred into thermoplastic by hot embossing. E: Electrodes are demolded from wafer, remaining embedded in plastic. F: Channel mold (pictured in E) is embossed, resulting in formation of channels and deformation of electrodes.

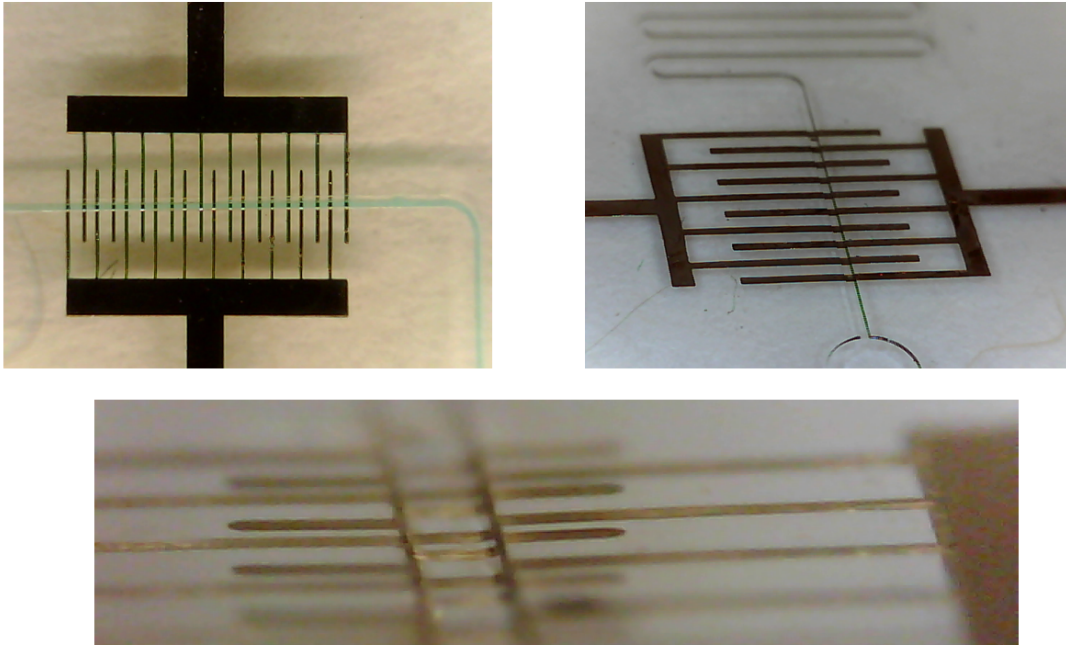


Figure 2-7: Embedded electrode images. Interdigitated electrode arrays produced by the above described process. Top left: “2D” electrode pattern bonded to separate channel layer as described in Paredes *et al.* (2015). Top right: “3D” deformed electrodes. Channel width = 300 μm , electrode width = 100 μm . Bottom: detail of another deformed electrode pattern. Channel width = 300 μm , electrode width = 50 μm .

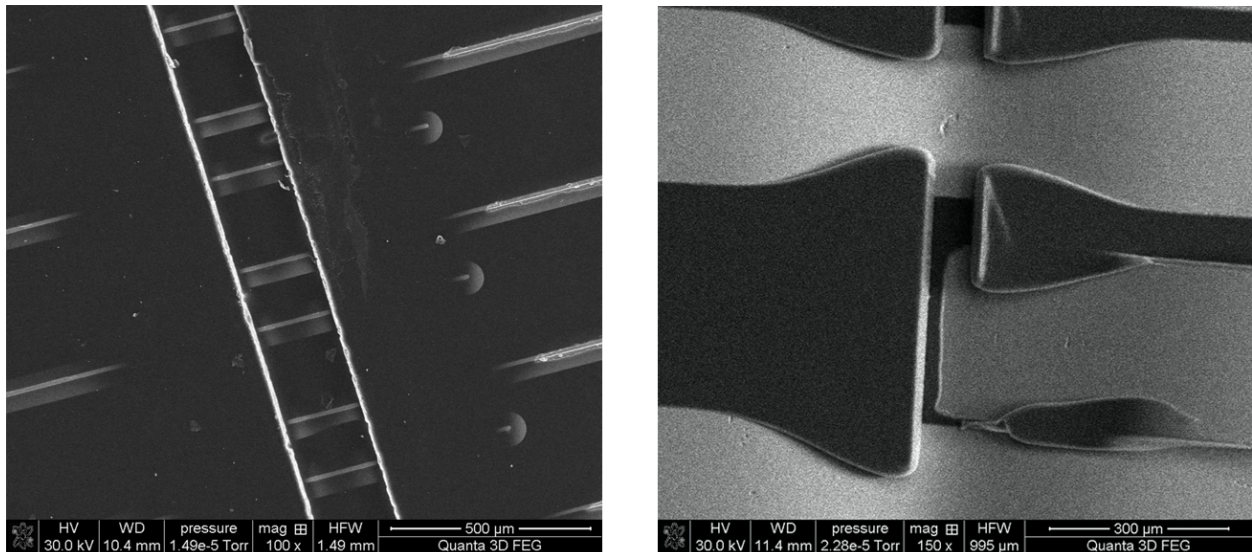


Figure 2-8: SEM images of deformed electrodes after embossing. Left: Sufficient reflow time. Plastic completely covers the electrodes near the edges of the channel. Right: Insufficient reflow time. Electrode curvature can be observed.

Ensuring that the electrical properties of the nickel templates remain viable after deformation is critical, as breakage, strain, and necking could compromise electrical conductivity. Two methods were employed to detect electrode breakage after deformation: resistance measurements using a probe station and optical imaging using transmission microscopy. Breakage occurred in a small but nonzero fraction of electrodes, more frequently in thin electrodes. Necking and plastic deformation were never observed; rather, the mode of breakage seemed to be a straight fracture line along the edge of the channel. See Figure 2-9 for transmission images showing such a fracture line.

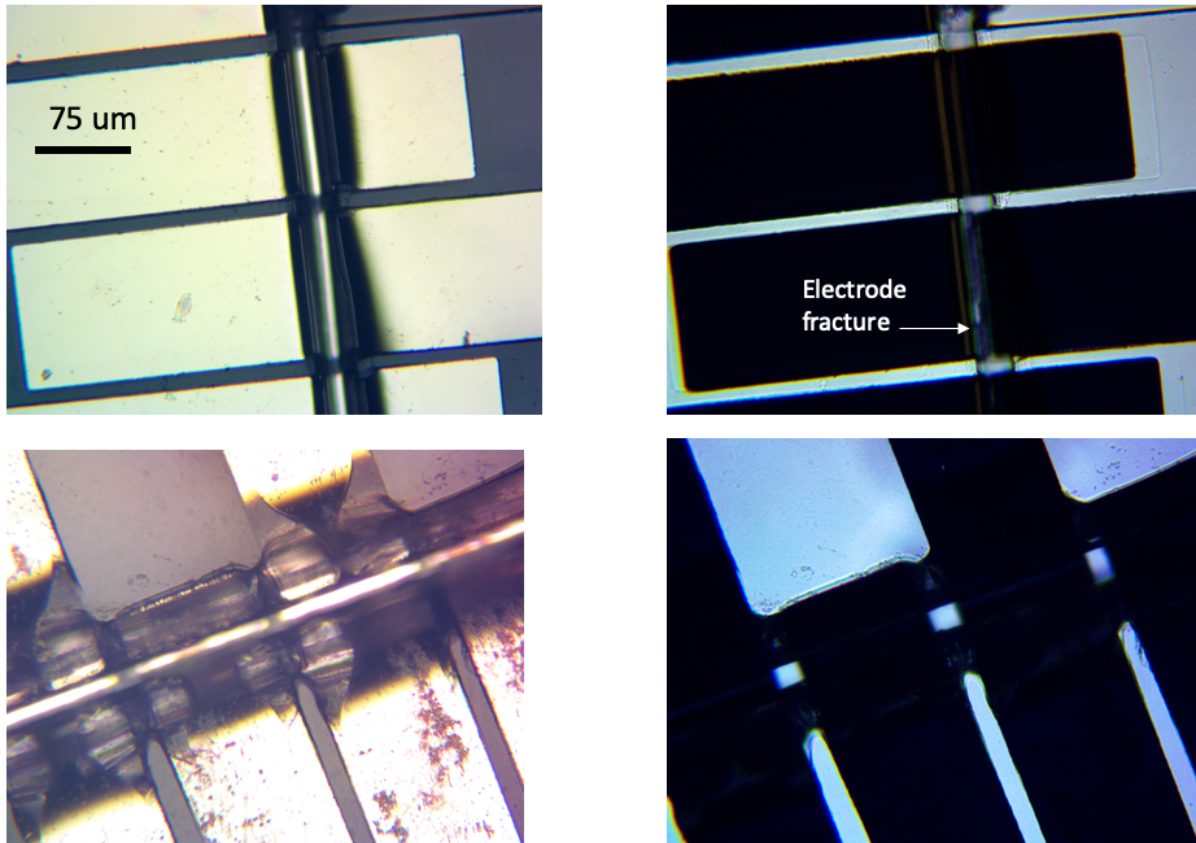


Figure 2-9: Transmission images of electrodes after deformation. A hairline fracture can be observed in the top left image.

Before and after deformation, measurements of resistance between the contact pads and the channel bottom electrode were made using an Everbeing EB-8 probe station. With channel depths up to 60 μm , no appreciable increase in resistance was detected during the embossing process, apart from a small fraction of electrodes which fractured during the process. Furthermore, the resistance of these samples was low overall, indicating that the quality of the electroplated nickel was high.

Chapter 2g: Bonding and Assembly

Another major challenge for thermoplastic microfluidics is the need to find a replacement for the plasma bonding methods available to PDMS-glass structures. Broadly speaking, there are two main adhesive-free strategies for bonding thermoplastics: thermal and solvent-assisted bonding. Both strategies essentially use the plastic itself as the adhesive by softening the surface layers of plastic and fusing them together using pressure, and therefore both strategies run the risk of feature loss should the “surface” comprise more than a few microns of material. Each process must therefore be tuned carefully in order to facilitate a strong bond while preventing excessive surface diffusion and loss of features.

Solvent bonding uses an immersion bath or vapor of solvent in which the thermoplastic is slightly soluble, such as methyl ethyl ketone or ethanol. The solvent solubilizes the surface of the plastic parts and allows these surfaces to fuse when brought into contact. UV or plasma treatment may be used to increase surface roughness and solubility and help facilitate bonding, and heat is also used during the pressure phase both to drive solvent evaporation and increase the diffusion of solvent into the plastic surface. Solvent bonding is typically a rapid and comparatively low temperature process, resulting in fast process time and low risk of channel collapse. However, the process is highly sensitive to surface energy and solvent concentration and using too much or too highly concentrated solvent can result in channel clogging as solubilized plastic is washed into the channel itself during the bonding process. However, proven and robust solvent bonding protocols exist for many thermoplastics; in particular, PMMA can be reliably bonded at room temperature by a mixture of 20% 1,2-dichloroethane and 80% ethanol. (Lin, Chao, and Lan 2007)

Thermal bonding uses heat and pressure rather than solubility to facilitate the interdiffusion of surface layers of polymer. In order to preserve the structure of the patterned plastic, the temperature must be lower than the glass transition temperature of the plastic, and therefore the pressures and times involved in this process are typically quite long. Additionally, even at these temperatures the plastic does exhibit a degree of viscous deformation and therefore this process can result in channel collapse especially for channels with a low aspect ratio. This process therefore presents a challenge for channel designs with a wide range of channel sizes on the same chip. Despite these challenges, thermal bonding is often the best option in the case where a plastic has no suitable solvent bonding process available. In particular, while we attempted a solvent-assisted polycarbonate bonding process using a mixture of 50% IPA and 50% methyl ethyl ketone as described in Paredes *et al.* (Paredes *et al.* 2015) we ultimately found the most reliable method for polycarbonate bonding to be a pure thermal process due to the narrow process window of this solvent-assisted process and the high glass transition temperature of polycarbonate. Polycarbonate chips were bonded at 135 degrees C and 900 PSI for 10 minutes. For patterns with large (>1mm) channels, where channel collapse was a concern, a lower temperature of 125 degrees C was used.

Chapter 2h: Potential of Parallel-Plate Devices for Impedance Cytometry

Impedance cytometry is a technique wherein a cell is subjected to an AC electric field and the impedance response of the cell and the surrounding fluid are measured. In theory, this technique allows for a variety of properties of cells to be measured depending on the chosen frequency regime, from simple counting or sizing of cells at low frequencies to measurements of the capacitance of the cell membrane or the permittivity of the cytosol at higher frequencies.

Generally, impedance cytometry operates in one of three regimes. This can be understood by analyzing the cell as an RC circuit consisting of a capacitor representing the cell membrane and a resistor representing the cytosol in parallel with a resistor representing the surrounding aqueous media (leaving aside the question of ionic shielding) (Sun, Bernabini, and Morgan 2010).

$$Z_{circuit} = \frac{1}{j\omega C_{media} + \frac{1}{R_{media}} + \frac{1}{Z_{cell}}}$$

Where Z_{media} is the complex impedance of the mixture, ω is the operating frequency, C_{media} and R_{media} are the capacitance and resistance of the media equivalent circuit, and Z_{cell} is the complex impedance of a shelled particle, which can be modeled as a resistor and a capacitor in series, with the values:

$$C_{cell} = \frac{9\Phi R \epsilon_{sh}}{4d} G_f \quad R_{cell} = \frac{4 \left(\frac{1}{2\sigma_{media}} + \frac{1}{\sigma_{cell}} \right)}{9\Phi G_f}$$

where Φ is the volume fraction occupied by the particle, ϵ_{sh} is the permittivity of the shell (the cell membrane), d is the thickness of the shell, G_f is the geometry constant of the system (for an ideal parallel plate capacitor, A/g where A is the plate area and g is the separation) and σ_{media} and σ_{cell} are the conductivity of the media and the cytoplasm respectively. The resistance and capacitance of the suspending media are likewise given by:

$$R_{media} = \frac{1}{\sigma_{media} \left(1 - \frac{3\Phi}{2}\right) G_f} \quad C_{media} = \epsilon_{media} \left\{1 - 3\Phi \left[\frac{\epsilon_{media} - \epsilon_{cell}}{2\epsilon_{media} - \epsilon_{cell}} \right]\right\} G_f$$

At low frequency, the capacitors charge fully and act as an open circuit, meaning that the cell essentially behaves as an insulator. The DC resistance of the sensing volume is as follows:

$$Z_{circuit} = \frac{1}{\frac{1}{R_{media}}} = \frac{1}{\sigma_{media} \left(1 - \frac{3\Phi}{2}\right) G_f} = \frac{1}{\sigma_{media} - \frac{3\Phi}{2} \sigma_{media} G_f}$$

In other words, the DC conductivity ($1/Z_{circuit}$) of the sensing volume consists of a constant part which depends only on the DC conductivity of the media plus a part that varies linearly with the volume fraction of the cell. This measurement can be used to size cells based on the volume fraction. The sensitivity of this method is obviously limited by the volume fraction, as well as by the contrast between the conductivity of the cell and the background media. Therefore, for single cell measurements, it is important to use a sensing volume that is not much larger than the size of the cell. This is commonly achieved by physically confining the cell and the electric field using a narrow channel filled with a conductive fluid. This common cell counting technique is also known as the Coulter counter principle.

At moderate frequencies where the period of the applied field is of the same order as the RC time constant of the membrane capacitor, the full expression for the equivalent circuit above is used. This measurement can also act as a proxy for cell size due to the dependence of the cell membrane capacitance on the membrane surface area, and can also be used to distinguish types of cells based on membrane composition and permeability. Like before, the capacitance of the particle is linearly dependent on the volume fraction, and the media capacitance can be separated into a component dependent only on the capacitance of the cell (and the geometry constant) and a component that varies linearly with the volume fraction.

At high frequencies, the capacitor does not charge appreciably and therefore acts as a short circuit. This allows the measurement to directly probe the cytosol, and the resulting mixture conductivity is a volume-weighted mixture of the media and cytosol high-frequency conductivities, consisting once again of a constant part dependent on the media conductivity only and a variable part that depends linearly on the volume fraction:

$$Z_{circuit} = \frac{1}{\frac{1}{R_{media}} + \frac{1}{R_{cell}}} = \frac{1}{\sigma_{media} \left(1 - \frac{3\Phi}{2}\right) G_f + \frac{9\Phi G_f}{4 \left(\frac{1}{2\sigma_{media}} + \frac{1}{\sigma_{cell}}\right)}}$$

$$\frac{1}{Z_{circuit}} = \sigma_{media} + \frac{3\Phi G_f}{2} \left(\frac{3}{2 \left(\frac{1}{2\sigma_{media}} + \frac{1}{\sigma_{cell}}\right)} - \sigma_{media} \right)$$

Chapter 2i: Field Homogeneity and Electrode Geometry

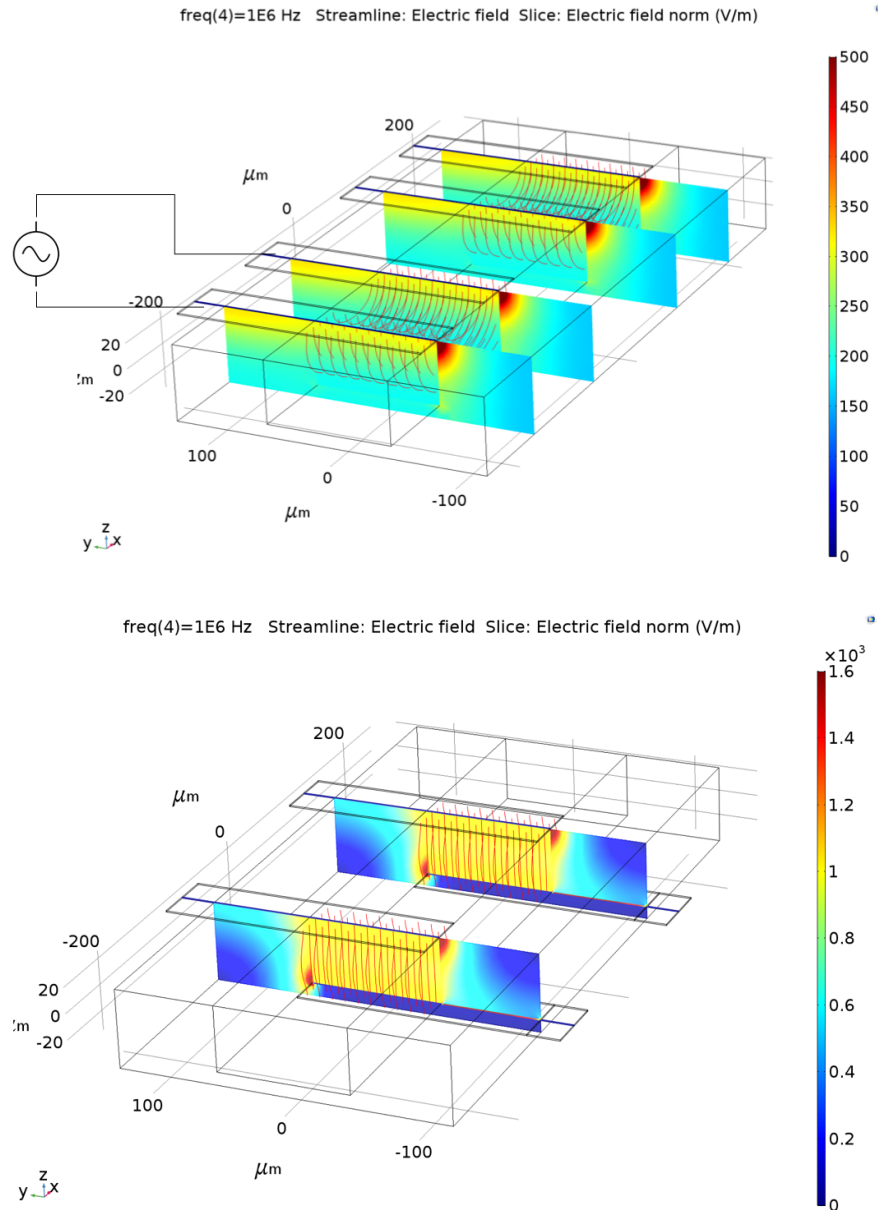


Figure 2-10: Simulated electric field geometries for in-plane (top) and parallel-plate (bottom) electrode geometries. Fabrication constraints (electrode and channel size and spacing) are held constant, as is applied voltage. Note the increased spatial uniformity of the field in the second case.

In all three regimes described in the previous section, the difference in conductivity between the signal and background depends, as expected, on the volume fraction, meaning

that high volume fraction is necessary for high contrast. Furthermore, the magnitude of the signal depends on the local field strength. This represents a challenge in the case that the electric field varies within the measurement volume, as the measured signal would reflect not only the desired measurement properties (cell size, membrane permeability, etc.) but also the position of the cell in the channel. This means that either the cell must be confined to a particular region by size exclusion (which runs the risk of channel clogging) or flow focusing (which necessitates additional control channels and is very sensitive to perturbations in fluidic resistance), or that the position of the cell must be measured e.g. optically, which necessitates additional measurement equipment, negating the advantage of a compact, label-free sensor.

Figure 2-10 and 2-11 show simulated (COMSOL Multiphysics) electric field geometries for two different configurations of electrodes: coplanar and parallel-plate. These geometries are subject to the same fabrication constraints: lateral feature size and channel depth. Many extant microfluidic impedance cytometers use a coplanar electrode geometry due to the difficulty of incorporating more than one electronics layer; for example, a typical PDMS-based microfluidic impedance cytometer will consist of a single layer of unpatterned glass with sputtered gold electrodes and one or more layers of PDMS with fluidic channels. In the coplanar case, the electric field varies with distance from the electrodes: the cell will perturb a more concentrated electric field the closer the cell is to the electrodes. In contrast, a parallel-plate geometry features a homogeneous electric field everywhere between the electrodes as long as the electrodes extend beyond the walls of the channel. Additionally, the electric field strength is higher and the sensing volume smaller for the same fabrication limitations, because the electrode separation is limited by the depth of the channel (typically a much easier parameter to minimize) rather than the lateral feature size. These considerations make the parallel-plate geometry more desirable for impedance cytometry applications in virtually every case, at the cost of much more difficult fabrication using traditional soft lithography techniques.

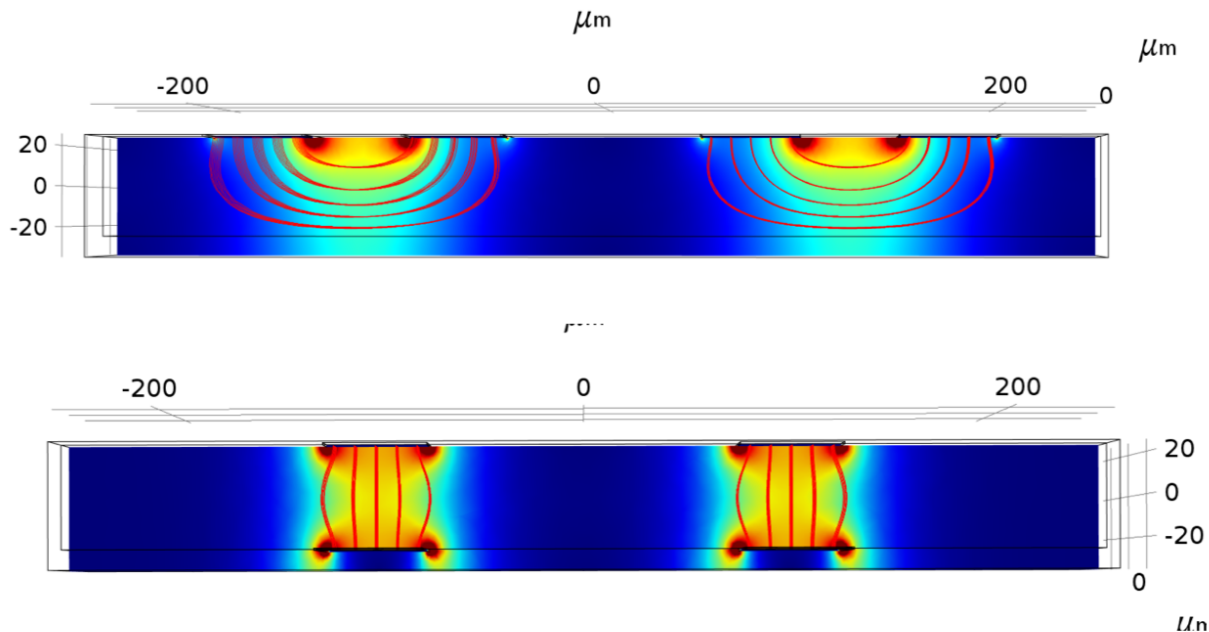


Figure 2-11: Simulated electric field geometries for in-plane (top) and parallel-plate (bottom) electrode geometries – side view.

Chapter 2j: Parallel Plate Electrode Fabrication

A few examples of micromachined parallel-plate impedance cytometers exist in the literature. These rely on complex, multistep process flows involving deposition of seed layers and in-situ electroplating or metal etching, or multilayer glass- or silicon-based microfabrication. These processes are expensive and time-consuming, limiting their application to diagnostic devices with strict cost per consumable requirements. The embossing-based electrode deformation process described in chapter 2 of this work can be applied to the fabrication of low-cost parallel-plate impedance cytometers in plastic microfluidic chips.

See Figure 2-12 for a schematic of this process. First, two electrodes are patterned and embedded into thermoplastic using the previously demonstrated method. A microchannel mold is then aligned with one of the electrode layers. The channel mold is embossed into the plastic layer, deforming the electrode and producing the three-dimensional deformed electrode pattern described above. This structure is then aligned with the undeformed electrode layer and the two layers of plastic are bonded, producing a pair of electrodes separated by an embossed plastic channel. Alignment of electrode pairs by eye under a microscope (without any dedicated alignment marks) produced an alignment mismatch of approximately 20 μm – this could be improved substantially with the inclusion of metal alignment marks and/or mechanical alignment features.

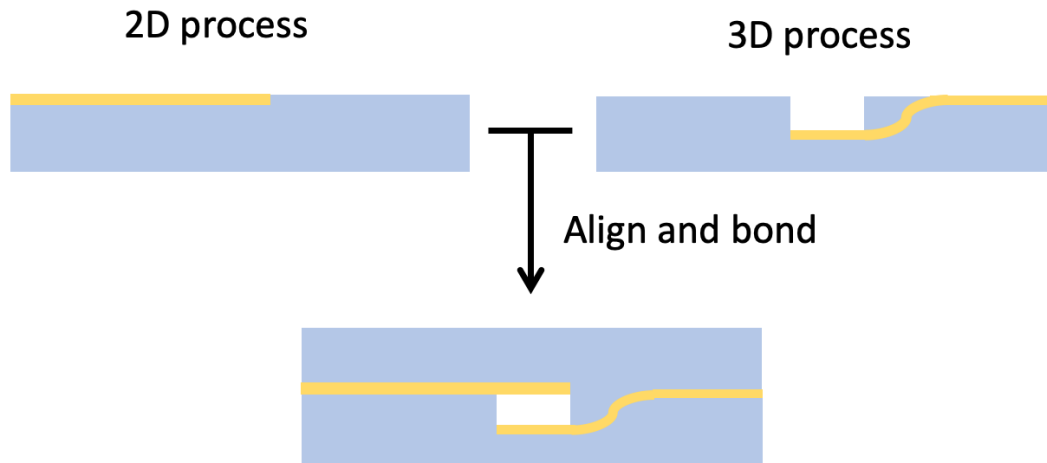


Figure 2-12: Schematic of parallel-plate electrode fabrication process

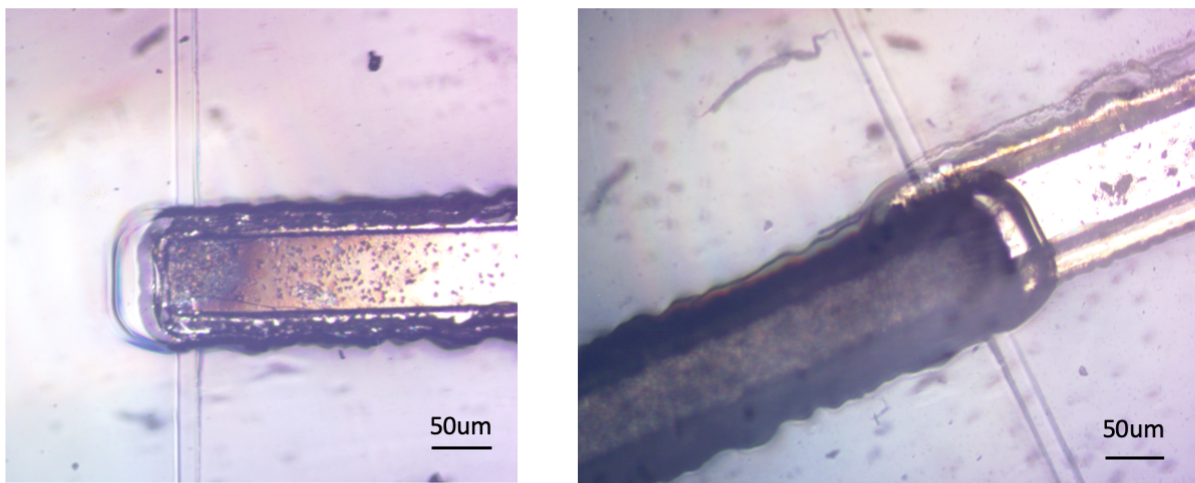


Figure 2-13: Parallel-plate electrodes Left: Before bonding Right: After bonding

Chapter 2k: Discussion

The fabrication method discussed above is able to produce out-of-plane nickel electrode pairs in contact with a microfluidic device using a fairly simple fabrication process and inexpensive materials. Using electro- or electroless plating methods these electrodes could easily be coated in situ with gold, which adheres well to electroplated nickel and which could be further functionalized with a variety of biomolecules for electrochemical sensing.

Considerable work is still needed to characterize the performance of these systems including the sensitivity limits and time constant of the impedance cytometer, but this geometry demonstrates considerable promise when compared to in-plane electrode pairs. The equipment and materials necessary are widely available and inexpensive and most laboratories with PDMS soft lithography capability could conceivably implement this fabrication process.

Deformation-based patterning of three-dimensional embedded metal microstructures is an area of microfabrication research that remains largely unexplored. The simple structures described in this chapter are suitable for additional applications which are not described in this work, including microheaters, solenoids, and dielectrophoretic traps. One additional use of this embedded electrode process is described in the following chapter. Additional deformation modes, perhaps using three-dimensional molds, are also possible. Pursuit of this area of research could yield a variety of active devices that are easily integrated with plastic microfluidic chips.

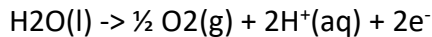
Chapter 3: Active Electrolysis Pump using Embedded Electrodes

Chapter 3a: Introduction

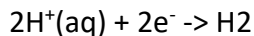
Microfluidic devices in laboratories and some point-of-care settings can use off-chip power sources such as syringe pumps or compressed gas to drive flow. However, on-chip pumps are desired for some applications in drug delivery which require extremely compact devices. For devices that must be in contact with patient samples or biologics, single-use devices are preferred and therefore the pumps must be designed with cost and disposability in mind.

Chapter 3b: Theory & Design of Electrolysis Pump

The working principle of the pump is the splitting of water into hydrogen and oxygen gas by electrolysis, one of the earliest observed and documented electrochemical processes dating back to 1789 (De Levie 1999). This process occurs in an electrochemical cell consisting of a positively charged anode and a negatively charged cathode suspended in an aqueous solution. Water is oxidized at the surface of the anode, losing two electrons to the anode and forming oxygen gas and dissolved hydrogen ions:



The corresponding reduction half-reaction takes place at the surface of the cathode, where dissolved hydrogen ions are reduced to hydrogen gas:



Therefore, an ideal electrochemical cell operating at perfect efficiency would yield 0.25 molecules of oxygen gas and 0.5 molecules of hydrogen gas per electron, or 5.18 μmol of hydrogen gas and 2.59 μmol of oxygen gas per coulomb.

Because the oxidation of water into oxygen gas and hydrogen ions is thermodynamically unfavorable, this reaction requires an electrical potential. The electrical potential difference between the cathode and anode required for an electrochemical reaction at standard temperature and pressure and at 1.0 M concentration of each aqueous species is referred to as the standard potential of the cell; the standard potential for the electrolysis of water is -1.23 V (Böhm, Olthuis, and Bergveld 1999). Cell potentials under other conditions can be calculated using the Nernst equation:

$$E_{\text{cell}} = E_{\text{cell}}^0 - \frac{RT}{nF} \ln(Q)$$

where E_{cell} is the cell potential, E^0_{cell} is the standard cell potential, n is the valence number, F is Faraday's constant, R is the molar gas constant, T is the temperature, and Q is the reaction quotient (the equilibrium expression in terms of the initial concentrations of the reactants). In this case, because the reaction species are water and hydrogen ions, the potential at pH 7 in the ideal case is unchanged at -1.23 V. In a real electrochemical cell, the required voltage will be higher than -1.23 V; this increase in potential is due to energy losses such as competing reactions (for instance, oxidation of metal electrodes and reduction of dissolved metal species) and thermal losses both within the cell and through parasitic resistances (e.g. contact resistance). Competing reactions will also reduce the efficiency of the electrochemical cell as electrons are instead captured in competing reactions.

To a first approximation, neglecting any pressure generated by fluid flow and assuming an ideal gas, the resulting volume of liquid displaced per unit of charge can be calculated from the ideal gas law, using the reaction stoichiometry calculated earlier (V = volume of fluid generated, P_{atm} = atmospheric pressure, n = moles of gas generated, R = molar gas constant, T = temperature in K):

$$V = \frac{nRT}{P_{atm}} = \frac{\left(5.18 \frac{\mu\text{mol}}{\text{C}}\right) (8.314 \text{ J K}^{-1} \text{ mol}^{-1}) (298 \text{ K})}{101.3 \text{ kPa}} = 1.26 * 10^{-4} \text{ L/C}$$

or 126.7 $\mu\text{L/s/A}$, in terms of current. This relationship is only valid for short timescales, as the growing gas bubbles will reduce the exposed surface area of the electrodes and therefore slow down the overall reaction rate, eventually stopping the reaction. The maximum displacement delivered by the pump is therefore dependent on the total surface area of the electrodes. In order to achieve maximum surface coverage in a compact footprint, an interdigitated electrode pattern was chosen. See Figure 3-1 for a schematic of the device.

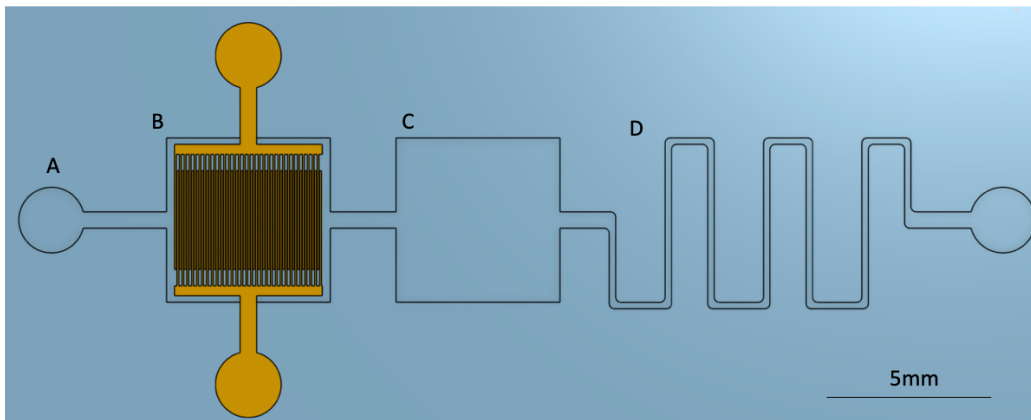


Figure 3-1: Schematic of electrolysis pump. A: loading port. B: electrolysis chamber C: reservoir D: serpentine for optical flow rate measurement

The device consists of a loading port (A) to fill the reservoirs with fluid, an electrolysis chamber (B) with interdigitated electrodes, a fluid reservoir (C) separating the electrolysis chamber from the delivery channel in order to prevent leakage of gas into the channel, and a serpentine delivery channel (D), initially empty, which is used to measure the delivery volume based on the movement of the liquid-air interface in the channel. Initial designs used a square electrolysis chamber in order to maximize electrode area, but this resulted in fluid becoming trapped in the corners of the chamber in initial tests and later designs, including those characterized below, used circular chambers. IDE arrays varied in electrode size and spacing, though all electrodes were 5 μm thick. The dimensions of the channels were as follows: reservoirs: 5 mm diameter, output serpentine: 250 μm wide, channel depth: 50 μm .

Chapter 3c: Fabrication of Electrolysis Pump

Electrolysis pumps were fabricated using the hot embossing process with embedded electrodes as described in the previous chapter. Nickel molds (50 μm channel depth) were patterned using Riston GM130 (nominal thickness 75 μm , measured thickness after lamination and patterning $\sim 60\mu\text{m}$) and electroplating, annealed, and then embossed into polycarbonate. Electrodes were patterned using S-1818 photoresist and electroplated to a target thickness of 5 μm , then transferred into an unpatterned polycarbonate sheet via embossing as previously described. The inlet, outlet, and access holes for the solder pads were then drilled in the sheet containing the channels and then the two pieces of plastic were bonded together by thermal fusion at 125 degrees C and 500 PSI, as described in Chapter 2d. The lower bonding temperature (and correspondingly longer bonding time) were chosen as a result of the large cavities in the device, which risked collapse if the plastic was close to its glass transition temperature. Inlets and outlets were anchored into the drilled holes with catheter pins cut to length and then sealed with UV-curing adhesive (Bondic). Electrical leads were connected to exposed metal pads using silver epoxy.

Chapter 3d: Characterization of Flow Rates

Using a syringe pump, the devices were loaded with deionized water with trace amounts of yellow dye until the pump section and the reservoir were full, while the microchannel remained empty, at which point flow was stopped, but the syringe pump remained connected to the inlet to control pressure. The electrical leads were then connected to a DC power supply and the applied voltage was steadily increased until electrolysis was observed, at which point the voltage and current were noted and the flow of fluid through the channel was recorded on a microscope camera (see Figure 3-3). The displacement of the fluid per frame was then measured in ImageJ and used to calculate the flow rate (Q = flow rate, v_{avg} = average fluid velocity, A = cross-sectional channel area):

$$Q = v_{avg}A$$

The flow rate was then integrated in order to evaluate the total delivery volume. See Figures 3-4 and 3-5 for charts of the calculated flow rate and delivery volume for 3 devices, all of which have circular chambers and IDE arrays which are 90 μm across and spaced 75 μm apart. The total delivered volume is similar for all three devices, though the kinetics of delivery are different. This is likely due to variation in the capillary force in each channel, as the channels were not treated with a surface coating and therefore likely exhibited a variation in surface energy.

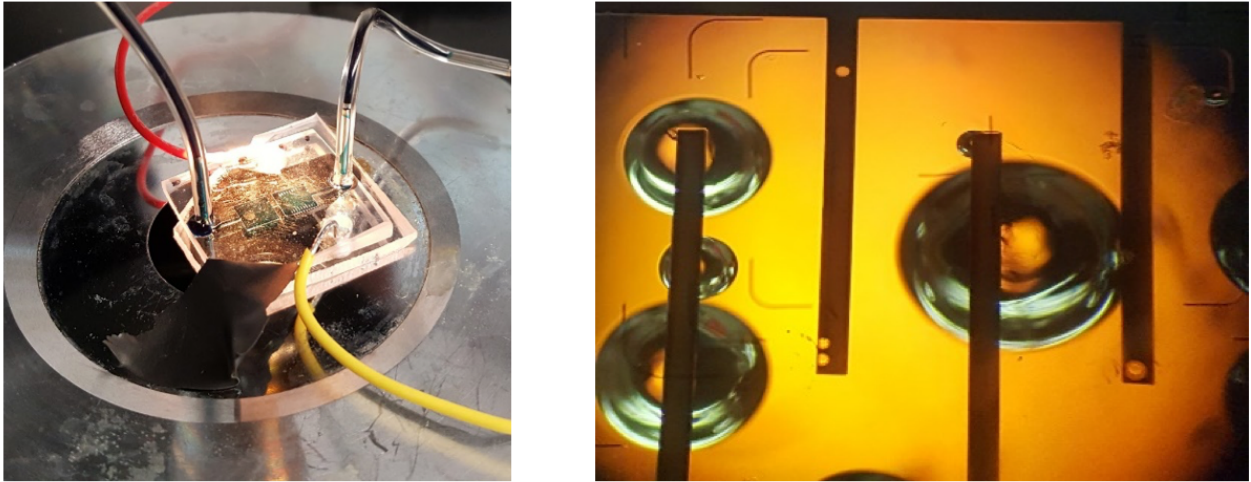


Figure 3-2: Experimental setup. Left: Packaged device with electrical and fluidic leads connected. Right: Electrodes during device operation.

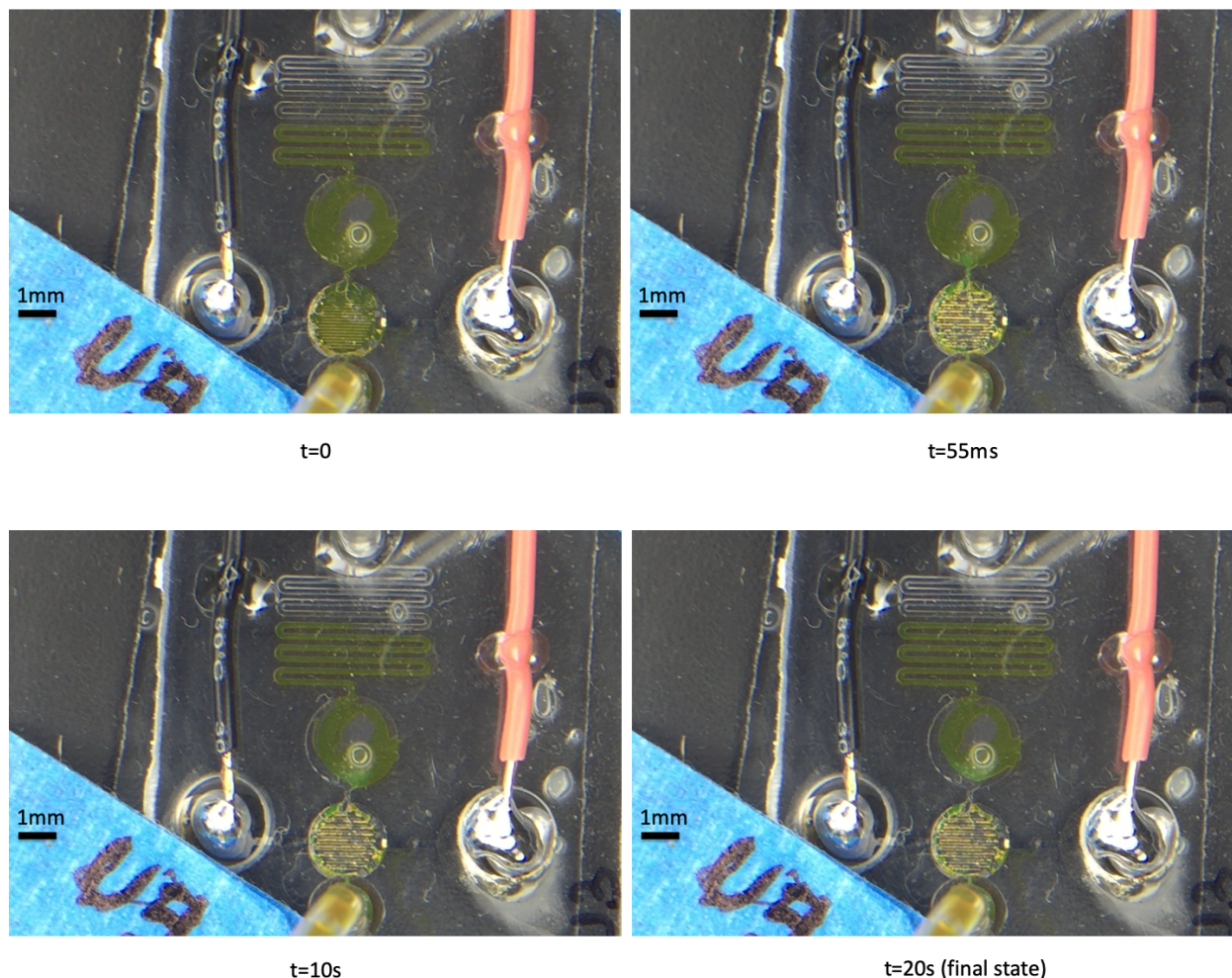


Figure 3-3: Images of a device during flow measurement experiment. Top left ($t=0$) is defined as the moment at which the redox reaction begins. Flow rate spikes initially and quickly decays.

Trial	Operating Voltage	Operating Current (initial)	Predicted Flow Rate
1	1.7 V	4.8 mA	0.61 $\mu\text{L/s}$
2	1.7 V	4.5 mA	0.57 $\mu\text{L/s}$
3	1.6 V	8.3 mA	1.05 $\mu\text{L/s}$

Table. 3-1: Measured voltage and current during operation of the three devices plotted below.

Volumetric Flow Rate vs Time

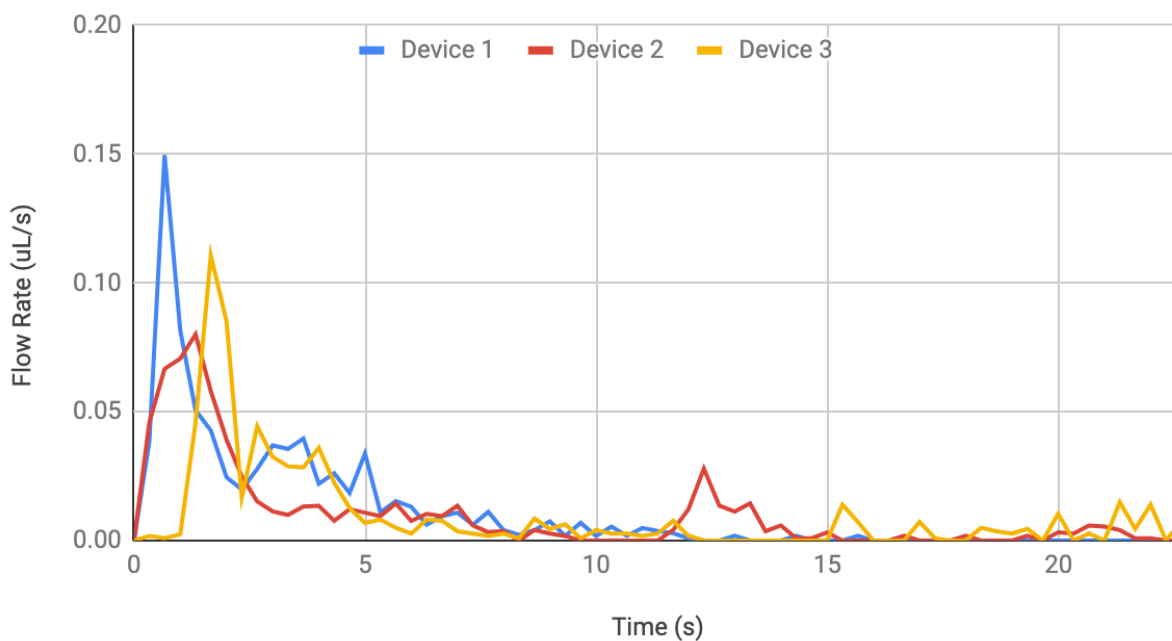


Figure 3-4: Volumetric flow rate over time for 3 devices. Flow rate peaks within a few seconds and then rapidly tapers off as electrode area is occluded by growing bubbles.

Total volume delivered vs time

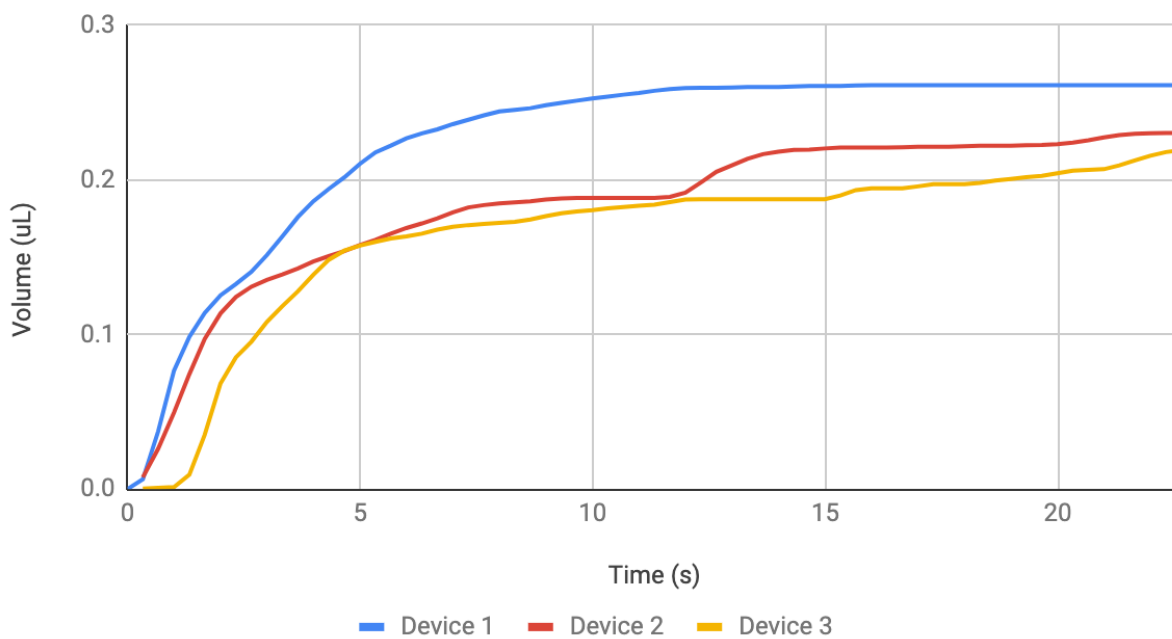


Figure 3-5: Total volume delivered over time.

Chapter 3e: Discussion

The measured flow rate in all three devices differed substantially from the predicted flow rates based on the operating current. This is likely due to a combination of measurement error and of several shortcomings of my analytical model. Firstly, the nickel microelectrodes were observed to oxidize during the course of the operation; this is to be expected, as the standard potential of nickel is lower than that of water. Electrons consumed in the reduction of Ni^{2+} to metallic nickel would have slowed the rate of the electrolysis reaction. Gold-coated electrodes will be necessary during further development of these devices. Secondly, my calculations used the atmospheric pressure, neglecting pressure drops due to capillary forces and viscous losses, which were likely substantial during the operation of these devices.

The total delivered volume was similar in all three devices and reached a maximum of 0.26 μL . This could be considerably improved in a number of ways, notably by using noble metal electrodes and by increasing the available reaction area by increasing the electrode surface area. Furthermore, as the bubbles generated by the operation of this pump remain in contact with the electrode surface, should noble metal electrodes be used the pump could operate in a reciprocal fashion by reversing the applied voltage and therefore the reaction, in order to drive period flow.

A few improvements to this design could make it suitable as a pressure source for a microfluidic chip. However, for drug delivery applications, a pump that could drive a larger volume with lower power requirements is desirable. Such a device is described in the next chapter.

Chapter 4: Chemically-Actuated Microjet Injector

Chapter 4a: Introduction

Electrically driven pumps are not necessary in applications which require only a single delivery of fluid, in particular if extremely compact power sources are required. One such application is oral vaccination. Vaccines and other drugs with low bioavailability, as well as drugs with small dosage and time windows such as insulin, are typically delivered by injection instead of orally because the protective mucosal layer of the digestive tract acts as a potent barrier to the diffusion of most bioactive materials. The gastrointestinal mucosa contains a layer of epithelial cells that continuously secrete mucus gel at a rate of multiple microns per second, reaching an equilibrium gel thickness of up to 300 μm for the intestinal mucosa or 800 μm for the buccal mucosa (Cone 2009). This effectively excludes most large and/or hydrophilic molecules from reaching the bloodstream. However, if delivery of antigen to the mucosal epithelium can be achieved, this would be a highly effective way of inducing an immune response as it could stimulate both systemic and mucosal immunity (Ma *et al.* 2014).

Attempts to bypass the gastrointestinal mucus layer have been made using both chemical means (drug formulations that increase the diffusivity of drugs (Khanvilkar, Donovan, and Flanagan 2001), or encapsulate drugs in delivery vesicles that promote absorption (Li, Nielsen, and Müllertz 2012)) and mechanical means (microneedle (Prausnitz, Goma, and Li 2019) or jet-based displacement of mucus). Mechanical mechanisms that target the most absorptive section of the digestive tract, the small intestine, must be compact enough to pass through the digestive tract and must have a built-in timing or sensing mechanism to guarantee drug delivery at the correct time. It is in this problem that we find an application for a compact single-use pump.

Chapter 4b: Functional Principle of Pump

The microjet vaccination device (Aran *et al.* 2017) consists of a small 3D-printed capsule containing three chambers (see Figure 4-1). The inner two chambers are separated by a movable piston and contain the vaccine solution and a dry propellant consisting of citric acid and sodium bicarbonate. The vaccine chamber is open to the outside through a narrow (250 μm diameter) nozzle which is capped by a thin layer of epoxy. The outer chamber contains water, and is separated from the propellant chamber by a polymer membrane that slowly degrades when in contact with water. This acts as the timing mechanism, which begins when the assembly containing the inner chambers is inserted into the outer chamber. Upon degradation of the membrane, the dry citric acid and sodium bicarbonate dissolve in the water and undergo an acid-base reaction, forming sodium citrate, water, and carbon dioxide gas. The expansion of the gas moves the piston, causing the vaccine solution to pressurize and break through the epoxy cap, releasing a high-pressure jet of vaccine solution.

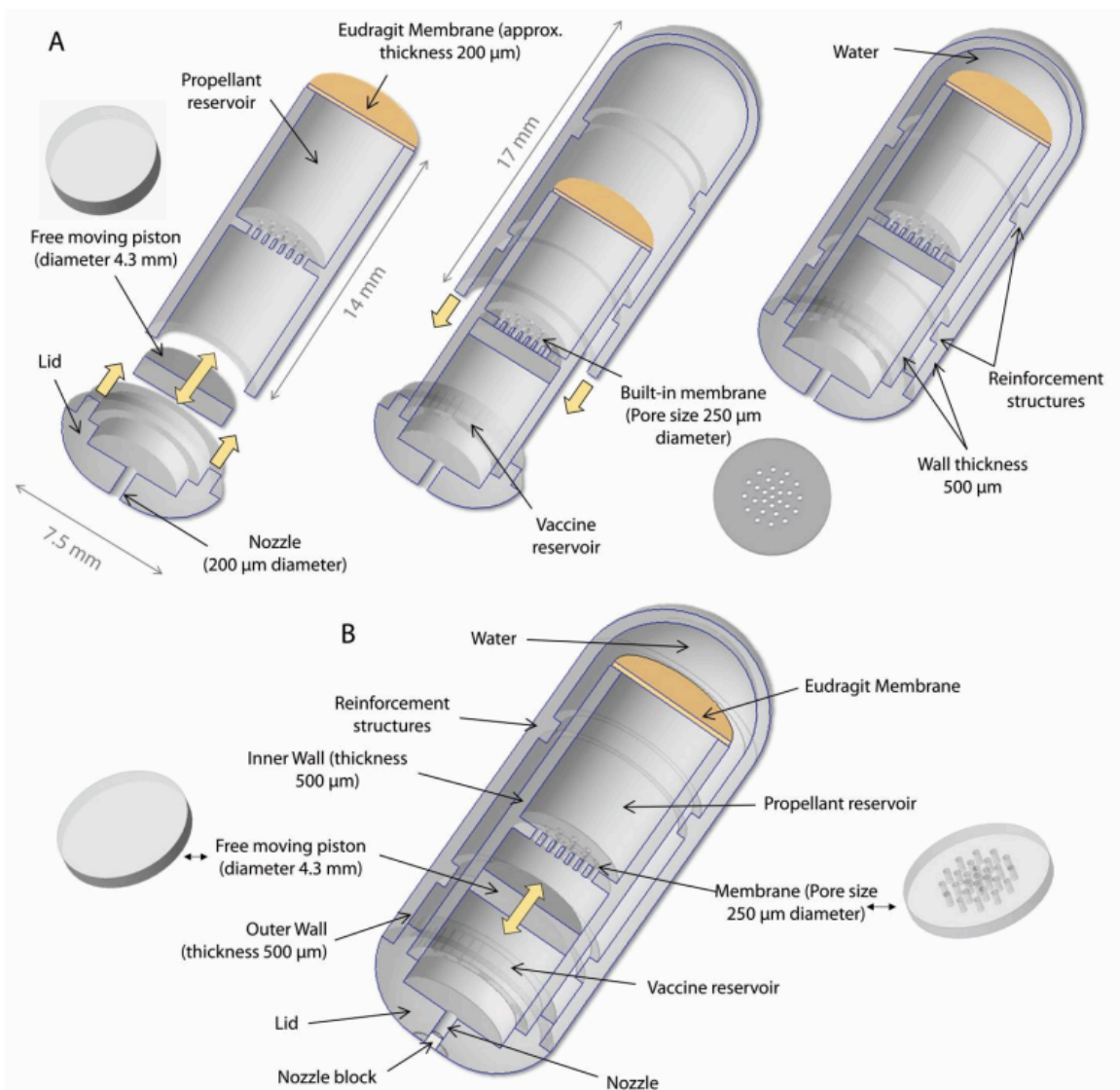


Figure 4-1: Microjet injector architecture. A. Assembly of microjet injector. After propellant is sealed in propellant reservoir by Eudragit membrane, piston and nozzle cap are inserted. Vaccine reservoir is loaded with vaccine through pore, which is then sealed with a layer of epoxy. Finally, just before administration, the outer jacket, filled with water, is attached, beginning the timed breakdown of the membrane.

In theory, the timing mechanism could be replaced with a polymer membrane that is sensitive to a particular pH or to particular digestive enzymes for targeted release in the small intestine. However, we chose to first prove the principle by using a simple time delay mechanism and targeting the buccal mucosa instead. The buccal mucosa (the inside of the cheek) is much easier to access, but is thicker and more viscous than the small intestine mucosa, and a delivery mechanism which can successfully bypass the buccal mucosa should also function to bypass the intestinal mucosa if targeted correctly.

Chapter 4c: Microjet Simulations

To support the design of the device I conducted computational fluid dynamics simulations in order to attempt to determine the effect of pressure on mucosal layer penetration. A three-phase fluid model of the jet was conducted in ANSYS Fluent, with a 2D axisymmetric geometry and a transient pressure-based solver, with phases representing the drug-carrying fluid, the fluid in the buccal or intestinal cavity, and the mucus layer. Diffusion of drug was assumed to be negligible over the timescale of the simulation, which is supported by the very high Peclet number of $\sim 10^7$, indicating that convection dominates over diffusion in this time scale:

$$Pe = \frac{LU}{D} \approx \frac{8 * 10^{-4} m * 1 m s^{-1}}{10^{-10} m^2 s^{-1}} = 8 * 10^6$$

Where Pe is the Peclet number and L , U , and D are the characteristic length, velocity, and diffusivity of the system. The mucus layer was assumed to be 800 μm initially, representing the thickness of the buccal mucosa, which is considered a worst-case scenario for drug delivery. The mucus was modeled as a power-law shear thinning fluid with the viscosity depending on the shear rate according to the following equation:

$$\eta = k\dot{\gamma}^{n-1}$$

Where the consistency index $k = 1.412 \text{ kg s}^{-2}/\text{m}$ and the power law index $n = 0.15$, η is the viscosity and $\dot{\gamma}$ is the shear rate. This model is a simplification of a more complex viscoelastic model of mucus rheology and are curve fit from rheology data found for gastrointestinal mucus in the literature (Lai *et al.* 2009). It is therefore important to note that these simulations only represent an approximation of jet behavior in a particular regime, but are still useful for informing design decisions within that regime. The nozzle is by a pressure boundary condition 250 μm in diameter positioned 125 μm away from the surface of the mucus layer surrounded by a rigid wall (see Figure 4-2 for simulation geometry detail). The experimentally measured pressure of the jet was 30 kPa, so simulations were conducted using 10 and 30 kPa boundary conditions. In both conditions, the jet quickly (0.4 ms-0.6 ms) penetrated the mucosal layer and the local pressure at the epithelial surface reached the jet pressure (see Figure 4-3). Elevated pressure at the endothelium has been associated with enhanced tight junction permeability (Tokuda *et al.* 2009) so this could serve to further increase drug uptake.

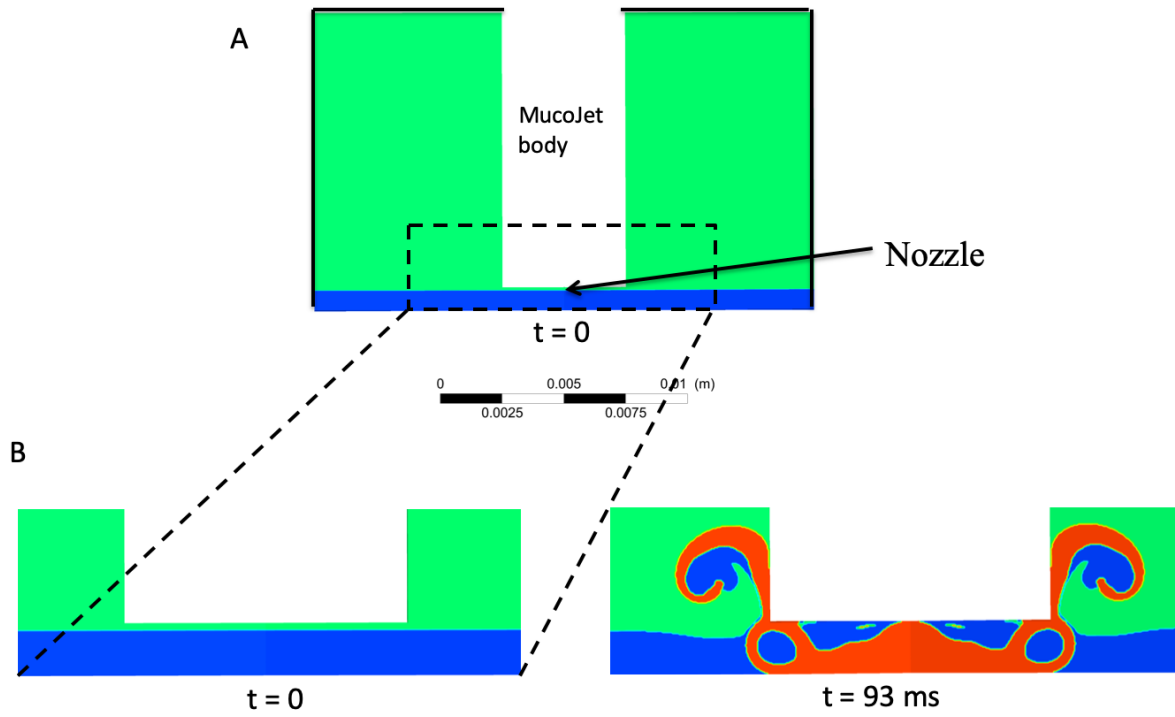


Figure 4-2: Simulation geometry. Colors represent fluid phase with the majority volume fraction. Green = water, blue = mucus, red = drug solution.

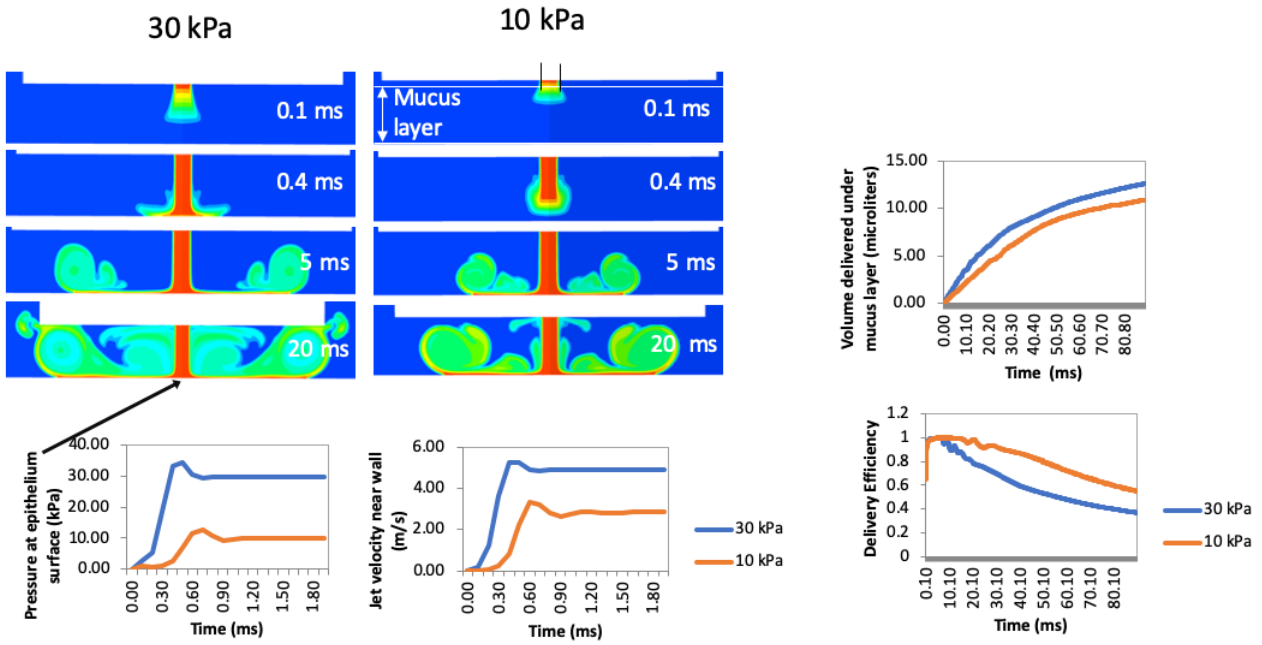


Figure 4-3: Output metrics from microjet simulations. Top left: Heatmaps of drug volume fraction over time at 2 different nozzle pressures (30 and 10 kPa). Bottom left: Pressure at target location (indicated by arrow). Bottom middle: Jet velocity, measured at the midpoint between the nozzle and the epithelium wall. Top right: Total volume of drug delivered to mucus layer over time. Bottom right: Delivery efficiency (drug within mucus layer/total drug delivered) over time.

During the delivery process, drug is lost to the surrounding fluid as the elevated pressure at the delivery site drives fluid away from the surface, seen in the laterally expanding vortices in Figure 4-2. A simple metric of delivery efficiency can be evaluated as the fraction of delivered drug that remains within the mucus layer as opposed to that lost into the lumen. This fraction decays over time and does so more quickly at higher pressure. Because the drug fluid was delivered quickly to the epithelial surface at one third of the operating pressure of the device in these simulations and because higher pressure will result in higher drug losses over the short term, these simulations suggest that the pressure generated by this design is more than sufficient for its operation and that an even smaller volume of propellant could be used in future designs.

Chapter 4d: In vitro Investigation using Porcine Buccal Mucosa

In order to validate these results experimentally, we carried out an experiment in which Ovalbumin (OVA) was delivered to fresh porcine buccal tissue in a Transwell assay. Porcine buccal tissue was obtained from pig heads obtained from a local slaughterhouse (Marin Sun Farms Inc.) and transferred to the laboratory in ice-cold Krebs-Ringer buffer. The top 0.5 mm of the mucosa was removed using a tissue slicer (Fisher Scientific) and was cut into 7mm circular

specimens using a biopsy punch. The tissue sample was then placed onto a polycarbonate Transwell membrane (Sigma-Aldrich) as shown in Figure 4-5. OVA-fluorescein conjugate was delivered to the surface of the buccal tissue using the microjet device (treatment, n=3) or with a micropipette (control, n=3). Samples taken from the basolateral media every 30 seconds were analyzed for OVA-fluorescein content using a microplate reader.

Figure 4-5 shows OVA-fluorescein concentration in the basolateral media normalized to the delivered concentration (3 mg/ml). The treatment group exhibited significantly ($p < 0.003$, one-tailed t-test assuming unequal variance) higher concentration than the control group at all time points from 30 to 180 minutes. These results were further validated by in vivo experiments carried out by my coauthors in rabbits, in which anti-OVA IgG and IgA titers in the bloodstream, Peyer’s patch, lymph nodes, and buccal mucosa were found to be higher in rabbits treated with the microjet device than in control rabbits with drug solution delivered orally (Aran *et al.* 2017).

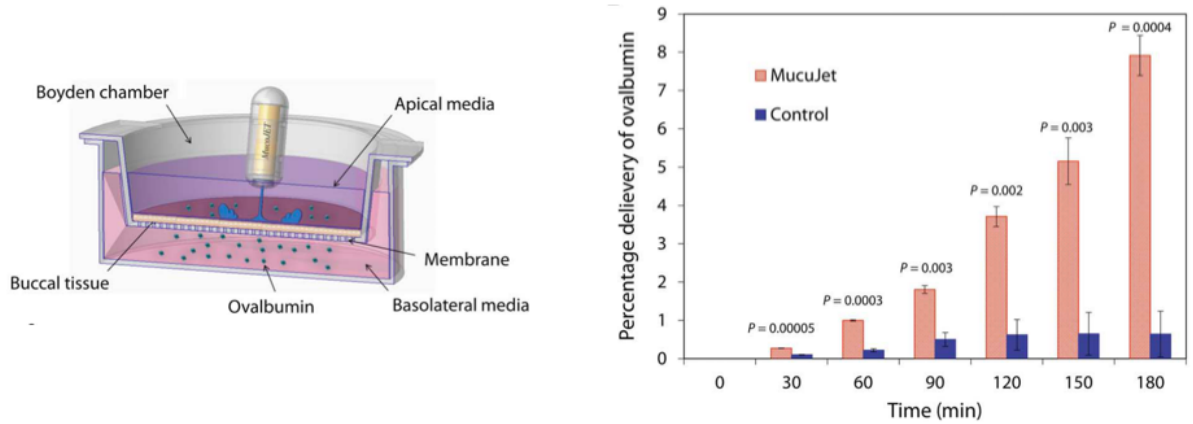


Figure 4-5: In vitro investigation of OVA-fluorescein delivery in porcine buccal mucosa. Left: Schematic of experimental setup. Right: OVA-fluorescein concentration in basolateral media as measured by microplate reader (normalized to delivery concentration).

Chapter 4e: Discussion

The results from the in vitro experiment as well as the in vivo experiments carried out by my colleagues validate the result of the simulation that this pump design is capable of generating pressures capable of penetrating the mucosal layer and delivering a substantial dose of a biomolecular payload to the buccal tissue. The intestinal mucosa is substantially thinner and less viscous than the buccal mucosa, and the epithelium in the duodenum is more permeable than the buccal tissue, so this device would also be suitable for intestinal drug delivery given some minor geometric modifications to orient the pore perpendicularly to the long axis of the pill and an accurate timing mechanism. Future studies of this device architecture will ideally refine the timing mechanism to achieve intestinal delivery.

These results show that compact, internally-powered fluidic control systems can be used to great effect, even if the mechanism is single-use. 3D-printed chemically-driven pumps with moving parts have potential for other applications including diagnostics, sample collection, and microswimmers. For complex, multi-use flow control and particle sorting, alternative strategies can be used such as that discussed in the following chapter.

Chapter 5: Compact, Electrically Controlled Micromagnetic Actuators for Microfluidics

Applications

Chapter 5a: Introduction

Magnetic bead cytometry has recently become a popular method for cell sorting and manipulation, due to the comparatively low cost of magnetic functionalization compared to fluorescent tagging. However, magnetic actuators suffer from similar scaling challenges to those discussed earlier in this work. Strategies for magnetic trapping based on external permanent magnets (Sinha *et al.* 2007) or micron-scale soft magnetic structures actuated by external magnetic fields (Murray *et al.* 2016) are simple to implement and energy-efficient, but cannot be used to address trapping sites individually at the microscale. Miniaturized electromagnets (Shen, Yamahata, and Gijs 2008) are energy- and heat-inefficient due to their reliance on high current and the scaling of resistance with cross-sectional area. Multiferroic technologies, which take advantage of strain-mediated coupling between magnetic and piezoelectric materials, are a potential candidate for a compact, locally addressable, and energy-efficient actuator that can be integrated with a microfluidic device.

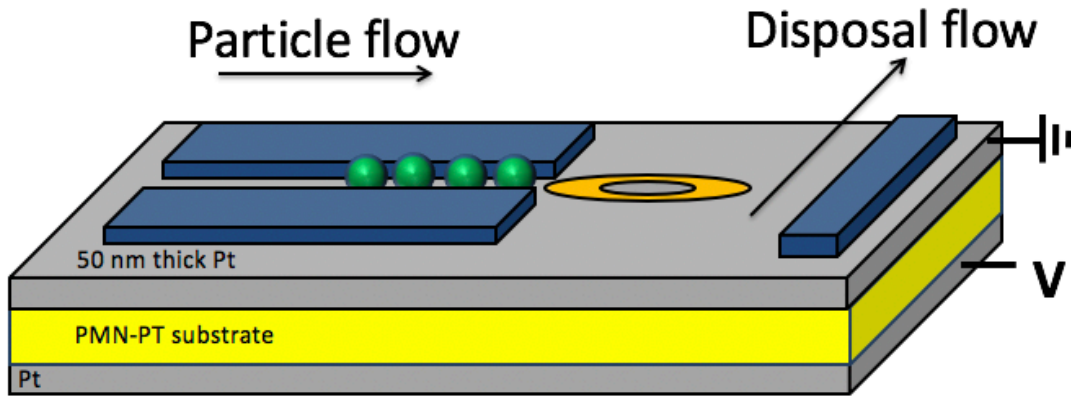
Chapter 5b: Theory of Multiferroic Actuator

Multiferroic heterostructures are composite nanostructures that exhibit coupling between one or more ferroelectric materials, or materials with a stable nonzero electrical polarization at no applied electric field, and ferromagnetic materials, or materials with a stable nonzero magnetic field at zero applied magnetic field. These materials can be coupled through a variety of mechanisms but particularly relevant to this work is coupling through the inverse magnetostrictive effect, also known as the Villari effect, which is the change in magnetization of a ferromagnet under applied stress. Because all ferroelectric materials are piezoelectric (undergo deformation under an applied electric field) due to the necessary asymmetry of a ferroelectric crystal, this stress can be generated locally by applying an electric field to a ferroelectric material which can transfer stress to a ferromagnetic material.

Local control of magnetic state in a micromagnetic structure with this method can be applied to the problem of capture and manipulation of magnetic microparticles in a fluid. Sohn and coauthors (Sohn *et al.* 2015) demonstrated that a stable domain structure which forms two opposing domain walls can be induced and programmatically rotated in a multiferroic system consisting of a magnetic nickel ring on a single crystal [011]-normal PMN-PT (lead magnesium niobate – lead titanate) substrate. By applying an electric field in the [011] direction, they induce an out-of-plane tensile strain in the PMN-PT, which causes transverse strains in-plane: a tensile strain along the [10-1] axis and a compressive strain along the [100] axis. Due to the negative magnetostriction of nickel, the magnetic domains reorient to align with the compressive strain direction, moving the domain wall to align with the [100] axis. Furthermore, they demonstrated that the external magnetic fields at the domain walls can locally trap superparamagnetic iron oxide microbeads, and that trapped beads can follow the rotation of

the domain wall under applied strain. In other words, an applied electric field can be used to control the position of a magnetic bead in a fluid at single-micron scale.

Chapter 5c: Design of Multiferroic-Microfluidic Gate



Microfluidic circuit design

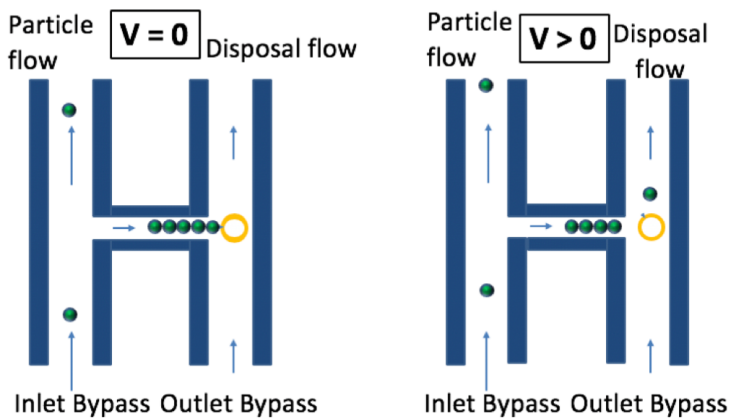


Figure 5-1: Schematics of particle valve operation.

A narrow channel between two flows at different operating pressures is obstructed by a multiferroic gate. Capture and release of particles at the gate modulates flow through the channel.

One potential application of this technology is flow control in microchannels by means of magnetic valves. By trapping the particle in the path of a channel that has a cross-sectional area comparable to the size of the particle, one could modulate the hydrodynamic resistance of the channel and in doing so divert fluid flow to parallel channels. This type of valve functions (in a low-Reynolds number flow) without completely obstructing the flow, but still requires the particle to be a large fraction of the size of the channel for maximum effectiveness. Examples of applications of such an actuator include the sorting of biological particles such as cells, or the creation of packed beds of functionalized magnetic nanoparticles for applications in molecular sensing.

See Figure 5-1 for a schematic of such a system. A magnetic microstructure, which can be controlled using piezostain in the manner described above, is located at one opening of a small (~4 μm wide by ~2 μm deep) channel which connects two large channels (labeled as the

“particle flow” and “disposal flow” in Figure 5-1). A magnetic particle is captured at the domain wall, partially blocking a channel and causing a buildup of additional particles behind it. Alternatively, additional magnetic traps within the channel could be used to modulate the number of trapped particles more precisely. When a voltage is applied to the piezoelectric substrate, the domain wall moves, and given a large enough particle and a fast enough domain wall motion the Stokes drag force will overcome the magnetic force, causing the ejection of the particle into the disposal flow (see Sohn *et al.*, supplementary material) (Sohn *et al.* 2015) and opening the channel.

At low Reynolds number, the flow through a microchannel of arbitrary shape is a linear function of the pressure drop across that channel. The constant of proportionality between the flow rate Q and the pressure drop ΔP is commonly given as the hydraulic resistance, which depends on the channel shape and dimensions (Damiri and Bardaweel 2015), as an analogue to Ohm’s law:

$$\Delta P = R_h Q$$

$$R_h = \frac{\mu L \beta}{A^2}$$

where μ is the dynamic viscosity, L is the length of the channel, A is the cross-sectional area, and β is a geometric factor; for instance, in a cylindrical channel $\beta = 8\pi$. At $Re \sim 0$ the Navier-Stokes equation simplifies to the Stokes creeping flow equation (Kirby 2010):

$$\nabla p = \eta \nabla^2 \vec{u}$$

where p is the pressure, η is the dynamic viscosity and \vec{u} is the velocity vector field. This equation is linear and time invariant, which means pressures and flow rates add linearly. As a result, hydraulic resistances behave mathematically like electrical resistances and can be analyzed as such, allowing for simple network analysis of microflows. Though the hydraulic resistance of a microchannel with a particular geometry may require experiment or simulation to determine, should the hydraulic resistance be known the channel can be abstracted as a lumped parameter and a network of such channels can be easily analyzed.

This microfluidic particle valve has a Reynolds number of approximately:

$$Re = \frac{\rho v L}{\mu} \sim \frac{(10^{-4} m s^{-1})(10^{-6} m)}{10^{-6} m^2 s^{-1}} = 10^{-4}$$

(where ρ is the density of the fluid, v and L are the characteristic velocity and length of the system, and μ is the dynamic viscosity), which is much less than 1, meaning that this flow can be safely approximated as a Stokes flow and making this network amenable to circuit analysis. By magnetically trapping a particle in the channel, the hydraulic resistance of that channel is increased, reducing the flow rate in that channel and increasing the flow rate in parallel

channels. See Figures 5-2 and 5-3 for results from COMSOL Multiphysics simulations of 4umx2um channels with various sizes and numbers of particles trapped within the channels:

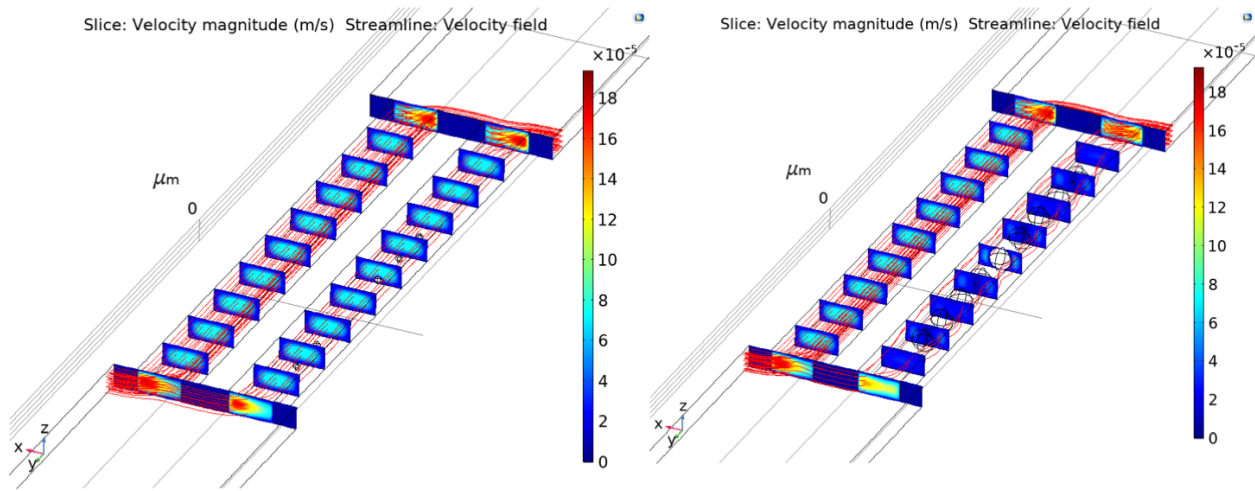


Figure 5-2: Simulations of particle valve, 9 trapped particles. Left: 0.6 μm particles. Right: 2 μm particles.

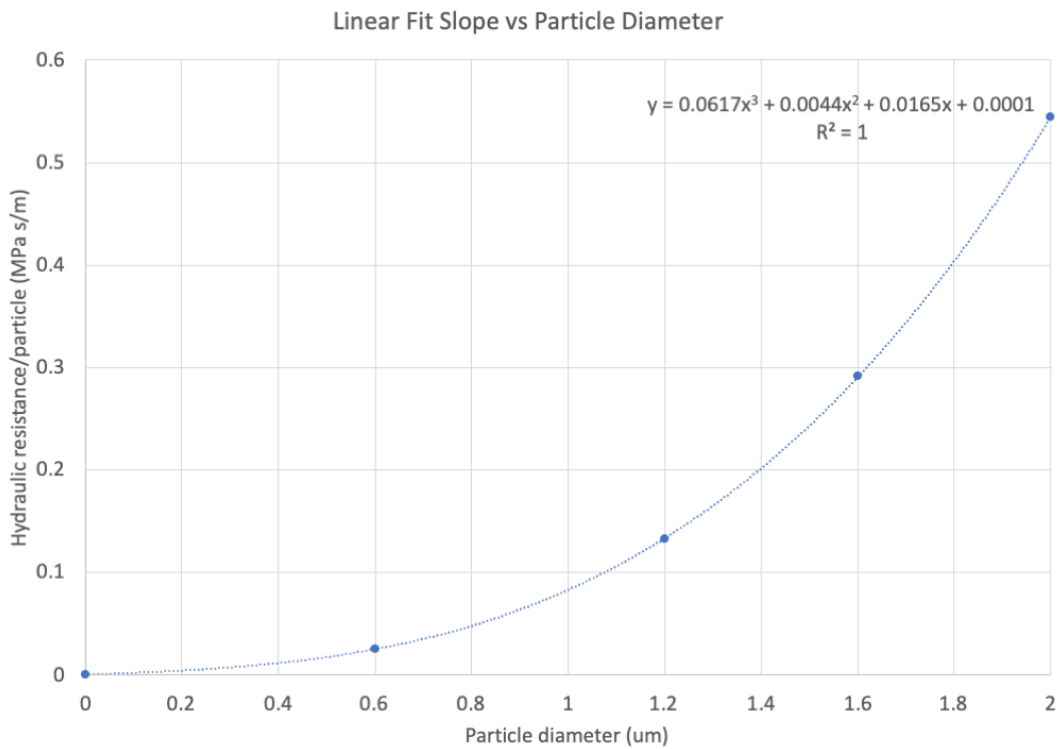
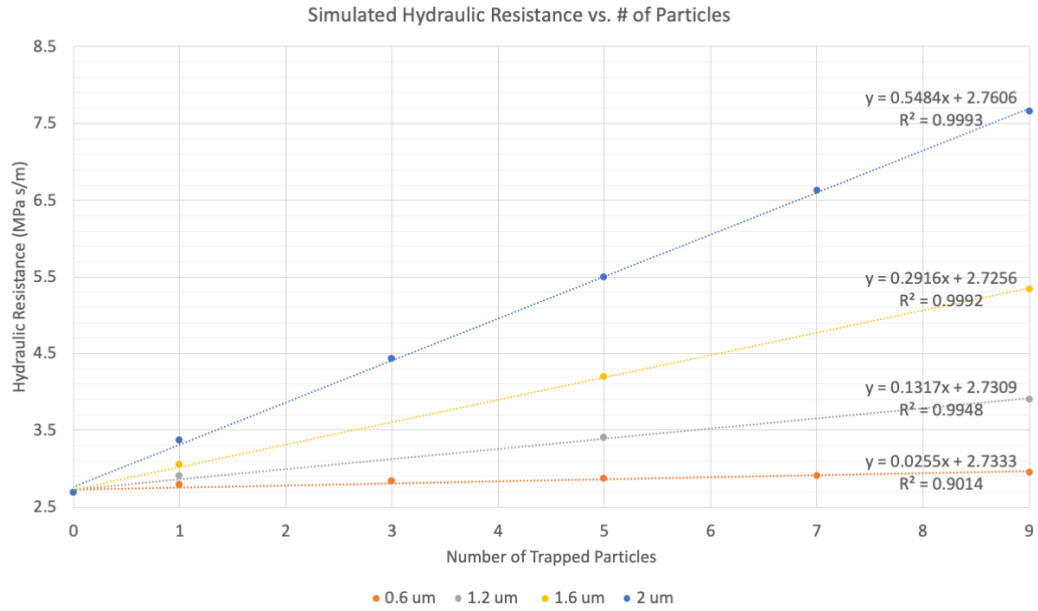


Figure 5-3: Particle gate simulation results. Top: Hydraulic resistance (pressure/flow rate) vs # of particles for 4 different particle diameters: 0.6, 1.2, 1.6, 2 um. As expected, the increase in hydraulic resistance is linear with the number of trapped particles. Bottom: Change in hydraulic resistance per particle as a function of particle diameter.

The increase in hydraulic resistance is linear with the number of particles trapped in the channel. The slope of this line (i.e. the increase in resistance per particle) depends on the particle size in a way that can be fit very accurately using a third order polynomial. Due to the linearity of the Stokes equations, if the particle size is normalized by the channel depth, these results are generalizable to channels and particles of other sizes so long as the channel aspect ratio is 1:2 and the governing assumptions (Stokes flow, non-slip, continuum assumption) hold. For differently shaped channels, the dependence on particle diameter is expected to vary but the hydraulic resistance is expected to remain linear with the number of particles, so generating scaling laws for these geometries would be computationally simple.

These results demonstrate the operating principle of the microparticle valve. A trapped particle does not completely block the flow, meaning that additional particles can flow into the channel and build up behind the trapped pilot particle. However, each particle trapped in the channel increases the hydraulic resistance; a 3-fold increase in hydraulic resistance (9 $2\mu\text{m}$ particles trapped in this channel geometry) results in a 3-fold decrease in the flow rate in that channel at constant pressure. Due to this increase in hydraulic resistance, as a channel fills up with particles, other particles will be diverted to parallel channels, resulting in a relatively even packing of each channel with particles. In addition to its flow control applications, this behavior could be taken advantage of in order to generate uniform particle beds for molecular sensing.

Chapter 5d: Characterization of Particle Trap and Release Mechanism

In order to characterize the dynamics of microparticle trap and release independent of the microfluidic channel, $1\mu\text{m}$ diameter superparamagnetic iron oxide microbeads were suspended in deionized water above a multiferroic heterostructure consisting of magnetized nickel microrings on a platinum-PMN-PT-platinum stack as described above. The motion of the beads was monitored using a high-speed camera (Fastec IL-3, 1000 frames per second) until trapping of beads at the domain walls was observed. Trapping events were recognized by a sudden cessation of the Brownian motion of the microbeads as they encountered the stray field at the domain wall (see Figure 5-4). After trapping was observed, a potential was applied in steps of 20V from 0 to 400V and motion of the beads was noted as the domain walls rotated.

While the domain wall rotation behaved as expected when observed, the motion occurred in a relatively small number of trapping sites. One possible reason for this low yield is the result described by Lo Conte *et al.* (Lo Conte *et al.* 2018) in this particular multiferroic system: even in single-crystal PMN-PT, there exists a notable local variation in strains as measured by X-ray microdiffraction. Because the applied field and the domain wall motion are coupled through strain in the piezoelectric material, this corresponds to a variation in activation voltage between actuators.

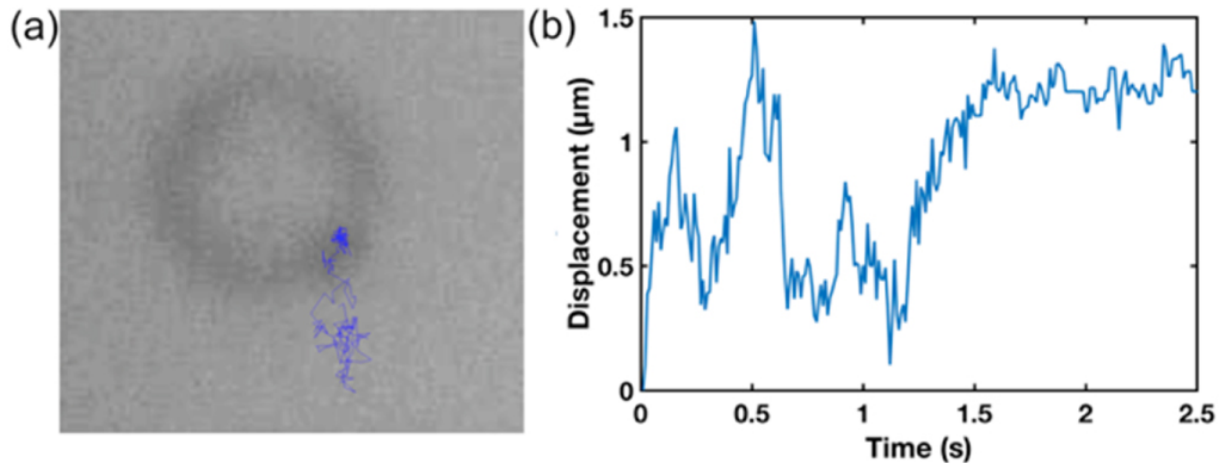


Figure 5-4: Cessation of Brownian motion on suspended particle capture. a) Motion of particle center-of-mass tracked in ImageJ. b) Displacement of particle from starting location. Particle capture at domain wall occurs at 1.5s.

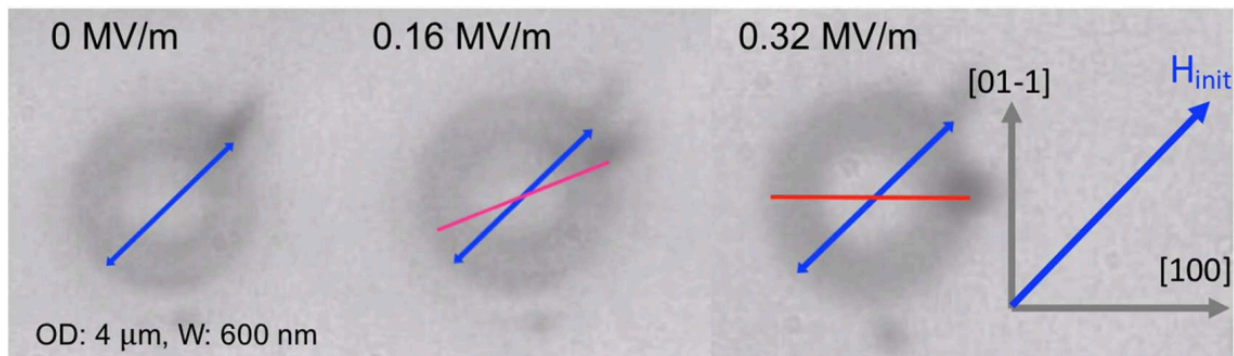


Figure 5-5: Particle rotation under electric field. Particle is initially trapped at domain wall corresponding with direction of magnetization. With gradually increasing electric field, particle reorients to align with compressive strain axis [100].

Visualization of particles under flow was challenging due to the need for an opaque substrate. Bulk flow experiments were performed using a flow cell constructed from microscope slides with drilled vias and double-sided spacer tape (ARcare 90106). This allowed for the inlets and outlets to be positioned far away from the microscope objective so as not to interfere with imaging, even at small focal distances. We conducted bulk flow tests of capture by two classes of magnetic microstructures: nickel rings of the same type described above, and 6 μm diameter Terfenol-D ($\text{Tb}_x\text{Dy}_{1-x}\text{Fe}_2$) microdiscs. Terfenol-D is a magnetic composite which is attractive to multiferroics researchers for its very high magnetostriction (M. Liu *et al.* 2012) leading to strong magnetoelectric coupling; however, fabrication constraints prevented us from exploring this material system further. Capture of 1 μm beads was observed even at relatively high (mm/sec) fluid velocities.

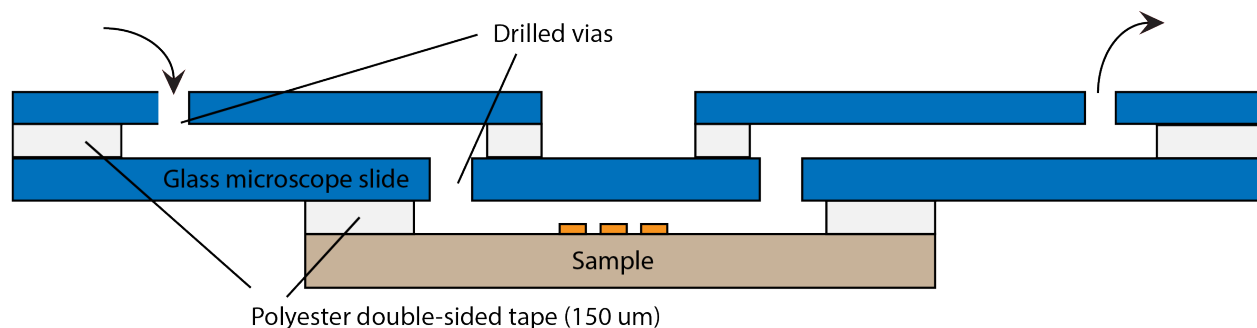


Figure 5-6: Experimental setup for bulk flow tests. Gaskets are laser cut from Adhesives Research ARcare 90106 double-sided diagnostic grade spacer tape. 2 mm diameter vias drilled in glass microscope slides using a carbide drill bit.

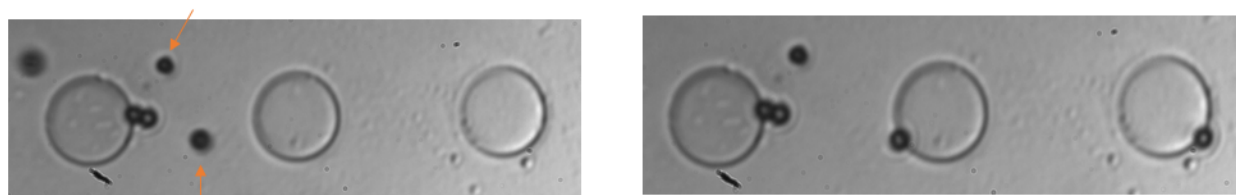


Figure 5-7: Particle capture on Terfenol-D disks. Capture of particles from bulk flow at the edges of Terfenol-D ($Tb_xDy_{1-x}Fe_2$) microdiscs 6 μm in diameter.

Chapter 5d: Patterned Microelectrodes for Local Strain Control

As noted by Lo Conte *et al.* (Lo Conte *et al.* 2018), local variation of strain across the substrate may be one reason for inconsistent particle capture and motion. Local control of strain is necessary to address this problem. Additionally, local control of strain is necessary for addressability of individual magnetic particle traps. Sohn *et al.* previously achieved local control of strain in nickel discs on a PZT substrate using an array of control electrodes (Sohn *et al.* 2017) by inducing in-plane strain between alternating pairs; however, this requires 6 electrodes per site, making it difficult to scale. To attempt to control local strain in bulk crystalline PMN-PT, we used patterned surface electrodes in an effort to localize the out-of-plane ([011]) strain, relying on the induced strain in the [100] and [01-1] directions to drive domain wall reorientation. This is the same approach previously used to actuate nickel rings on PMN-PT in bulk using unpatterned parallel-plate electrodes.

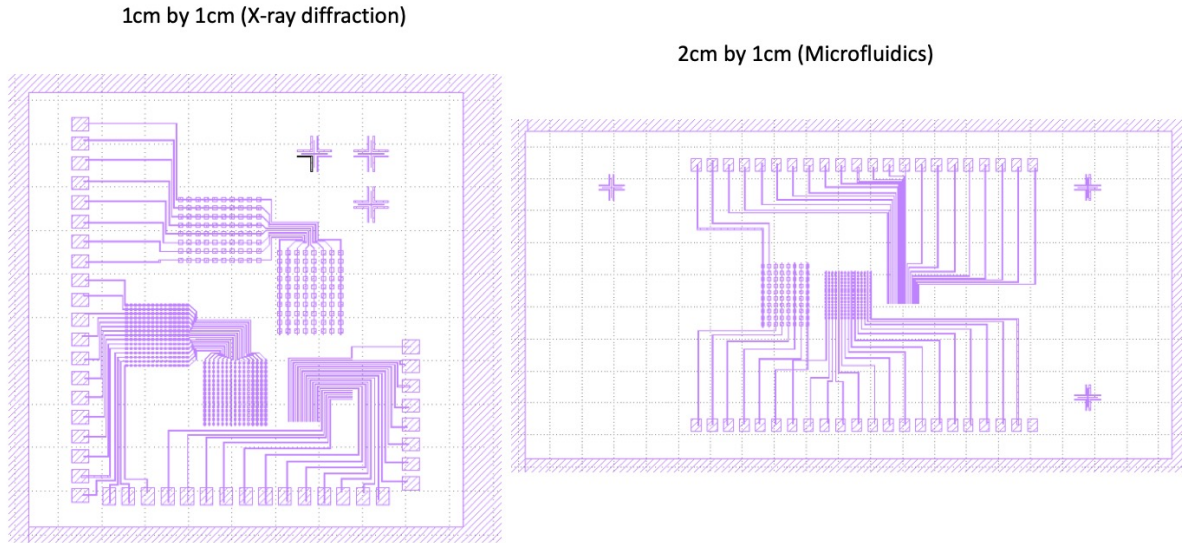


Figure 5-8: PMN-PT surface microelectrode designs.

We designed two different layouts according to the sizes of PMN-PT substrate we had available: a 2cm by 1cm chip for testing flow (see Chapter 5g for details of the microfluidic interfacing) and a 1cm by 1cm chip for X-ray microdiffraction experiments. See Figure 5-8 for layout images. Three different electrode size/pitch combinations were selected: 100 μm electrodes with 100 μm spacing, 50 μm electrodes with 50 μm spacing, and 10 μm electrodes with 50 μm spacing.

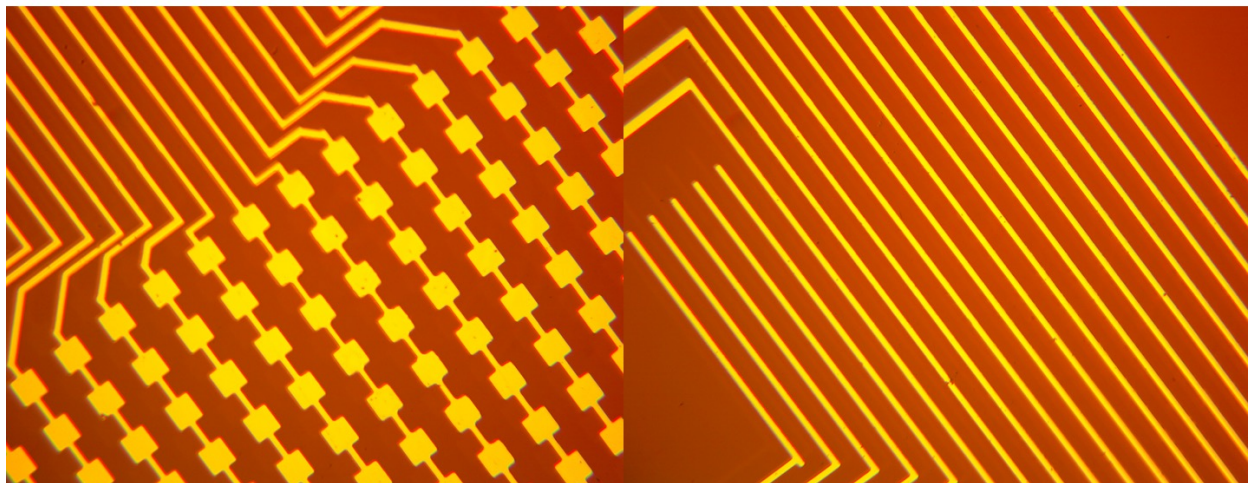


Figure 5-9: Surface microelectrodes on PMN-PT. Left: 50 μm . Right: 10 μm

Chapter 5e: Fabrication

Platinum microelectrodes were patterned on 2cm by 1cm <011>-cut PMN-PT substrates by contact photolithography and lift-off. We used a 2-layer photolithography process developed in the Marvell Nanofabrication Laboratory for liftoff using thin photoresists. First, a layer of MicroChem LOR-5A was spin-coated and soft baked; this is a specially-designed liftoff resist that develops in most i-line or g-line photoresist developers and is masked by a layer of photoresist above it. Essentially, it acts as a spacer between the substrate and the photoresist layer, increasing the total thickness of the resist while allowing for the use of high-resolution positive photoresists that cannot form thick layers by themselves. Then, a second layer of Fujifilm OiR 906-12 resist was added and was exposed on a Karl Suss UV contact mask aligner with a dose of 130 mJ/cm² with a post-exposure bake of 120 degrees C for 60 seconds, and developed in MF-26A developer for 60 seconds. 50 nm of platinum was then deposited using a 10kW e-beam evaporator to form the electrode layer and lifted off in an ultrasonic bath using MicroChem Remover PG.

For the microfluidic chip, e-beam lithography was used to define 6µm and 4µm diameter rings. Nickel was deposited by a collaborator (Dr. Mohanchandra Kotekar Panduranga, UCLA) and lifted off to form magnetic microstructures (see Figure 5-10).

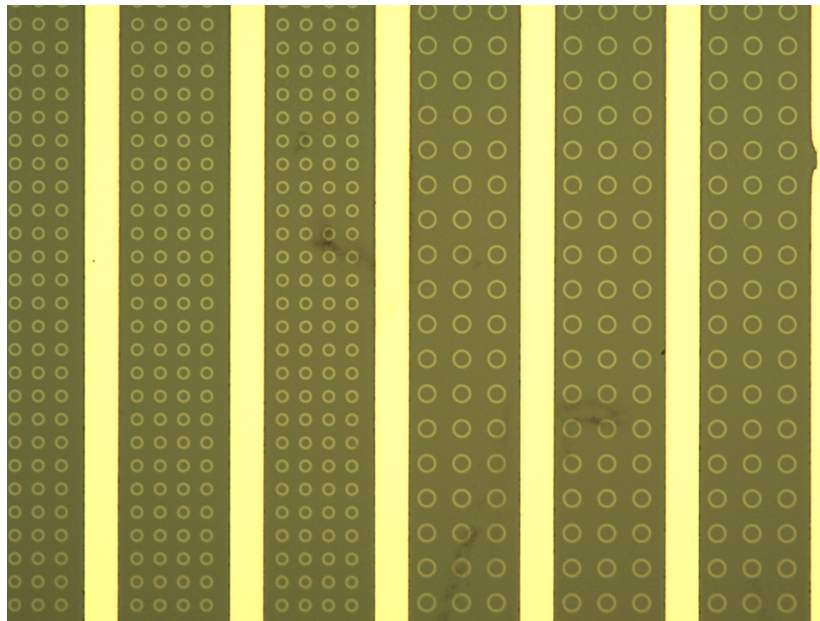


Figure 5-10: Micromagnet patterns. 6µm (right) and 4µm (left) diameter rings patterned on PMN-PT substrate between 10µm microelectrodes.

Chapter 5f: Strain Measurements

To control local strain in the substrate, a method of measuring microscale strain was needed. To this end we conducted X-ray microdiffraction experiments at Beamline 12.3.2 of the Advanced Light Source. This beamline is able to focus a beam of X-rays from the ALS synchrotron down to a spot size of less than 1 μm . The X-ray beam is scanned over the substrate by a system of mirrors and the pixel-by-pixel diffraction pattern is collected by a CCD detector (N. Tamura *et al.* 2009). The system also includes an X-ray fluorescence detector which is used to read the emission spectra of various chemical species on the surface of the sample. By tuning the detector to the emission peaks of microstructured materials one can locate specific features (e.g. platinum microelectrodes, nickel micromagnets) in order to orient the X-ray microdiffraction scan.

The substrate was attached to a 1cm by 1cm chip carrier with silver epoxy and the surface electrodes were wire-bonded to bond pads on the chip carrier (Westbond model 7400B, Al-1% Si wire). Adjacent pairs of electrodes were alternately wire bonded to ground or left floating, in order to include a control for surface strain induced by the platinum deposition. The platinum sheet electrode on the bottom of the chip, connected to the chip carrier by silver epoxy, was used as the hot electrode. The chip carrier fit into a socket on a custom PCB, which was bolted onto a magnetic sample holder designed for use with the Beamline 12.3.2 stage and connected to a DC power supply located outside of the X-ray safety hutch by a coaxial cable. We acquired microdiffraction patterns of the substrate at 6 different locations at voltages ranging from 0-400 V in increments of 100 V, with 10 μm pixel size. The locations correspond to electrode size and orientation: areas A1 and A2 correspond to the 50 μm electrodes, B1 and B2 the 100 μm electrodes, and C1 and C2 the 10 μm electrodes. An additional measurement, labeled area D, was performed on the 10 μm electrodes using higher resolution (2 x 2 μm pixels).

Diffraction patterns were automatically analyzed in XMAS (“X-ray microdiffraction analysis software”) (Tamura 2014) with the help of the beamline scientist and author of the software package, Dr. Nobumichi Tamura. I then plotted the xx, yy, and zz strain data using a custom Matlab script (see Appendix 1). Minimal data processing was used to correct for detector errors: duplicate data points, caused by the beam power falling out of tolerance and the measurement restarting, were removed, and dead pixels were replaced by an average pixel value. Dead pixel removal affected less than 10 pixels per image out of at least 1600. See Figure 5-12 for strain images and Appendix A for the MATLAB script used to plot these images.

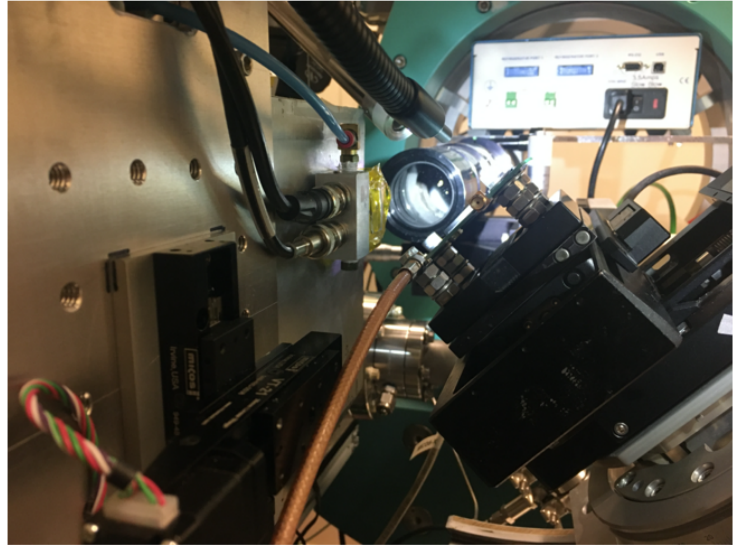
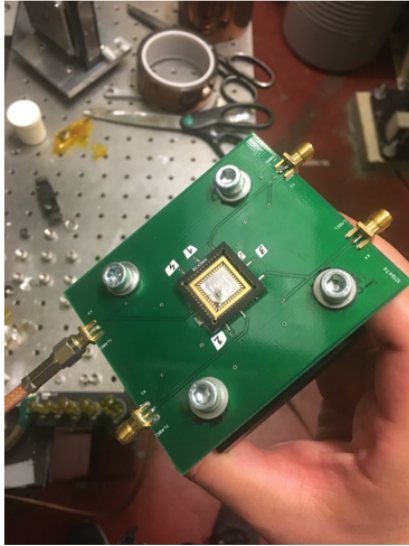


Figure 5-11: X-ray microdiffraction experimental setup at Beamline 12.3.2 of the Advanced Light Source. Left: PMN-PT sample mounted on custom PCB. Right: PCB mounted to motorized stage at 45 degree angle to x-ray beamline and detector (above image, out of frame).

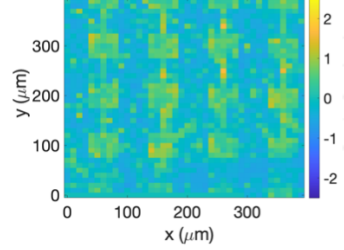
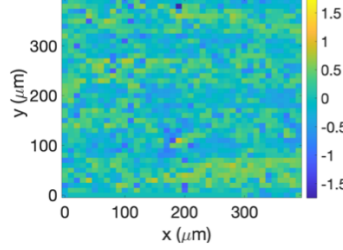
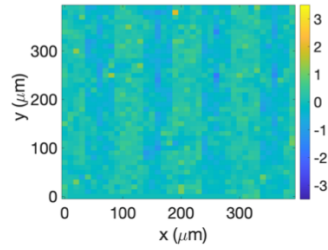
Area A1

XX strain (ppt)

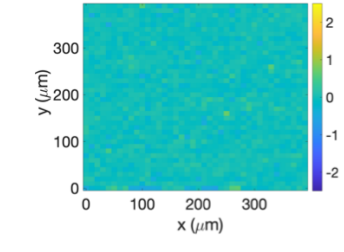
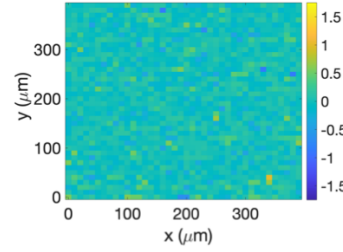
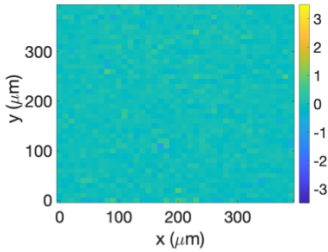
YY strain (ppt)

ZZ strain (ppt)

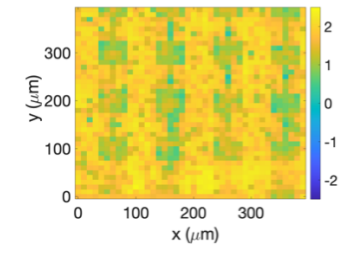
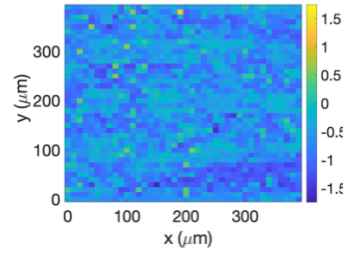
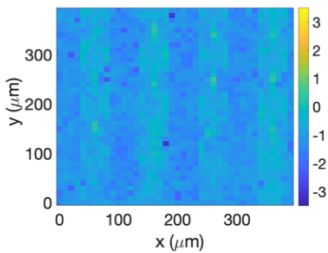
0V



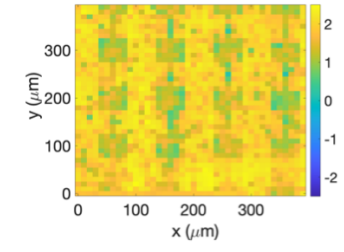
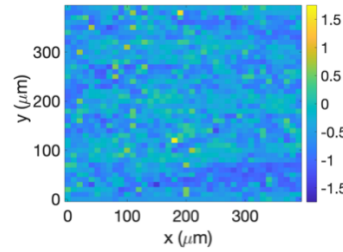
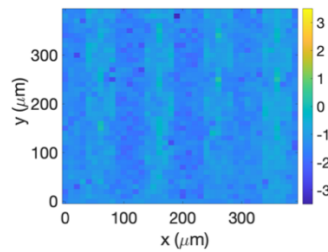
100V



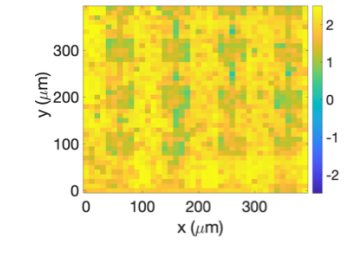
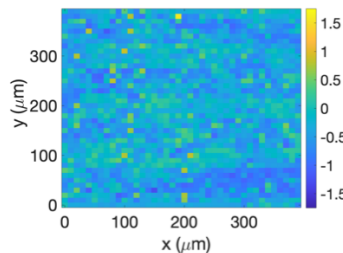
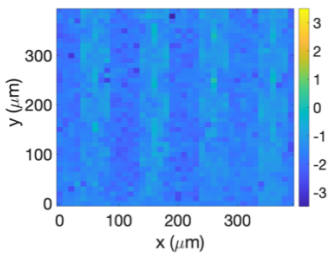
200V



300V



400V



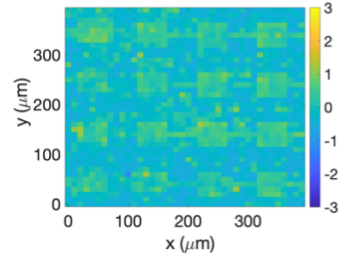
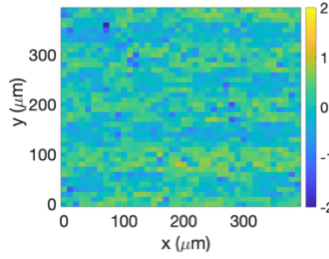
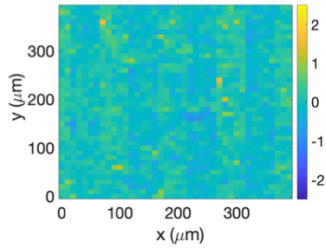
Area A2

XX strain (ppt)

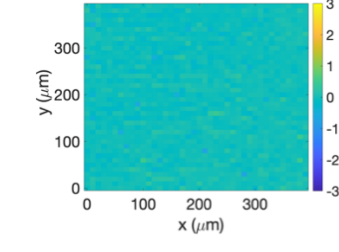
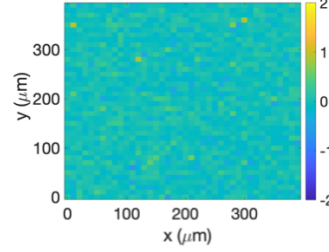
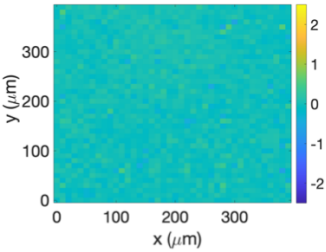
YY strain (ppt)

ZZ strain (ppt)

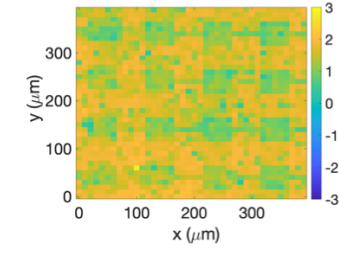
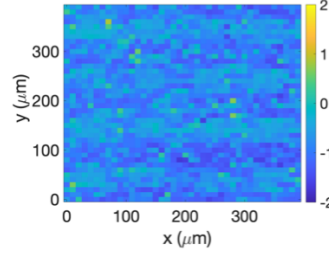
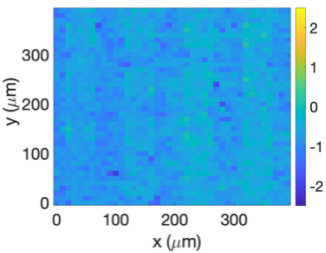
0V



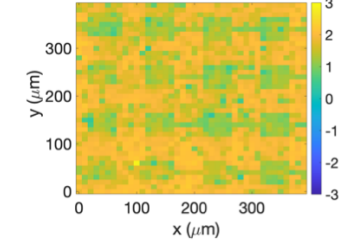
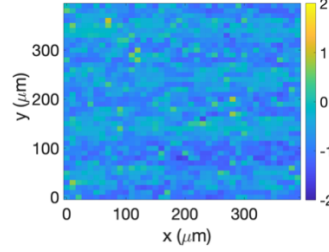
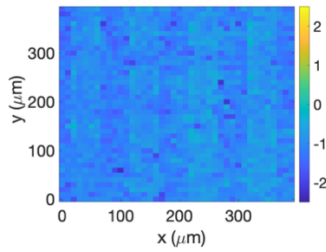
100V



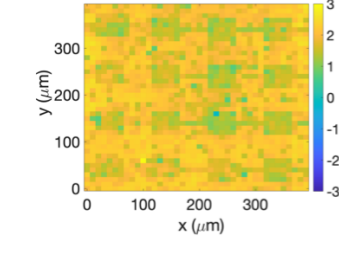
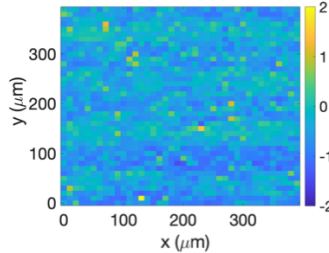
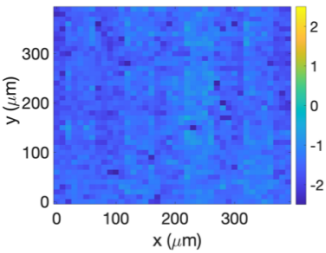
200V



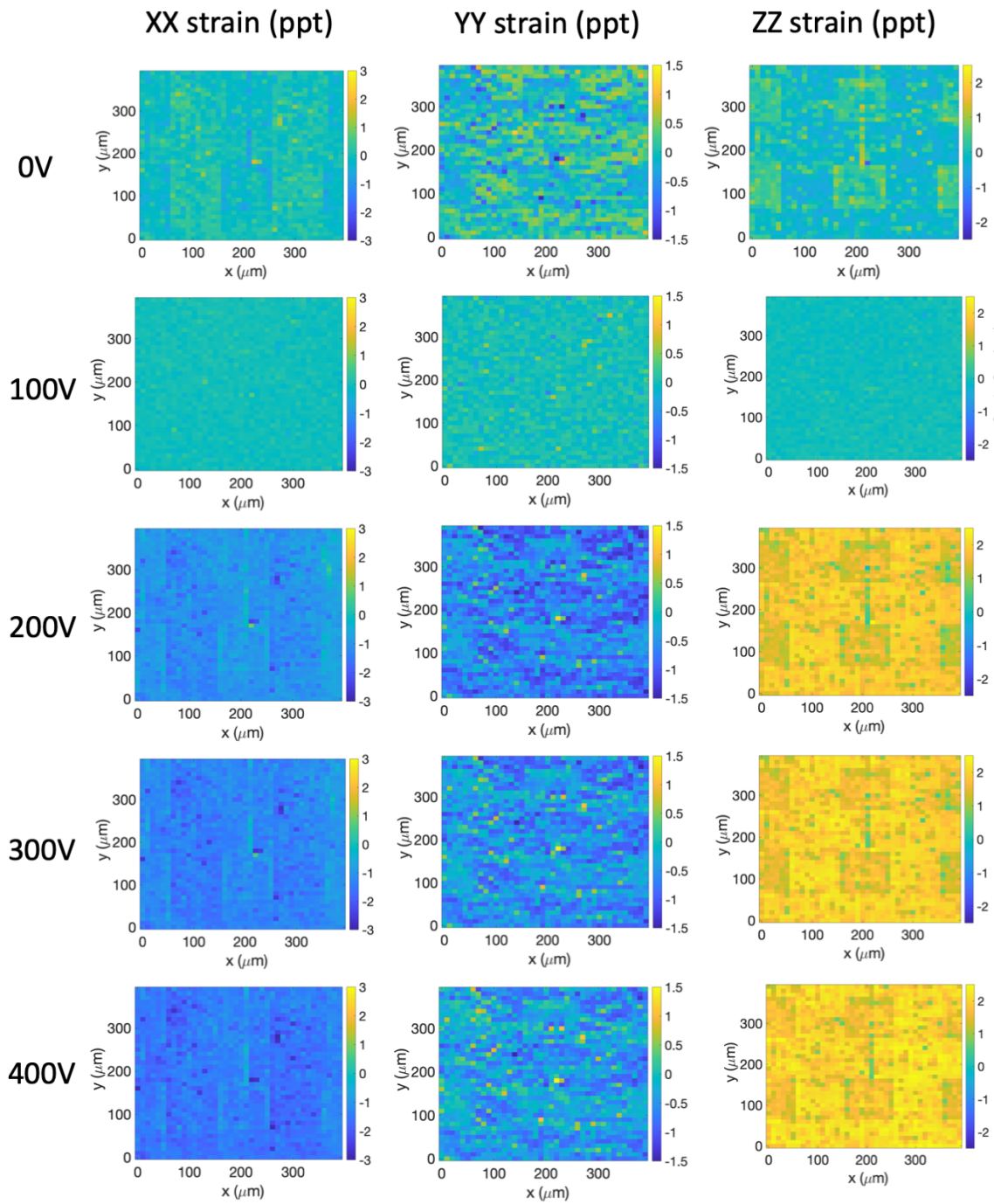
300V



400V



Area B1



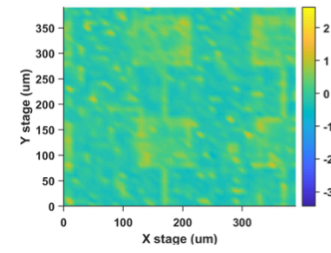
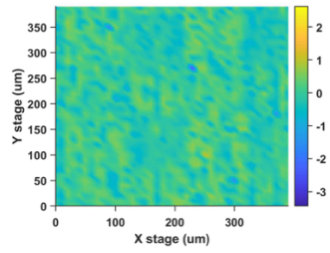
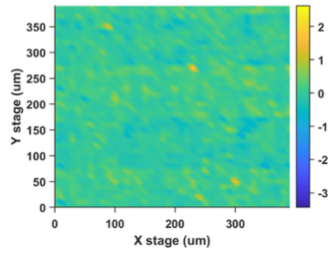
Area B2

XX strain (ppt)

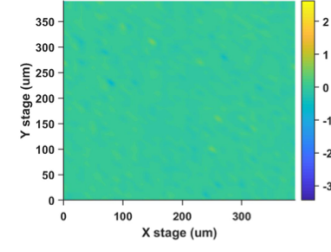
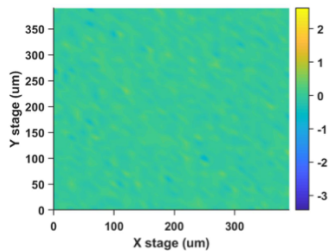
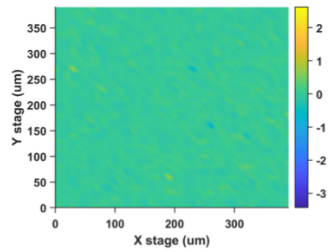
YY strain (ppt)

ZZ strain (ppt)

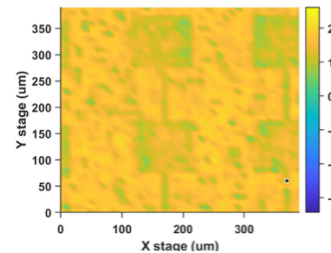
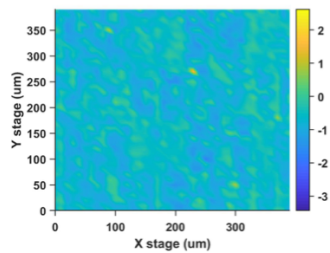
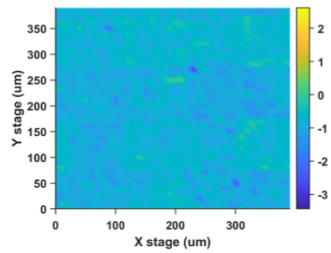
0V



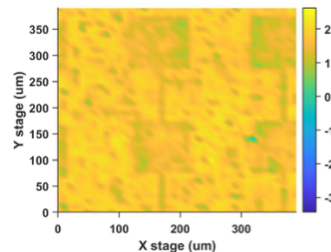
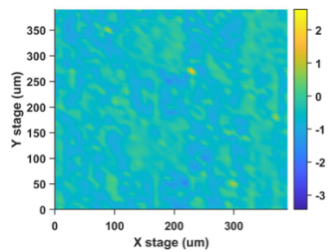
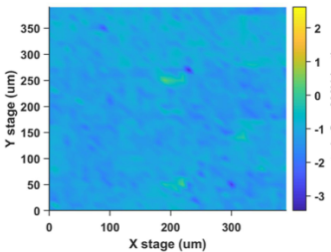
100V



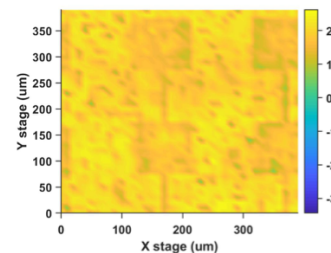
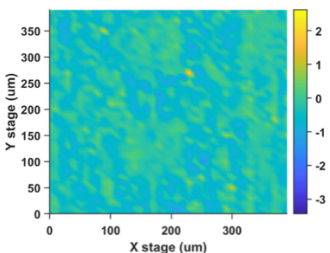
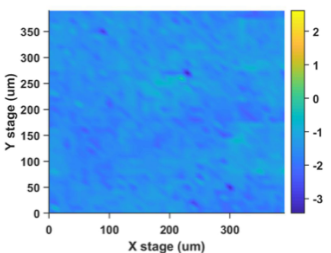
200V



300V



400V



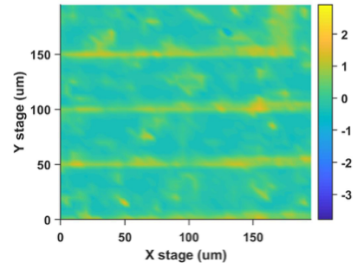
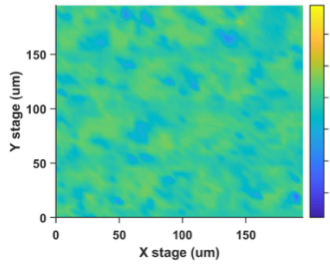
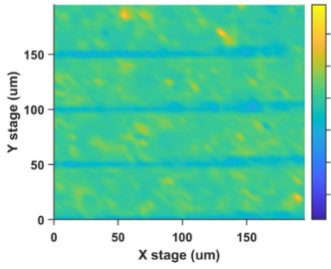
Area C2

XX strain (ppt)

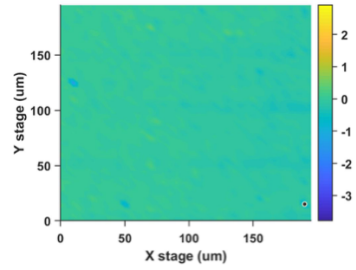
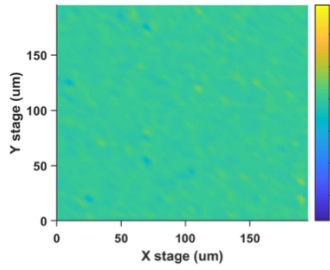
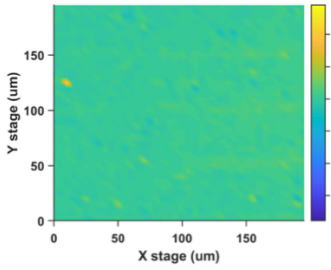
YY strain (ppt)

ZZ strain (ppt)

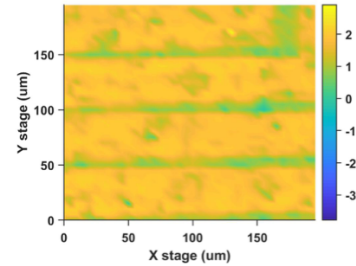
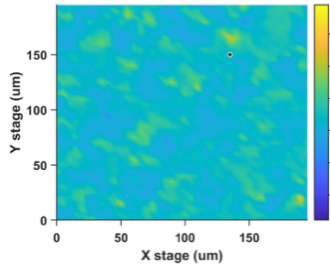
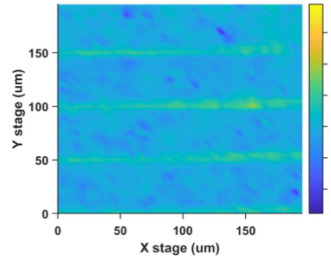
0V



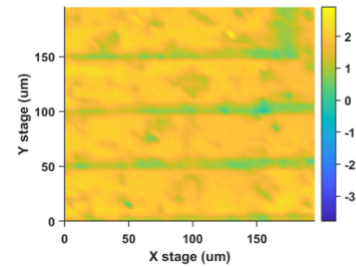
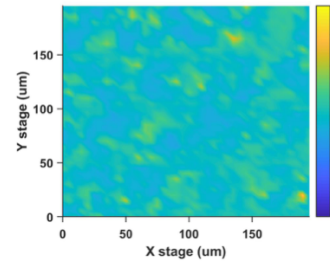
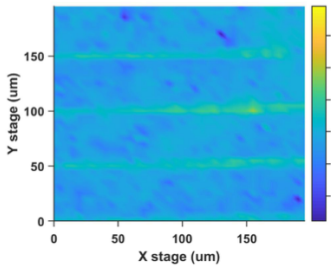
100V



200V



300V



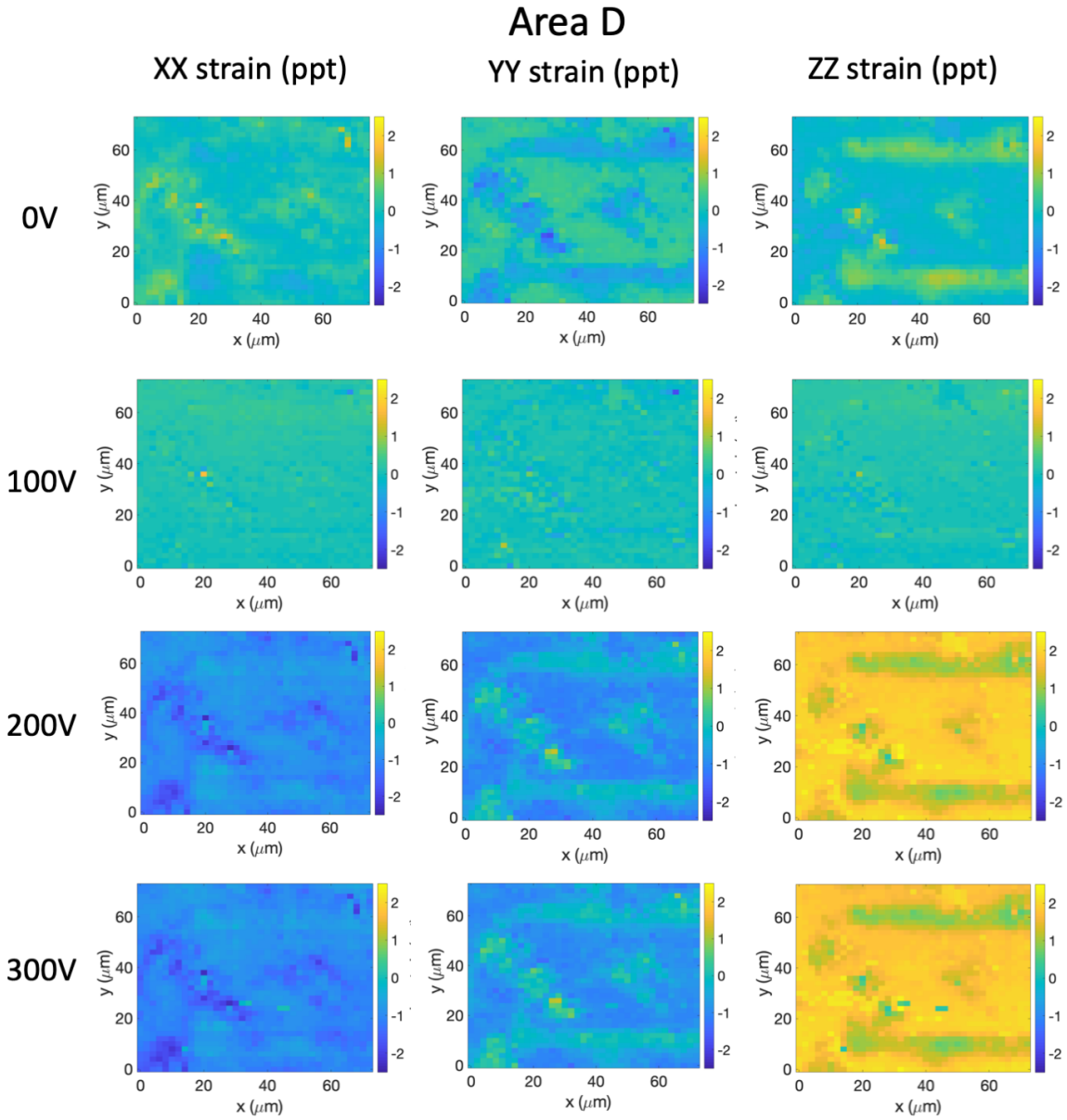


Figure 5-12: Strain maps from first strain measurement experiment. 0V images are absolute strain, all others are relative to 0V.

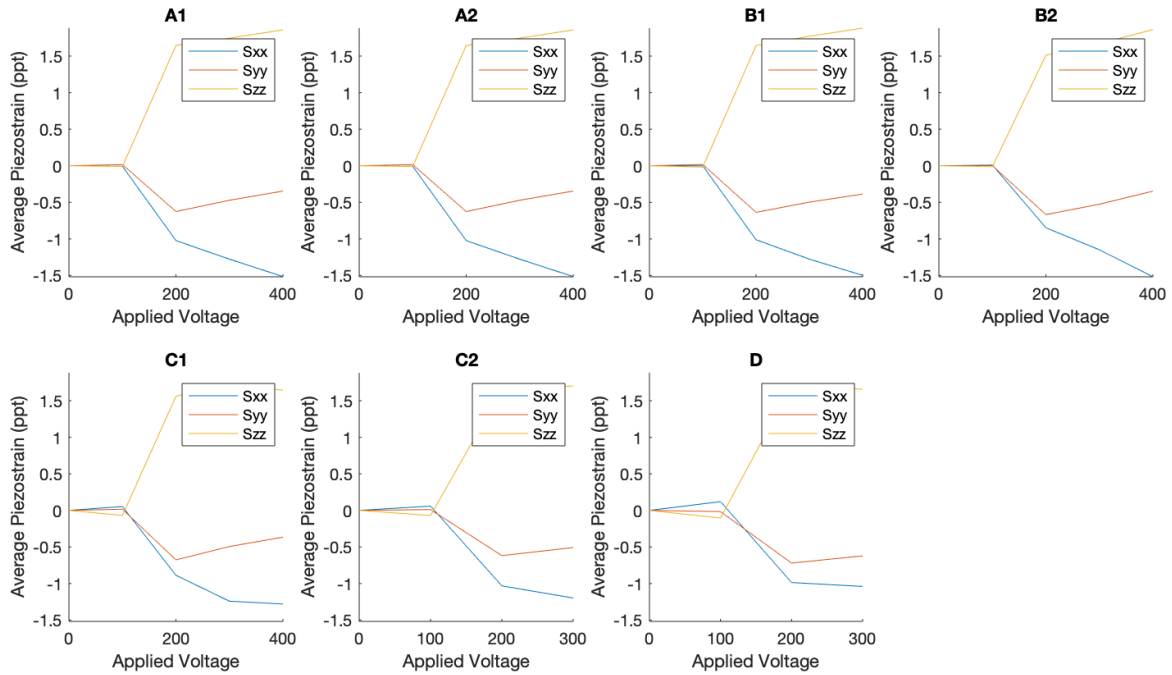
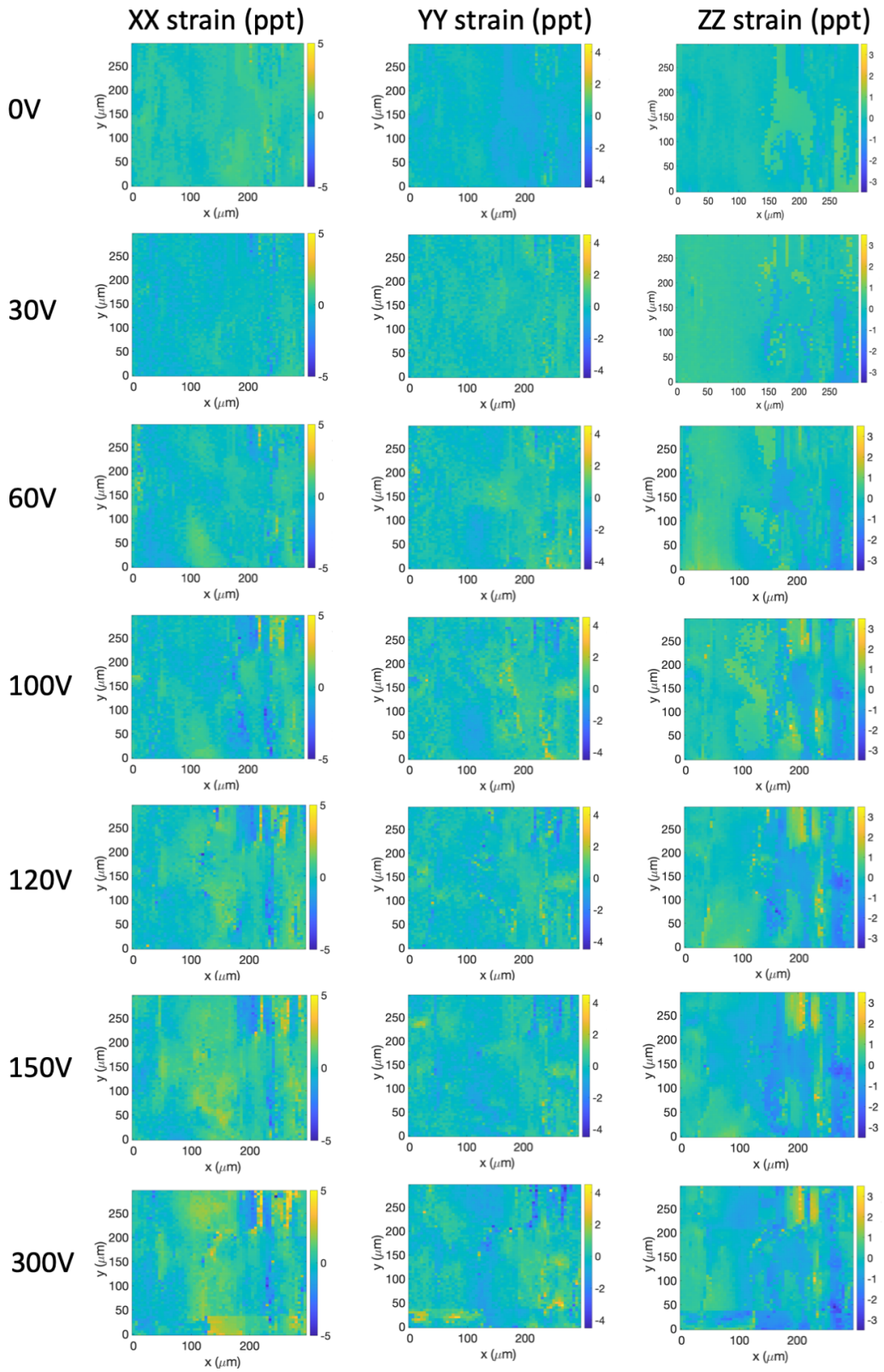


Figure 5-13: Average piezostrain from second strain measurement experiment.

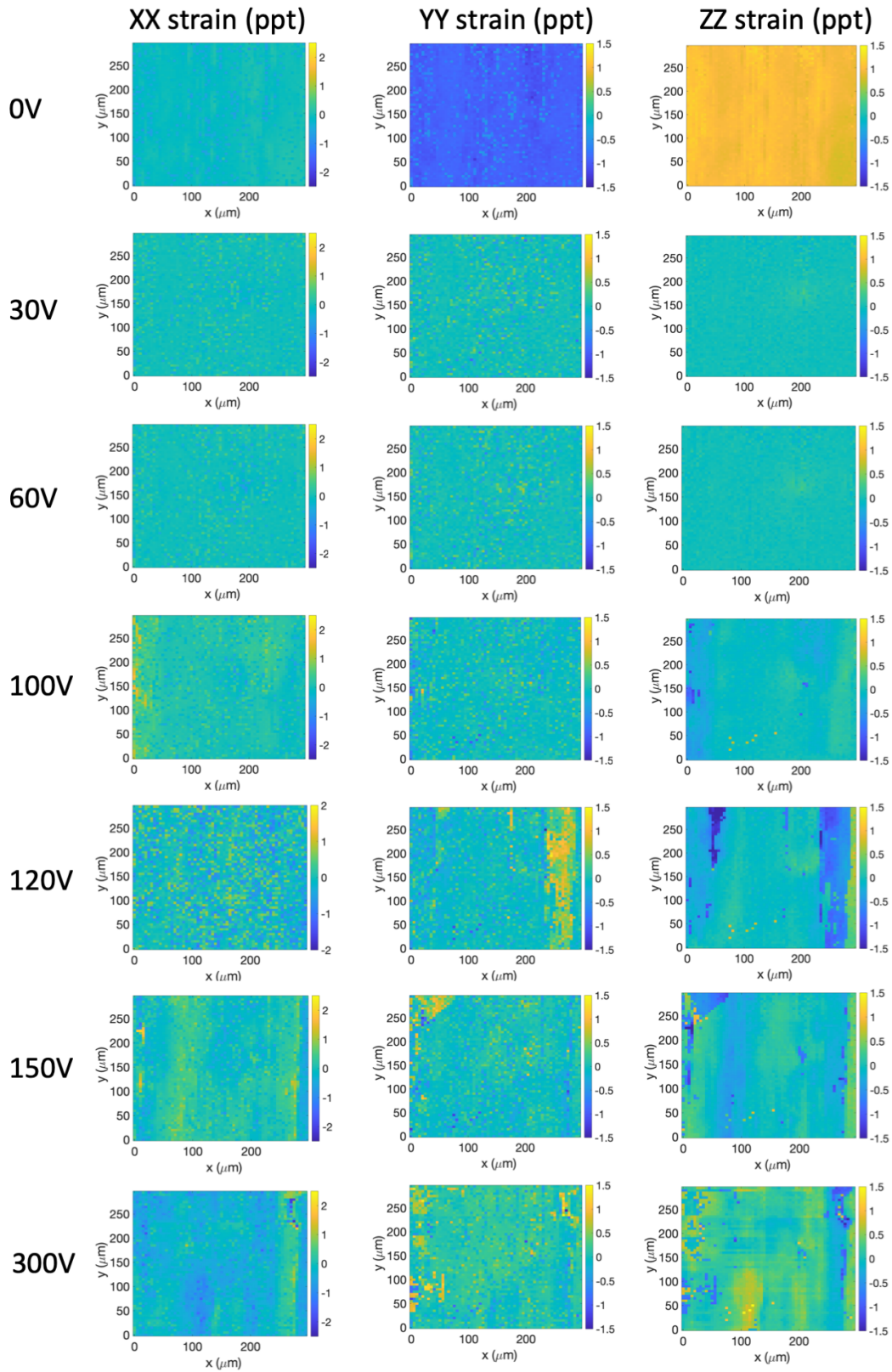
Local strain variations that map to the electrodes are clearly visible in these images. However, this maps directly to the residual strains present in the 0V measurements, in which no piezostrain is applied. Furthermore, the local strain patterns are present whether or not the electrode is hot or neutral. Instead, it appears that the result of the applied voltage is a bulk strain with some local variation due to residual strains from the metal deposition.

A follow-up experiment was designed to address some of the shortcomings of this initial experiment using the same PMN-PT sample. Instead of floating electrodes, we alternated hot electrodes with grounded electrodes. This is intended to contain the electric fields from the hot electrodes and prevent surface charging and to introduce local in-plane electric fields that may produce local strain patterns. The PMN-PT sample had been cycled once during the previous experiment and therefore some of the residual strain would have been annealed out. Furthermore, one measurement was done in a control area of the chip with no surface electrodes in order to measure the propagation of bulk strain over long distances. The results of this follow-up experiment are shown below.

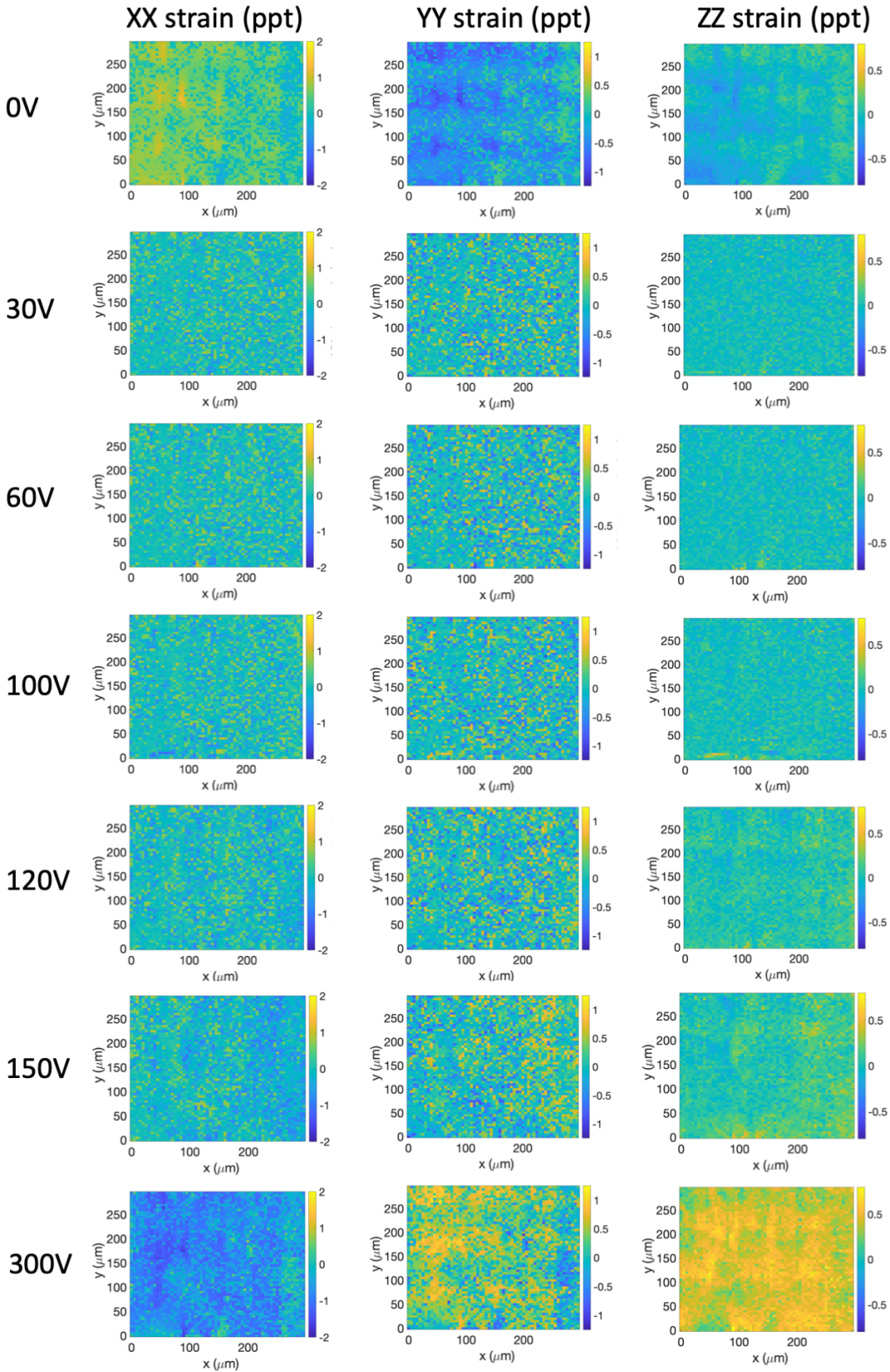
Area A1



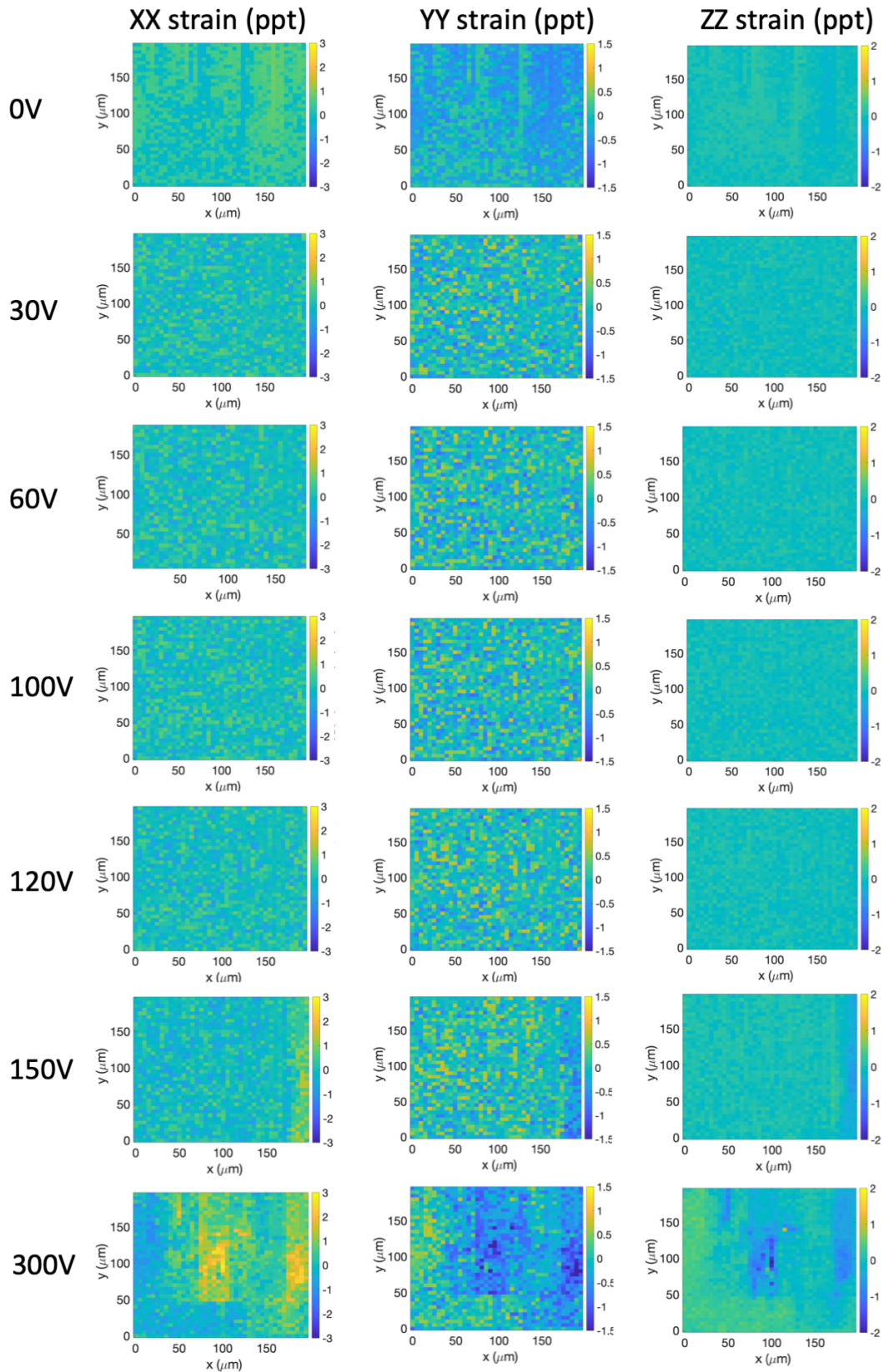
Area B1



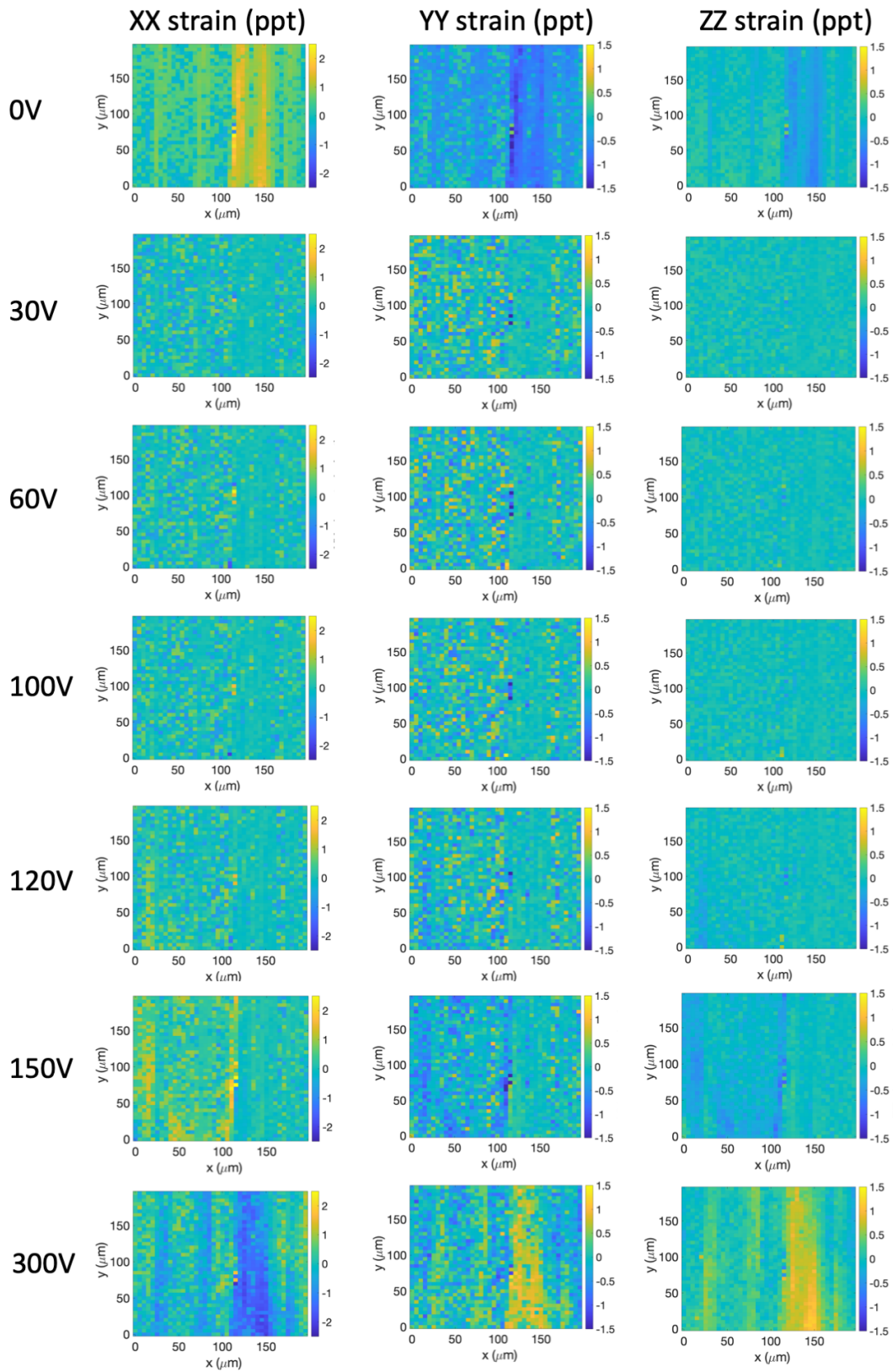
Area B2



Area C1



Area C2



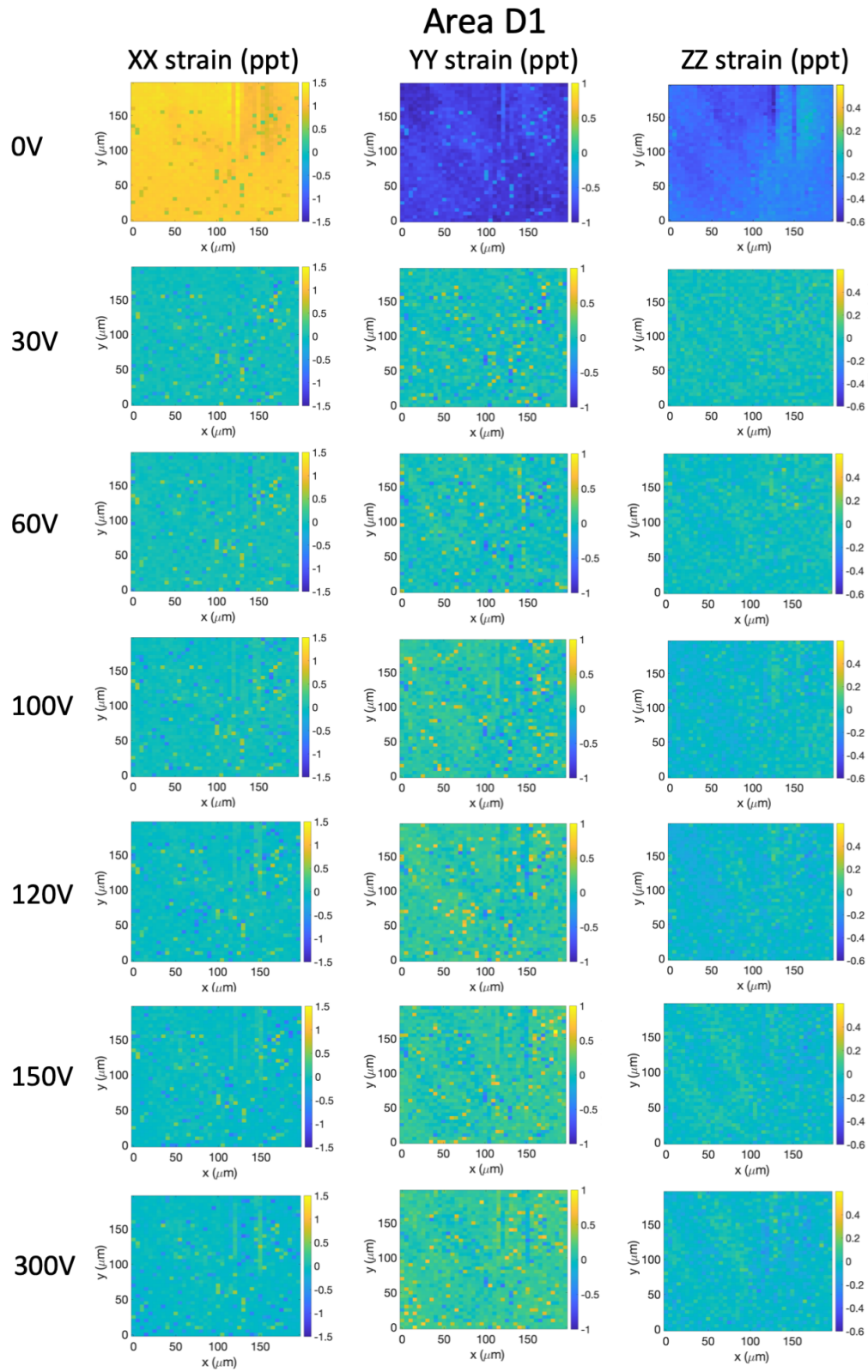


Figure 5-14: Strain maps from second strain measurement experiment. 0V is absolute strain, all others are relative to 0V

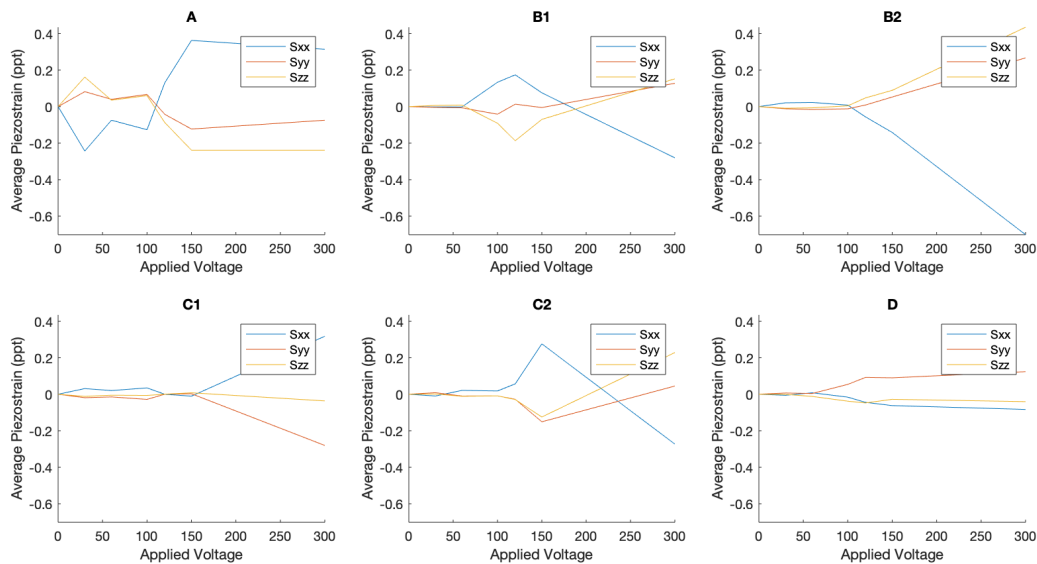


Figure 5-15: Average piezostain from second strain measurement experiment.

Several key differences from the strain patterns measured in Experiment 1 are immediately apparent. The residual strains that follow the electrode pattern are no longer present. This is to be expected after the initial cycling of the material. Substantial local variations in strain are present but do not appear to be related to electrode geometry. Average strains are substantially (~3 to 4-fold) lower than those in the previous experiment and some locations exhibit average strain trends in opposite directions; this does not appear to be an effect of local electrode orientations, as exhibited by areas B1 and B2 having identical electrode size but perpendicular electrode orientation and nevertheless exhibiting similar strain patterns at 300V. Furthermore, area D, which is located in a region of the chip where there are no surface electrodes, exhibits lower but non-negligible strain in all three directions. This could suggest that out-of-plane bulk strain is largely suppressed by the grounded surface electrodes, while in-plane variations in strain due to the in-plane components of the electric field produce local variations that are difficult to predict due to strain propagating over large distances.

Further work is necessary to fully understand the dynamics of designs which rely on surface electrode-driven control of out-of-plane strain in bulk crystalline PMN-PT. However, the results of these experiments suggest that local control of strain in this manner may be prohibitively difficult. Alternate strategies are needed based on in-plane strain or thin piezoelectric films.

Chapter 5g: Microfluidic Device Assembly

Interfacing a substrate like PMN-PT with a microfluidic device represents unique challenges. It is opaque, expensive (necessitating small chip size), rigid, and undergoes substantial (~1 part per thousand) strain during operation. Imaging the flow of 1 μm non-

fluorescent particles in a fluid with reflection microscopy requires a microfluidic chip material with good optical properties. My initial approach to this problem was to encapsulate the device in polycarbonate, which offers exceptional optical clarity. The 4 μ m feature size of the channels in this design was below the limit of the nickel electroplated molds described in Chapter 2; therefore, I etched silicon embossing molds using a deep reactive ion etch (Bosch SF6/C4F8 etch, described in more detail in Chapter 2). The molds were treated with a self-assembled monolayer of n-octadecyltrichlorosilane by immersion in anhydrous toluene for 60 minutes in order to reduce the demolding force (Saha *et al.* 2011). These molds were delicate and prone to shattering if embossing pressure was ramped too quickly; however, they produced exceptional results even with very high aspect ratio channels (see Figure 5-16 for an image of a 4 μ m wide by 12 μ m deep polycarbonate channel).

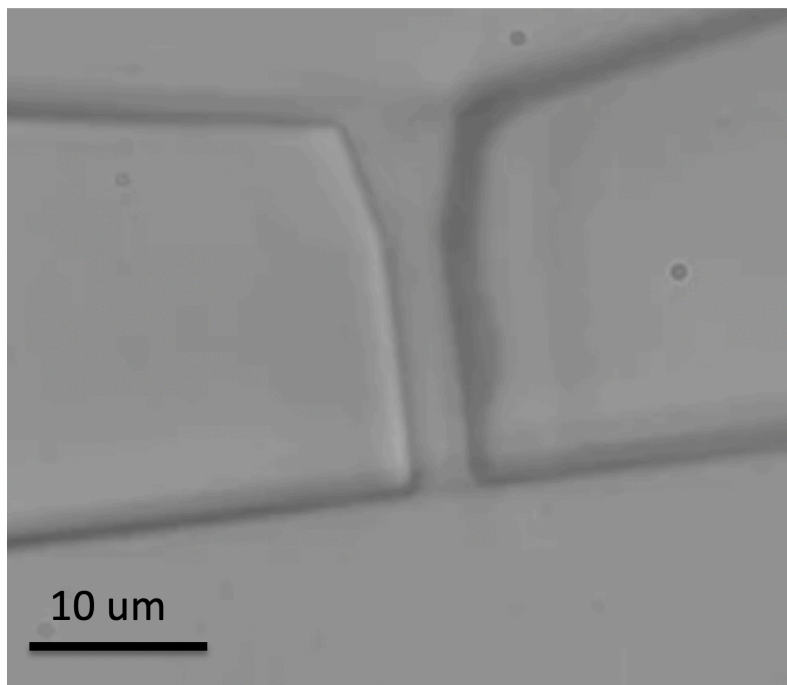


Figure 5-16: 4 μ m by 12 μ m (3:1) aspect ratio in polycarbonate. Sealed by thermal bonding and filled with deionized water.

Unfortunately, polycarbonate is too rigid to form a seal with PMN-PT, so it was necessary to use PDMS (poly-(dimethyl siloxane)) as the microfluidic chip material. PDMS is not as transparent as polycarbonate; in order to achieve sufficient optical clarity, it was necessary to use a very thin layer of PDMS. I used an 8:1 ratio of backbone to crosslinker and spun the uncrosslinked mix (after degassing) at low speed (200rpm) onto a vapor-silanized silicon mold fabricated using Bosch RIE. After the polymer cured, I carefully removed it from the wafer and cut to size with a razor blade.

Chip carriers that were compatible with the 2x1cm microfluidic chip were unavailable, so a custom PCB with bondable surface treatment (ENIG) was fabricated and attached directly to the chip with silver epoxy and wire bonds. The PDMS cap was then mated to the surface of the PMN-PT chip. As vacuum-driven flow was to be used for this experiment, no plasma treatment

or other adhesion promotion step was necessary. Fluidic connections were made using unpatterned blocks of thick PDMS as gaskets. See Figure 5-17 for images of the packaged device.

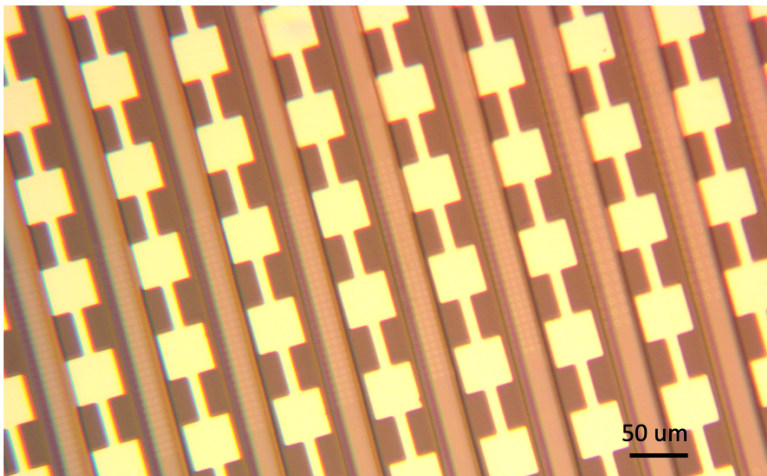
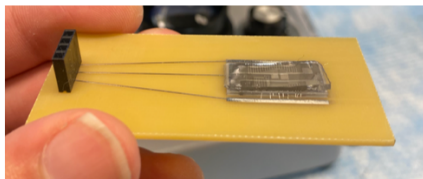


Figure 5-17: Packaged PMN-PT microfluidic chip. Above: PMN-PT substrate with PDMS microfluidic cap, bonded to PCB. Right: Microscope image of 50um electrode region. 4um and 6um nickel micromagnets are visible within channels.

The microfluidic assembly worked as intended and I was able to achieve vacuum-driven flow of particles over the nickel microstructures. Unfortunately, reliable capture, particle motion, or release from these microstructures was not observed, possibly due to some defect during the fabrication process.

Chapter 5h: Discussion

Though still limited by fundamental technical problems with strain control, the potential of multiferroic systems to precisely control magnetic particles in a fluid cannot be overlooked. We have demonstrated programmatic capture and manipulation of a particle in a fluid and described a design for a magnetic valve that could be implemented using this technology. Continued work by others on the fabrication of microstructures using more promising magnetic materials such as Terfenol-D and Ni/CoFeB composites will likely open up new avenues for local strain control and make this design realizable (Xiao *et al.* 2020).

Conclusion

Taken together, the various fabrication methods and devices described here represent a variety of approaches to a common goal: simple and powerful electronic-microfluidic devices using alternative manufacturing technologies. As the commercial sector takes more of an interest in microfluidics for diagnostics, high-throughput screening, biomanufacturing, drug delivery, and many other application areas, novel strategies for low-cost packaging of electronic-microfluidic systems are needed. To this end, I have described a process based on hot embossing and deformation of embedded metal elements that has versatile patterning capability in one or more layers.

I have also described several classes of compact, active flow control elements, including two types of bubble-actuated pumps, one driven by an acid-base reaction and the other by the electrolysis of water. By including the pump on-chip, one obviates the need for an external pneumatic system, which opens up opportunity in drug delivery, handheld diagnostics, autonomous sample collection systems, and other areas.

Finally, I have described considerable progress toward a parallelizable, compact, low-power method of controlling magnetic particle motion using an electric field. The use of multiferroic heterostructures to manipulate biological materials is an emerging field and one that shows promise, though substantial technical challenges remain in realizing this technology.

Each of the devices described above requires considerable optimization, and there is a great deal of room for further work in this space. The manufacturing methods used in this work are simple inexpensive, with few exceptions. It is my hope that these methods are adopted by other researchers working at the interface of microfluidics and microelectronics and that they contribute to the development of inexpensive, portable microfluidic devices with well-developed manufacturing practices.

Works Cited

- Aran, Kiana, Marc Chooljian, Jacobo Paredes, Mohammad Rafi, Kunwoo Lee, Allison Y. Kim, Jeanny An, *et al.* 2017. "An Oral Microjet Vaccination System Elicits Antibody Production in Rabbits." *Science Translational Medicine* 9 (380): eaaf6413. <https://doi.org/10.1126/scitranslmed.aaf6413>.
- Balakrishnan, Karthik R., Jeremy C. Whang, Richard Hwang, James H. Hack, Lucy A. Godley, and Lydia L. Sohn. 2015. "Node-Pore Sensing Enables Label-Free Surface-Marker Profiling of Single Cells." *Analytical Chemistry* 87 (5): 2988–95. <https://doi.org/10.1021/ac504613b>.
- Becker, Holger, and Laurie E. Locascio. 2002. "Polymer Microfluidic Devices." *Talanta* 56 (2): 267–87. [https://doi.org/10.1016/S0039-9140\(01\)00594-X](https://doi.org/10.1016/S0039-9140(01)00594-X).
- Berthier, Erwin, Edmond W.K. Young, and David Beebe. 2012. "Engineers Are from PDMS-Land, Biologists Are from Polystyrenia." *Lab on a Chip* 12 (7): 1224–37. <https://doi.org/10.1039/c2lc20982a>.
- Böhm, S., W. Olthuis, and P. Bergveld. 1999. "An Integrated Micromachined Electrochemical Pump and Dosing System." *Biomedical Microdevices*. Vol. 1. Kluwer Academic Publishers. <https://doi.org/10.1023/A:1009996407848>.
- Chatzimichail, Stelios, Pashiini Supramaniam, Oscar Ces, and Ali Salehi-Reyhani. 2018. "Micropatterning of Planar Metal Electrodes by Vacuum Filling Microfluidic Channel Geometries." *Scientific Reports* 8 (1). <https://doi.org/10.1038/s41598-018-32706-6>.
- Cone, Richard A. 2009. "Barrier Properties of Mucus." *Advanced Drug Delivery Reviews* 61 (2): 75–85. <https://doi.org/10.1016/j.addr.2008.09.008>.
- Conte, Roberto Lo, Zhuyun Xiao, Cai Chen, Camelia V. Stan, Jon Gorchon, Amal El-Ghazaly, Mark E. Nowakowski, *et al.* 2018. "Influence of Nonuniform Micron-Scale Strain Distributions on the Electrical Reorientation of Magnetic Microstructures in a Composite Multiferroic Heterostructure." *Nano Letters* 18 (3): 1952–61. <https://doi.org/10.1021/acs.nanolett.7b05342>.
- Damiri, Hazem Salim, and Hamzeh Khalid Bardaweel. 2015. "Numerical Design and Optimization of Hydraulic Resistance and Wall Shear Stress inside Pressure-Driven Microfluidic Networks." *Lab on a Chip* 15 (21): 4187–96. <https://doi.org/10.1039/c5lc00578g>.
- DiBari, George A. 2008. "Nickel Plating." In *Plating and Surface Finishing*, 95:27–28. <https://doi.org/10.31399/asm.hb.v05.a0001245>.
- Duncombe, Todd A., and Amy E. Herr. 2013. "Photopatterned Free-Standing Polyacrylamide Gels for Microfluidic Protein Electrophoresis." *Lab on a Chip* 13 (11): 2115–23. <https://doi.org/10.1039/c3lc50269d>.
- Fissi, Lamia El, Román Fernández, Pablo García, María Calero, José V. García, Yolanda Jiménez, Antonio Arnau, and Laurent A. Francis. 2019. "OSTEMER Polymer as a Rapid Packaging of Electronics and Microfluidic System on PCB." *Sensors and Actuators, A: Physical* 285: 511–18. <https://doi.org/10.1016/j.sna.2018.11.050>.
- Forrest, Stephen R. 2004. "The Path to Ubiquitous and Low-Cost Organic Electronic Appliances on Plastic." *Nature* 428 (6986): 911–18. <https://doi.org/10.1038/nature02498>.
- Goral, V. N., Y. C. Hsieh, O. N. Petzold, R. A. Faris, and P. K. Yuen. 2010. "Hot Embossing of Plastic Microfluidic Devices Using Poly(Dimethylsiloxane) Molds." *14th International*

- Conference on Miniaturized Systems for Chemistry and Life Sciences 2010, MicroTAS 2010 2* (1): 1214–16.
- Ha, Mingjing, Jung Woo T. Seo, Pradyumna L. Prabhumirashi, Wei Zhang, Michael L. Geier, Michael J. Renn, Chris H. Kim, Mark C. Hersam, and C. Daniel Frisbie. 2013. "Aerosol Jet Printed, Low Voltage, Electrolyte Gated Carbon Nanotube Ring Oscillators with Sub-5 Ms Stage Delays." *Nano Letters* 13 (3): 954–60. <https://doi.org/10.1021/nl3038773>.
- Heuck, F., P. Van Der Ploeg, and U. Staufer. 2011. "Deposition and Structuring of Ag/AgCl Electrodes inside a Closed Polymeric Microfluidic System for Electroosmotic Pumping." In *Microelectronic Engineering*, 88:1887–90. Elsevier. <https://doi.org/10.1016/j.mee.2011.01.058>.
- Heyderman, L. J., H. Schiff, C. David, J. Gobrecht, and T. Schweizer. 2000. "Flow Behaviour of Thin Polymer Films Used for Hot Embossing Lithography." *Microelectronic Engineering* 54 (3–4): 229–45. [https://doi.org/10.1016/S0167-9317\(00\)00414-7](https://doi.org/10.1016/S0167-9317(00)00414-7).
- Jung, Phill Gu, Im Deok Jung, Sang Min Lee, and Jong Soo Ko. 2008. "A Micropatterned Metal Embedding Process for the Formation of Metal Lines in Flexible Electronics." *Journal of Micromechanics and Microengineering* 18 (3): 35017. <https://doi.org/10.1088/0960-1317/18/3/035017>.
- Khan, M. F., N. Miriyala, J. Lee, M. Hassanpourfard, A. Kumar, and T. Thundat. 2016. "Heat Capacity Measurements of Sub-Nanoliter Volumes of Liquids Using Bimaterial Microchannel Cantilevers." *Applied Physics Letters* 108 (21): 211906. <https://doi.org/10.1063/1.4952614>.
- Khanvilkar, Kavita, Maureen D. Donovan, and Douglas R. Flanagan. 2001. "Drug Transfer through Mucus." *Advanced Drug Delivery Reviews* 48 (2–3): 173–93. [https://doi.org/10.1016/S0169-409X\(01\)00115-6](https://doi.org/10.1016/S0169-409X(01)00115-6).
- Khoshmanesh, Khashayar, Shi Yang Tang, Jiu Yang Zhu, Samira Schaefer, Arnan Mitchell, Kouros Kalantar-Zadeh, and Michael D. Dickey. 2017. "Liquid Metal Enabled Microfluidics." *Lab on a Chip* 17 (6): 974–93. <https://doi.org/10.1039/c7lc00046d>.
- Kim, Sang Nyon, James F. Rusling, and Fotios Papadimitrakopoulos. 2007. "Carbon Nanotubes for Electronic and Electrochemical Detection of Biomolecules." *Advanced Materials* 19 (20): 3214–28. <https://doi.org/10.1002/adma.200700665>.
- Kirby, Brian. 2010. *Micro- and Nanoscale Fluid Mechanics. Micro- and Nanoscale Fluid Mechanics*. Cambridge University Press. <https://doi.org/10.1017/cbo9780511760723>.
- Lai, Samuel K., Ying Ying Wang, Denis Wirtz, and Justin Hanes. 2009. "Micro- and Macrorheology of Mucus." *Advanced Drug Delivery Reviews* 61 (2): 86–100. <https://doi.org/10.1016/j.addr.2008.09.012>.
- Lau, Pak Heng, Kuniharu Takei, Chuan Wang, Yeonkyeong Ju, Junseok Kim, Zhibin Yu, Toshitake Takahashi, Gyoujin Cho, and Ali Javey. 2013. "Fully Printed, High Performance Carbon Nanotube Thin-Film Transistors on Flexible Substrates." *Nano Letters* 13 (8): 3864–69. <https://doi.org/10.1021/nl401934a>.
- Levie, R. De. 1999. "The Electrolysis of Water." *Journal of Electroanalytical Chemistry* 476 (1): 92–93. [https://doi.org/10.1016/S0022-0728\(99\)00365-4](https://doi.org/10.1016/S0022-0728(99)00365-4).
- Li, Ping, Hanne Morck Nielsen, and Anette Müllertz. 2012. "Oral Delivery of Peptides and Proteins Using Lipid-Based Drug Delivery Systems." *Expert Opinion on Drug Delivery* 9 (10): 1289–1304. <https://doi.org/10.1517/17425247.2012.717068>.

- Lin, Che Hsin, Chien Hsiang Chao, and Che Wei Lan. 2007. "Low Azeotropic Solvent for Bonding of PMMA Microfluidic Devices." *Sensors and Actuators, B: Chemical* 121 (2): 698–705. <https://doi.org/10.1016/j.snb.2006.04.086>.
- Liu, C., J. M. Li, J. S. Liu, and L. D. Wang. 2010. "Deformation Behavior of Solid Polymer during Hot Embossing Process." *Microelectronic Engineering* 87 (2): 200–207. <https://doi.org/10.1016/j.mee.2009.07.014>.
- Liu, Ming, Shandong Li, Ziyao Zhou, Shawn Beguhn, Jing Lou, Feng Xu, Tian Jian Lu, and Nian X. Sun. 2012. "Electrically Induced Enormous Magnetic Anisotropy in Terfenol-D/Lead Zinc Niobate-Lead Titanate Multiferroic Heterostructures." *Journal of Applied Physics* 112 (6): 063917. <https://doi.org/10.1063/1.4754424>.
- Ma, Yunzhe, Wenqian Tao, Shelly J. Krebs, William F. Sutton, Nancy L. Haigwood, and Harvinder S. Gill. 2014. "Vaccine Delivery to the Oral Cavity Using Coated Microneedles Induces Systemic and Mucosal Immunity." *Pharmaceutical Research* 31 (9): 2393–2403. <https://doi.org/10.1007/s11095-014-1335-1>.
- Messner, Stephan, Jochen Schaible, Peter Nommensen, and Roland Zengerle. 2007. "Electrostatically Driven 3-Way Silicon Microvalve for Pneumatic Applications." *Sensors and Materials* 19 (1): 57–78.
- Mohammadzadeh, Aliakbar, Alison E. Fox Robichaud, and Ponnambalam Ravi Selvaganapathy. 2019. "Rapid and Inexpensive Method for Fabrication and Integration of Electrodes in Microfluidic Devices." *Journal of Microelectromechanical Systems* 28 (4): 597–605. <https://doi.org/10.1109/JMEMS.2019.2914110>.
- Molina, Daniel E., Adan Schafer Medina, Haluk Beyenal, and Cornelius F. Ivory. 2019. "Design and Finite Element Model of a Microfluidic Platform with Removable Electrodes for Electrochemical Analysis." *Journal of The Electrochemical Society* 166 (2): B125–32. <https://doi.org/10.1149/2.0891902jes>.
- Munief, Walid Madhat, Ruben Lanche, Xiaoling Lu, Sven Ingebrandt, and Vivek Pachauri. 2018. "Wafer-Scale Fabrication of Microelectrode Arrays on Optically Transparent Polymer Foils for the Integration of Flexible Nanoscale Devices." *Flexible and Printed Electronics* 3 (4). <https://doi.org/10.1088/2058-8585/aae3b6>.
- Murali, Pramod, Ali M. Niknejad, and Bernhard E. Boser. 2017. "CMOS Microflow Cytometer for Magnetic Label Detection and Classification." *IEEE Journal of Solid-State Circuits* 52 (2): 543–55. <https://doi.org/10.1109/JSSC.2016.2621036>.
- Murray, Coleman, Edward Pao, Peter Tseng, Shayan Aftab, Rajan Kulkarni, Matthew Rettig, and Dino Di Carlo. 2016. "Quantitative Magnetic Separation of Particles and Cells Using Gradient Magnetic Ratcheting." *Small* 12 (14): 1891–99. <https://doi.org/10.1002/smll.201502120>.
- Ng, Jessamine M.K., Irina Gitlin, Abraham D. Stroock, and George M. Whitesides. 2002. "Components for Integrated Poly(Dimethylsiloxane) Microfluidic Systems." *Electrophoresis* 23 (20): 3461–73. [https://doi.org/10.1002/1522-2683\(200210\)23:20<3461::AID-ELPS3461>3.0.CO;2-8](https://doi.org/10.1002/1522-2683(200210)23:20<3461::AID-ELPS3461>3.0.CO;2-8).
- Novak, Richard, Navpreet Ranu, and Richard A. Mathies. 2013. "Rapid Fabrication of Nickel Molds for Prototyping Embossed Plastic Microfluidic Devices." *Lab on a Chip* 13 (8): 1468–71. <https://doi.org/10.1039/c3lc41362d>.
- Paredes, Jacobo, Kathryn D. Fink, Richard Novak, and Dorian Liepmann. 2015. "Self-Anchoring

- Nickel Microelectrodes for Rapid Fabrication of Functional Thermoplastic Microfluidic Prototypes." *Sensors and Actuators, B: Chemical* 216 (September): 263–70. <https://doi.org/10.1016/j.snb.2015.04.041>.
- Park, Bong Kyun, Dongjo Kim, Sunho Jeong, Jooho Moon, and Jang Sub Kim. 2007. "Direct Writing of Copper Conductive Patterns by Ink-Jet Printing." *Thin Solid Films* 515 (19 SPEC. ISS.): 7706–11. <https://doi.org/10.1016/j.tsf.2006.11.142>.
- Peng, Linfa, Yujun Deng, Peiyun Yi, and Xinmin Lai. 2014. "Micro Hot Embossing of Thermoplastic Polymers: A Review." *Journal of Micromechanics and Microengineering* 24 (1). <https://doi.org/10.1088/0960-1317/24/1/013001>.
- Prausnitz, Mark R., Yasmine Gomaa, and Wei Li. 2019. "Microneedle Patch Drug Delivery in the Gut." *Nature Medicine*. Nature Publishing Group. <https://doi.org/10.1038/s41591-019-0606-0>.
- Rodriguez-Trujillo, Romen, Oscar Castillo-Fernandez, Miquel Garrido, Martin Arundell, Antoni Valencia, and Gabriel Gomila. 2008. "High-Speed Particle Detection in a Micro-Coulter Counter with Two-Dimensional Adjustable Aperture." *Biosensors and Bioelectronics* 24 (2): 290–96. <https://doi.org/10.1016/j.bios.2008.04.005>.
- Saha, Biswajit, Shu B. Tor, Erjia Liu, David E. Hardt, and Jung H. Chun. 2011. "Hot-Embossing Performance of Silicon Micromold Coated with Self-Assembled n-Octadecyltrichlorosilane." *Sensors and Actuators, B: Chemical* 160 (1): 207–14. <https://doi.org/10.1016/j.snb.2011.07.036>.
- Schrott, Walter, Miloš Svoboda, Zdeněk Slouka, and Dalimil Šnita. 2009. "Metal Electrodes in Plastic Microfluidic Systems." *Microelectronic Engineering* 86 (4–6): 1340–42. <https://doi.org/10.1016/j.mee.2009.01.001>.
- Shen, Meng, Christophe Yamahata, and Martin A.M. Gijs. 2008. "Miniaturized PMMA Ball-Valve Micropump with Cylindrical Electromagnetic Actuator." *Microelectronic Engineering* 85 (5–6): 1104–7. <https://doi.org/10.1016/j.mee.2007.12.013>.
- Sinha, Ashok, Ranjan Ganguly, K. Anindya De, and K. Ishwar Puri. 2007. "Single Magnetic Particle Dynamics in a Microchannel." *Physics of Fluids* 19 (11): 117102. <https://doi.org/10.1063/1.2780191>.
- So, Ju Hee, and Michael D. Dickey. 2011. "Inherently Aligned Microfluidic Electrodes Composed of Liquid Metal." *Lab on a Chip* 11 (5): 905–11. <https://doi.org/10.1039/c0lc00501k>.
- Sohn, Hyunmin, Cheng yen Liang, Mark E. Nowakowski, Yongha Hwang, Seungoh Han, Jeffrey Bokor, Gregory P. Carman, and Robert N. Candler. 2017. "Deterministic Multi-Step Rotation of Magnetic Single-Domain State in Nickel Nanodisks Using Multiferroic Magnetoelastic Coupling." *Journal of Magnetism and Magnetic Materials* 439 (October): 196–202. <https://doi.org/10.1016/j.jmmm.2017.04.077>.
- Sohn, Hyunmin, Mark E. Nowakowski, Cheng Yen Liang, Joshua L. Hockel, Kyle Wetzlar, Scott Keller, Brenda M. McLellan, *et al.* 2015. "Electrically Driven Magnetic Domain Wall Rotation in Multiferroic Heterostructures to Manipulate Suspended On-Chip Magnetic Particles." *ACS Nano* 9 (5): 4814–26. <https://doi.org/10.1021/nn5056332>.
- Sun, Tao, Catia Bernabini, and Hywel Morgan. 2010. "Single-Colloidal Particle Impedance Spectroscopy: Complete Equivalent Circuit Analysis of Polyelectrolyte Microcapsules." *Langmuir* 26 (6): 3821–28. <https://doi.org/10.1021/la903609u>.
- Tamura, N., M. Kunz, K. Chen, R. S. Celestre, A. A. MacDowell, and T. Warwick. 2009. "A

- Superbend X-Ray Microdiffraction Beamline at the Advanced Light Source." *Materials Science and Engineering A* 524 (1–2): 28–32. <https://doi.org/10.1016/j.msea.2009.03.062>.
- Tamura, Nobumichi. 2014. "XMAS: A Versatile Tool for Analyzing Synchrotron X-Ray Microdiffraction Data." In *Strain and Dislocation Gradients from Diffraction: Spatially-Resolved Local Structure and Defects*, 125–55. Imperial College Press. https://doi.org/10.1142/9781908979636_0004.
- Tang, Wenlai, Dezhi Tang, Zhonghua Ni, Nan Xiang, and Hong Yi. 2017. "Microfluidic Impedance Cytometer with Inertial Focusing and Liquid Electrodes for High-Throughput Cell Counting and Discrimination." *Analytical Chemistry* 89 (5): 3154–61. <https://doi.org/10.1021/acs.analchem.6b04959>.
- Tang, Xuejiao, Chengliang Bi, Changxiu Han, and Baogui Zhang. 2009. "A New Palladium-Free Surface Activation Process for Ni Electroless Plating on ABS Plastic." *Materials Letters* 63 (11): 840–42. <https://doi.org/10.1016/j.matlet.2009.01.006>.
- Taylor, Hayden, Yee Cheong Lam, and Duane Boning. 2009. "A Computationally Simple Method for Simulating the Micro-Embossing of Thermoplastic Layers." *Journal of Micromechanics and Microengineering* 19 (7): 75007. <https://doi.org/10.1088/0960-1317/19/7/075007>.
- Toepke, Michael W., and David J. Beebe. 2006. "PDMS Absorption of Small Molecules and Consequences in Microfluidic Applications." *Lab on a Chip* 6 (12): 1484–86. <https://doi.org/10.1039/b612140c>.
- Tokuda, Shinsaku, Hiroaki Miyazaki, Ken ichi Nakajima, Toshiki Yamada, and Yoshinori Marunaka. 2009. "Hydrostatic Pressure Regulates Tight Junctions, Actin Cytoskeleton and Transcellular Ion Transport." *Biochemical and Biophysical Research Communications* 390 (4): 1315–21. <https://doi.org/10.1016/j.bbrc.2009.10.144>.
- Unger, Marc A., Hou Pu Chou, Todd Thorsen, Axel Scherer, and Stephen R. Quake. 2000. "Monolithic Microfabricated Valves and Pumps by Multilayer Soft Lithography." *Science* 288 (5463): 113–16. <https://doi.org/10.1126/science.288.5463.113>.
- Wang, Hsiang Yu, and Chang Lu. 2006. "Microfluidic Chemical Cytometry Based on Modulation of Local Field Strength." *Chemical Communications*, no. 33: 3528–30. <https://doi.org/10.1039/b605722e>.
- Wei, Yi Chi, Shin Yu Su, Lung Min Fu, and Che Hsin Lin. 2012. "Electrophoresis Separation and Electrochemical Detection on a Novel Line-Based Microfluidic Device." In *Proceedings of the IEEE International Conference on Micro Electro Mechanical Systems (MEMS)*, 104–7. <https://doi.org/10.1109/MEMSYS.2012.6170104>.
- Welch, David, and Jennifer Blain Christen. 2013. "Seamless Integration of CMOS and Microfluidics Using Flip Chip Bonding." *Journal of Micromechanics and Microengineering* 23 (3): 35009–16. <https://doi.org/10.1088/0960-1317/23/3/035009>.
- Wu, Yifan, James D. Benson, and Mahmoud Almasri. 2012. "Micromachined Coulter Counter for Dynamic Impedance Study of Time Sensitive Cells." *Biomedical Microdevices* 14 (4): 739–50. <https://doi.org/10.1007/s10544-012-9655-6>.
- Xiao, Z., R. Lo Conte, M. Goiriena-Goikoetxea, R. V. Chopdekar, C. H.A. Lambert, X. Li, A. T. N'Diaye, et al. 2020. "Tunable Magnetoelastic Effects in Voltage-Controlled Exchange-Coupled Composite Multiferroic Microstructures." *ACS Applied Materials and Interfaces* 12 (5): 6752–60. <https://doi.org/10.1021/acsami.9b20876>.
- Zhang, Lian, Xiongying Ye, Zhaoying Zhou, and Jian Yao. 1997. "A Micromachined Single-Crystal

Silicon Flow Sensor with a Cantilever Paddle.” In *MHS 1997 - Proceedings of 1997 International Symposium on Micromechatronics and Human Science*, 225–29. Institute of Electrical and Electronics Engineers Inc. <https://doi.org/10.1109/MHS.1997.768884>.

Appendix A: MATLAB script for strain image generation

```
% A is the array containing the x, y and z (dev_z) data
% A=xlsread('Area_Voltage.xlsx');
% Input data format:
% col. 1&2 are x,y coordinates, col 3-5 are xx,yy,zz strains
% sorted by increasing y, then increasing x

A=table2array(A10V);
B=table2array(A1400V);
stepsize = 10; %size of each pixel in microns
squaresize = 40; %size of measured area in pixels

%Remove duplicate measurements from array (caused when beam
power falls
%out of tolerance
[~,indA]=unique(A(:,1:2), 'rows','stable');
[~,indB]=unique(B(:,1:2), 'rows','stable');
%indA/B is the list of rows containing unique x,y values
A = A(indA,:);
B = B(indB,:);

% Extract the columns x,y and dev_z
X=A(:,1);
Y=A(:,2);

%Pad missing pixels
%Using mean value of each column to avoid scaling issues

X_full=min(X):stepsize:max(X);
Y_full=min(Y):stepsize:max(Y);
[a,b]=meshgrid(X_full, Y_full); %generate coordinate grid
fullcoords=sortrows([a(:) b(:)],2); %sort by Y to put in correct
order
[~,missingindA]=setdiff(fullcoords,A(:,1:2),'rows');
[~,missingindB]=setdiff(fullcoords,B(:,1:2),'rows');
for n=1:size(missingindA,1)
    ind=missingindA(n);
    insrow= [fullcoords(ind,:) mean(A(:,3:5))];
    A=[A(1:ind,:); insrow; A(ind+1:end,:)];
end

for n=1:size(missingindB,1)
    ind=missingindB(n);
    insrow= [fullcoords(ind,:) mean(B(:,3:5))];
    B=[B(1:ind,:); insrow; B(ind+1:end,:)];
end
```

```

% Extract the columns x,y and dev_z
X=A(:,1);
Y=A(:,2);
angle=B(:,3)-A(:,3); %column 3 = xx, 4 = yy, 5 = zz
%angle=A(:,3); %for absolute strain of 0V image

%reshape squaresize^2 x 3 array of values into square array
angle=reshape(angle,[squaresize,squaresize]);

%Remove outliers (generally dead pixels)
stdev=std(angle, 0, 'all');
avg=mean(angle, 'all');
angleold=angle;
angle(angle>avg+6*stdev)=avg;
angle(angle<avg-6*stdev)=avg;

%Relative coordinates for X and Y
X=X-min(X);
Y=Y-min(Y);

% Assign the corresponding coordinates "x" and "y"
x=[min(X),max(X)];
y=[min(Y),max(Y)];

%Plot:
image(x,y,angle, 'CDataMapping', 'scaled');
colormap;
colorbar;

% Y-axis increases from bottom to top
ax=gca;
ax.YDir='normal';

% formatting axis numbers
set(gca, 'FontSize', 26);

% labels
xlabel('\fontname{helvetica} \fontsize{28} x (\mum)');
ylabel('\fontname{helvetica} \fontsize{28} y (\mum)');
c = colorbar;
%ylabel(c, '\fontname{helvetica} \fontsize{24} \theta (\circ)');
ylabel(c, '\fontname{helvetica} \fontsize{28} Strain Sxx
(ppt)');

```


Appendix B: Nickel Embossing Mold SOP

Protocol: Hot Embossing and Electrode Pattern Transfer using Electroplated Molds

Process developed by Marc Chooljian and Jacobo Paredes

Table of contents:

1. Necessary reagents and equipment
2. Process flow
 - a. Microchannel embossing
 - b. Single-layer electrode transfer
 - c. Electrode deformation
3. Module specifications
 - a. Lithography (Riston)
 - b. Lithography (S1818)
 - c. Electroplating
 - d. Embossing
 - e. Bonding
4. Safety considerations

Necessary reagents and equipment:

Nickel Electroplating:

- Ventilated electroplating beakers with plate holders
- 2x standard DC power supply
- Nickel plates, cut to 4"x4"
- Caswell nickel electroplating solution, 1400 mL
- Wood's Nickel strike solution (Nickel chloride and 20% HCl in water)
- Hotplates (3)

Lithography (Shared):

- Mask aligner
- Glassware and shaker or rocker for development
- Stainless steel polished wafers, 4"
- Acetone, Isopropanol in spray bottles

Lithography (Channels):

- Roll-to-roll laminator
- Riston GM130 dry-film photoresist
- Developer: Potassium carbonate 1% w/v in water
- Stripper: Potassium or sodium hydroxide 3% w/v in water

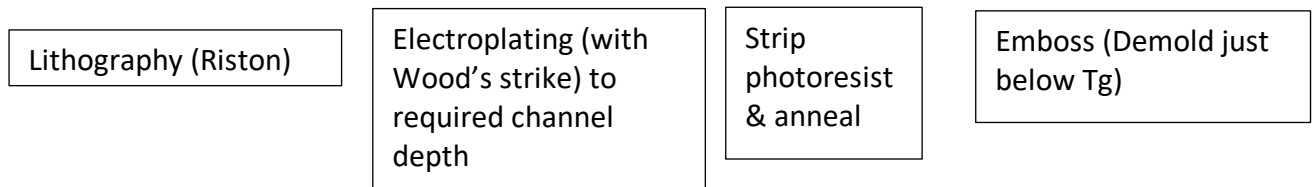
Lithography (Electrode templates):

- Spin coater
- Hot plate
- Microposit S-1818 photoresist
- Developer: MF-321
- Stripper: Acetone

Process flow:

Please refer to next section for process module details

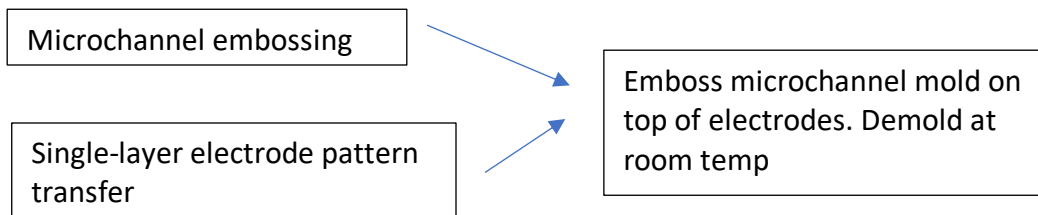
Microchannel embossing:



Single-layer electrode pattern transfer:



Electrode deformation:



After processing each layer, drill inlets (#70 drill bit) and contact pads and bond (see bonding section for details)

Module specifications

Lithography

Background:

Photolithography is a technique involving the transfer of a pattern from a photomask (a chrome-coated glass plate or printed mylar sheet) into a substrate wafer coated with a photosensitive polymer called a photoresist. This is the method used to pattern the features for each step in a microfabrication process. There are two broad categories of photoresist:

positive-tone and negative-tone. This distinction refers to the change in solubility of the photoresist when exposed to light: in a positive-tone photoresist, the areas exposed to UV light become soluble in the developer, while in a negative-tone photoresist they become insoluble. The photomasks used in this process must be designed with this in mind; a positive-tone photoresist mask must be the inverse of a negative-tone photoresist mask to achieve the same pattern.

This process uses two different photoresists. For the mold fabrication step, the photoresist used is **Riston GM-130**, a negative-tone dry film photoresist. For the electrode patterning step, the photoresist is **Microposit S-1818**, a positive-tone liquid photoresist. The substrate used for both processes is a **4" stainless steel single-side polished wafer**.

This entire process is carried out in a cleanroom environment in order to minimize the exposure of the wafer to 1. dust, and 2. violet or UV light. Cleanrooms are HEPA-filtered and lit by low-frequency yellow-orange lights.

Additional details for the processing of both photoresists can be found in their datasheets.

Riston process:

At the start of the process, turn on the mercury UV lamp (allow to warm up for ~20 minutes if off, and do not turn on if it has been turned off in the last 30 minutes) and the laminator. Allow the laminator to heat to 115 degrees C.

1. Prepare the wafer for patterning by cleaning it. Rinse the stainless steel wafer with acetone for 45 seconds to 1 minute and soak in isopropyl alcohol dish with light agitation, then air dry with a nitrogen gun.
2. Coating:
 - a. Ensure the roller is turned on and is running at 115 degrees C, speed 5.
 - b. Cut a square of Riston GM-130 from the roll. Carefully remove the plastic coating from the matte side. Place the wafer on top of a sheet of Tekwipe at least as large as the square of Riston, and place the photoresist sheet exposed side (the side you just removed the plastic from) down on top of the wafer. Finally, place the wafer between two sheets of Kapton to protect the rollers and prevent wrinkling of the film (the sheets of Kapton should be precut and placed near the laminator). The result should be a stack of (from bottom to top) Kapton, Tekwipe, wafer, Riston, Kapton.
 - c. Carefully feed the stack between the rollers, keeping your fingers well clear. If anything gets unintentionally stuck between the rollers, press the "reverse" button on the laminator. Wait for it to fully emerge on the other side before retrieving.
 - d. Remove the Kapton layers and place the (now laminated) wafer on a cooling rack to cool down to room temperature.
3. Exposure
 - a. Ensure the mask aligner has finished warming up and the voltage is stable.
 - b. Measure the UV intensity in mW/cm^2 using the UV meter and record it.

- c. I have gotten the best results with Riston GM130 with an exposure energy of approximately 70 mJ/cm^2 , though you may wish to vary the exposure if your process results vary. Calculate the desired exposure time using this target energy and the measured UV intensity.
 - d. Load wafer and mask, align, and expose
 - e. Remove the wafer and develop immediately (the datasheet does not suggest a PEB, nor have I found one necessary)
4. Development
- a. Develop in 1% w/v potassium carbonate solution, under vigorous agitation, for ~5 minutes. If the area of dissolved features on the surface is large, photoresist loading of the solution may occur. If this is the case, move the wafer to a fresh dish of developer half-way through the development process.
 - b. Rinse for 10 seconds with a spray of developer, then rinse in deionized water for 30 seconds.
 - c. Air dry and inspect features. Slanted sidewalls suggest overexposure or underdevelopment. Cavities in the sidewalls or cracking suggest overdevelopment.

S-1818 process:

As with the Riston process, turn on the UV lamp early to ensure that it is warmed up by the photoresist step. Also turn a hotplate and allow it to heat to 115 degrees C

1. Clean the stainless steel wafer as done in the Riston process. Then dry the wafer on a hotplate at 115 degrees C for 1 minute.
2. Coating:
 - a. Place the wafer on the spin-coater and test for centering using the attached centering arm.
 - b. Program in your desired spin speed: for this process, I use an initial spin speed of 500rpm for 5 seconds, followed by a 45 second spin at 1000 rpm. This should achieve a layer thickness of roughly $4 \mu\text{m}$. Adjust the spin speed if this is not achieved – photoresists can noticeably thicken as they age and their solvent evaporates. Run the program and test for centering and vacuum seal.
 - c. Place an approximately quarter-sized drop of S1818 in the center of the wafer using a dropper. Close the lid of the spinner and start the spin.
 - d. If edge-bead removal is desired (i.e. if trying to resolve small features), carefully use an acetone-soaked Tekwipe to remove a small ring of photoresist around the edge of the wafer before detaching from the vacuum chuck.
 - e. Soft bake: The purpose of this step is to evaporate the solvent in the photoresist and prepare it for exposure. Bake on a hotplate at 115C for 60 seconds. Cool to room temperature on a cooling rack.
3. Expose
 - a. Ensure the mask aligner has finished warming up and the voltage is stable.
 - b. Measure the UV intensity in mW/cm^2 using the UV meter and record it.

- c. Calculate an exposure time for a dose of approximately 150 mJ/cm² (may vary according to process results)
 - d. Load wafer and mask, align, and expose
 - e. No post-exposure bake is necessary. Remove wafer and immediately develop
4. Development
- a. Develop in MF-319 or MF-321 under gentle agitation for approximately 45 seconds (until clear)
 - b. Rinse in DI water for 30 seconds
 - c. Air dry using nitrogen gun and inspect features.

Electroplating

Background:

Electroplating (also known as electrodeposition or anodization) is the process of using an electric current to deposit dissolved metal cations on a conductive surface. An electric potential applied between a “donor” ion source (the anode) and the surface to be coated (the cathode) causes oxidation of the anode metal and reduction of the resulting dissolved metal ions at the cathode, forming a layer of the anodic metal on the cathode. In this case, the anode is nickel and the cathode is the stainless steel wafer. The exposed areas of the wafer are coated in nickel deposits, forming the mold or the electrode templates. The reaction is carried out in a conductive solution of nickel chloride and nickel sulfate and the electric potential and current are supplied by a DC power source under constant current conditions.

In order to promote adhesion of the nickel deposits to the stainless steel, a pretreatment process called a Wood’s strike can be performed. This involves a high-current (1A) short (~1 minute) plating process in a concentrated nickel chloride/HCl solution. This removes the oxide layer on the surface of the stainless steel and drives in a thin layer of nickel, creating a surface layer that has stronger adhesion to the nickel deposits. This step is carried out immediately prior to the plating in the mold process, but not in the electrode process.

Plating process (mold):

1. Turn on the nickel strike and plating solution hot plates and stirrers and allow them to heat to 50 degrees C. If the level of either solution is less than 1400 mL, it is because water has evaporated from the solution. Fill it to 1400 mL with DI water (inside a fume hood).
2. If significant time has passed since the photolithography process, clean the wafer with DI water thoroughly and air-dry with N₂.
3. Using vinyl adhesive, mask off the backside of the wafer to prevent backside plating. This is important because the plating time is proportional to the exposed surface area – leaving the backside of the wafer exposed will increase the plating time and throw off your thickness calculations. Remember to leave a side of the wafer uncovered by the adhesive so that you can clamp the steel with more ease. Ensure to fold the adhesive to cover the parts of the front of the wafer that you do not wish to electroplate if not covered with photoresist.
4. Wood’s Nickel Strike (adhesion treatment):

NOTE: Always remember to abide to safety regulations: wear appropriate chemical gloves and do not remove the Wood's Nickel Strike solution from the fume hood.

- a. Rinse the wafer holder and nickel plate with DI water
 - b. Place the wafer in a wafer holder (diagram WIP) across from a nickel plate. Attach alligator clips to wafer and plate – connect the positive lead to the nickel and the negative lead to the wafer. Within a fume hood, carefully lower the holder into the nickel strike bath and affix it to the lid. This step is hazardous – wear chemical gloves, as the strike solution is corrosive due to its high acid content. Ensure that the stirring bar is still mixing the solution before proceeding to the next step.
 - c. Set the current to 1A and strike for 1 minute. The cathode should bubble during this process.
 - d. Reduce the current to zero, turn off the power supply, and carefully remove the holder from the solution. Ensuring the power supply is off, remove the leads. Briefly rinse the holder, wafer, and nickel plate with DI water over a glass dish. The goal is to minimize the time between the Wood Strike and the Nickel Plating.
5. Nickel Plating:
- a. Maintain the Nickel Plating solution at an average temperature of 55 degrees C. Attach the nickel plating leads and place the holder in the nickel plating solution. Set the current to 65 mA and plate for the desired time to reach your desired thickness (will be anywhere from 1-5 hours). Do not plate thicker than 60 μm .
 - b. Reduce the current to zero, turn off the power supply, and carefully remove the holder from the solution. Ensuring the power supply is off, remove the leads. Rinse well the holder, wafer, and nickel plate with DI water over a glass dish. Remove the wafer from the holder, rinse again with DI water, making sure to remove all remaining plating solution. Dry using N₂.
6. Photoresist Strip and Anneal:
- a. Remove the vinyl from the backside of the wafer.
 - b. Place the wafer in a bath of sodium or potassium hydroxide, 3% w/v (this should be done in a fume hood as both compounds are strong bases, though the concentrations used in this case are very low). Agitate gently. Let sit until the photoresist layer flakes off (usually around 10-20 minutes).
 - c. Turn on a hot plate and allow it to heat up to 150 degrees C/
 - d. Remove the wafer from the bath and rinse in deionized water. Filter the photoresist flakes from the solution using a Tekwipe and funnel and dispose of the solution appropriately. Dry the wafer well using N₂.
 - e. Anneal the wafer on a hot plate. Place the wafer on the hot plate at 150 degrees C, and allow the hot plate to heat gradually to 400 degrees C, then anneal for 10 minutes at this final temperature. This step reduces residual stress in the nickel and increases the mechanical strength of the mold. After the anneal, cool gradually by turning off the hot plate and waiting ~20 minutes. The gradual cool is necessary to avoid thermal mismatch stress. **Remain near the hot plate throughout this entire process, and ensure that all flammables (i.e. acetone, IPA) are far from the hot plate and that there are no traces of them on the**

wafer. Ensure the hot plate has had sufficient time to cool before removing the wafer. 400 degrees C is VERY HOT.

Plating process (electrodes):

1. Turn on the nickel plating solution hot plate and stirrer and allow it to heat to 55 degrees C. If the level of either solution is less than 1400 mL, it is because water has evaporated from the solution. Fill it to 1400 mL with DI water (inside a fume hood).
2. If significant time has passed since the photolithography process, clean the wafer with DI water thoroughly and air-dry with N₂.
3. Using vinyl adhesive, mask off the backside of the wafer to prevent backside plating. This is important because the plating time is proportional to the exposed surface area – leaving the backside of the wafer exposed will increase the plating time and throw off your thickness calculations.
4. For the electrode process, there is no Wood's nickel strike step. It is desired for the electrodes to separate from the wafer after embossing so no adhesion treatment is necessary. If the electrodes separate prematurely (i.e. during the photoresist strip step) you may try a short nickel strike here.
5. Nickel Plating:
 - a. Attach the nickel plating leads and place the holder in the nickel plating solution. Set the current to 65 mA and plate for the desired time to reach your desired thickness. For features smaller than 50 μm , plate around 3 μm (assuming a photoresist thickness of $\sim 4\mu\text{m}$ – the goal is to keep the electrodes thinner than the photoresist). For larger features, plate around 4 μm which should take about 10 minutes. For the larger features, overplating the photoresist forms an anchor-like structure that assists in the transfer process.
 - b. Reduce the current to zero, turn off the power supply, and carefully remove the holder from the solution. Ensuring the power supply is off, remove the leads. Rinse the holder, wafer, and nickel plate with DI water over a glass dish. Remove the wafer from the holder, rinse again with DI water, making sure to remove all remaining plating solution. Dry using N₂ and remove the adhesive tape trying to avoid contact with the features.
 - c. Strip the photoresist by immersing the wafer in acetone without agitation. Rinse it in IPA and then dry gently in N₂. At this point, it is sometimes necessary to use care to prevent the electrodes from lifting off prematurely, especially with smaller features.
 - d. Lastly, utilize microscopy to check the thickness of the features and determine if they are adequate for testing.

Embossing and Bonding

1. Create two PDMS cushions to ensure even pressure distribution on the sample.
2. Place the following items in the hot embossing machine in order from top to bottom
 - a. PDMS cushion
 - b. Empty backing steel wafer for alignment

- c. Plastic cut in a square
- d. Steel wafer, polycarbonate, or plastic mold
- e. PDMS cushion

Polycarbonate embossing: this material has a glass transition temperature of 145 degrees C, therefore use a temperature between 155- and 160-degrees C and a pressure of 500 Psi. Embossing time depends on feature size – typically 10 – 20 minutes.

For channel molds, release pressure and demold as soon as possible after platens cool below 130C in order to avoid thermal clamping. For electrode transfer, allow to cool to room temperature under pressure.

Thermal bonding of polycarbonate: 130 degrees C, 900 PSI, 30 minutes. Allow to cool to room temperature under pressure.

Safety Considerations

Nickel plating solutions: Nickel and its salts are toxic if ingested or inhaled in large amounts, but are relatively safe at the concentrations we are working with (nickel toxicity is typically seen in people working at nickel smelting plants or machining nickel, who encounter large amounts of nickel dust). Nevertheless, it is good practice to limit exposure to the nickel plating solution. Ensure the wafer is clean of nickel solution before touching it with your hands, and do not move the nickel plating solution outside of the ventilated areas without a lid, especially if it is hot. Contact dermatitis is a very common response to nickel exposure, and is not life-threatening, but it is annoying – avoid getting nickel solution on your skin.

Nickel strike solution: The nickel strike solution is 20% hydrochloric acid, and is thus strongly corrosive. All work with the nickel strike solution should be done in a fume hood wearing proper chemical PPE, in particular chemically resistant gloves. This includes making the solution, transferring wafers into and out of the solution, and the strike process itself. Under no circumstances should the nickel strike solution be moved out of its designated area in the fume hood. Mixing the nickel strike solution involves highly concentrated HCl and is thus likely the most dangerous part of this process. Use appropriate chemical PPE and safety practice and, as always, pour acid into water, not the other way around. Any accidental exposure to nickel strike solution, like a spill, should be treated as a hazardous chemical exposure.

Electricity: High currents, in particular the 1A current used during the nickel strike process, are dangerous. Ensure that the power supply is off whenever the leads are not firmly secure to the wafer and plate in the plating bath (i.e. when plating). Do not under any circumstances touch the leads, wafer, or nickel plate when the power supply is on.

Heat: Several steps in this process, including but not limited to the S-1818 post exposure bake, the embossing step, and in particular the nickel anneal involve hot plates in excess of 100 degrees C. Take care to keep the areas around these hot plates clear of debris and ensure that

any flammables such as acetone or isopropanol are far away. During the exceptionally high temperatures of the nickel anneal, monitor the process directly for the entire duration. The electroplating baths themselves are heated to temperatures of 50 degrees C, which is hot enough to burn you if handled carelessly. In particular, if handling the plating solution beaker (to move it to the fume hood for transfer, for instance), wear heat-resistant gloves.

Disposal: Nickel and nickel strike solutions must be disposed of in appropriately labeled chemical waste containers. In particular, the nickel strike solution is a strong acid and must be disposed of as such – make sure it is not in the same container as any bases or organic solvents. It is appropriate to dispose of nickel strike and nickel plating solution in the same container, **SO LONG AS THAT CONTAINER IS FREE OF BASES OR SOLVENTS.**